UNIVERSITY OF CALIFORNIA, SAN DIEGO

Near-field Characterization of Photonic Nanodevices

A dissertation submitted in partial satisfaction of the requirements for the degree Doctor of Philosophy

in

Electrical Engineering (Photonics)

by

Maxim Abashin

Committee in charge:

Professor Yeshaiahu Fainman, Chair

Professor Prabhakar Bandaru

Professor Joseph Ford

Professor Sungho Jin

Professor Edward Yu

2009

The Dissertation of Maxim Abashin is approved, and it is acceptable in quality and form for publication on microfilm and electronically:

Chair

University of California, San Diego

2009

Table of Contents

List of Figures

Abbreviations and Symbols

Abbreviations

AFM	atomic force microscope/microscopy
AOM	acousto-optic modulator
FDTD	finite-difference time-domain
FEM	finite element method
GRIN	graded index
GVD	group velocity dispersion
HNSOM	heterodyne near-field scanning optical microscope
NSOM	near-field scanning optical microscope/microscopy
PBG	photonic band gap
PBS	polarization beam splitting
PhC	photonic crystal
PSD	position sensitive detector
SEM	scanning electron microscopy
SLD	superluminescent diode
SNR	signal-to-noise ratio
SOI	silicon-on-insulator
STM	scanning tunneling microscope
TIR	total internal reflection
WDM	wavelength division multiplexing

Acknowledgements

I would like to express my gratitude to my advisor, Prof. Shaya Fainman for his mentorship. My appreciation extends to all members of Ultrafast and Nanoscale Optics group at UCSD, especially to Kevin and Slava for teaching me analytical troubleshooting approach; to Uriel and Maziar for giving some initial vector to my research; to Rob for bringing very positive attitude to the graduate student life; to Chiaho, Kaz, Liang and Dawn for fabricating samples; to Antonello for building the initial experimental setup; to visiting scholars for new interesting research opportunities, and to all other students.

I am very thankful to my family, who were always encouraging me and supporting all my endeavors. I would also like to mention all my friends: Jenya, Andrey, Alexander, Ivan, Mikhail, Evgeniy, Dmitry, and many others – thank you so much for being around.

Vita

2001 B. S. (with honours) Applied Physics and Mathematics, Moscow Institute of Physics and Technology, Moscow, Russian Federation

2003 M. S. (with honours) Applied Physics and Mathematics, Moscow Institute of Physics and Technology, Moscow, Russian Federation

2007 C. Phil. Applied Physics/Photonics, University of California San Diego, La Jolla, CA, USA

2009 Ph. D. Electrical Engineering (Photonics), University of California San Diego, La Jolla, CA, USA

Dissertation Title: “Near-field Characterization of Photonic Nanodevices”

Publications

Peer-Reviewed Journal Publications

1. M. Abashin, K. Ikeda, R. Saperstein, and Y. Fainman, "Heterodyne near-field scanning optical microscopy with spectrally broad sources," Opt. Lett. **34**, 1327-1329 (2009)
2. L. Feng, D. Van Orden, M. Abashin, Q.-J. Wang, Y.-F. Chen, V. Lomakin, and Y. Fainman, "Nanoscale optical field localization by resonantly focused plasmons," Opt. Express **17**, 4824-4832 (2009)
3. M. Abashin, U. Levy, K. Ikeda, and Y. Fainman, "Effects produced by metal-coated near-field probes on the performance of silicon waveguides and resonators," Optics Letters **32**, Issue 17, pp. 2602-2604 (2007)
4. U. Levy, M. Abashin, K. Ikeda, A. Krishnamoorthy, J. E. Cunningham, Y. Fainman “Inhomogeneous dielectric metamaterials with space-variant polarizability”, PRL **98**, 243901 (2007)
5. E. Schonbrun, Q. Wu, W. Park, M. Abashin, Y. Fainman, T. Yamashita, and C. J. Summers, "Imaging the Wavefront Curvature Reversal in Photonic Crystals," Optics & Photonics News **18**, 34-34 (2007)

6. E. Schonbrun, M. Abashin, J. Blair, Q. Wu, W. Park, Y. Fainman, and C. J. Summers, "Total internal reflection photonic crystal prism," Opt. Express **15**, 8065-8075 (2007)
7. E. Schonbrun, Q. Wu, W. Park, T. Yamashita, C. J. Summers, M. Abashin, and Y. Fainman, “Wave front evolution of negatively refracted waves in a photonic crystal” Appl. Phys. Lett. **90**, 041113 (2007)
8. M. Abashin, P. Tortora, I. Märki, U. Levy, W. Nakagawa, L. Vaccaro, H. Herzig, and Y. Fainman, "Near-field characterization of propagating optical modes in photonic crystal waveguides," Opt. Express **14**, 1643-1657 (2006)
9. P. Tortora, M. Abashin, I. Märki, W. Nakagawa, L. Vaccaro, M. Salt, H. P. Herzig, U. Levy, and Y. Fainman, "Observation of amplitude and phase in ridge and photonic crystal waveguides operating at 1.55μm by use of heterodyne scanning near-field optical microscopy," Opt. Lett. **30**, 2885-2887 (2005)

Peer-Reviewed Conference Proceedings

1. M. Abashin, K. Ikeda, M. Ayache, Ro. E. Saperstein, Y. Fainman, " Time-Resolving Heterodyne NSOM with Spectrally Broad Sources," ***NFO10*** paper O86 (2008)
2. M. Abashin, R. E. Saperstein, Y. Fainman, “Heterodyne Near-field Scanning Optical Microscopy with Spectrally Broad Sources”, ***FIO*** **2007**, paper FWU2
3. M. Nezhad, M. Abashin, K. Ikeda, L. Pang, H. C. Kim, U. Levy, K. Tetz, R. Rokitski, and Y. Fainman, ***Proc. SPIE*** Int. Soc. Opt. Eng. 6476, 64760A (2007)
4. M. Abashin, U. Levy, K. Ikeda, A. V. Krishnamoorthy, J. E. Cunningham, Y. Fainman “Devices utilizing Free-Space Optics on Chip”, ***LEOS2006***, paper WY2
5. M. Abashin, U. Levy, K. Ikeda, Y. Fainman, "Influence of the near-field probe on the performance of nanophotonic devices," ***NFO9*** (2006)
6. U. Levy, M. Abashin, K. Ikeda, Y. Fainman “Near field characterization of subwavelength graded index structures for "Free space on a chip" applications” ***NFO9*** (2006)
7. M. Abashin, U. Levy, K. Ikeda, C. -H. Tsai, and Y. Fainman, "Nearfield Investigation of Subwavelength Structured Graded-Index Lens," ***CLEO/QELS*** **2006**, paper QTuA3
8. U. Levy, M. Abashin, K. Ikeda, C. -H. Tsai, Y. Fainman, A. Krishnamoorthy, and J. Cunningham, "Design, Fabrication and Characterization of Subwavelength Based Slab Lens in Silicon," ***NPIS*** **2006**, paper NThA4
9. Y. Fainman, K. Tetz, R. Rokitski, U. Levy, C. H. Tsai, C. H. Chen, L. Pang, M. Nezhad, H. C. Kim, and M. Abashin, ***NPIS*** **2006**, paper NThB1
10. U. Levy, K. Tetz, R. Rokitski, H.-C. Kim, C.-H. Tsai, M. Abashin, L. Pang, M.

Nezhad, and Y. Fainman, ***Proc. SPIE*** Int. Soc. Opt. Eng. 6124, 612404 (2006)

11. M. Abashin, U. Levy, Y. Fainman, P. Tortora, W. Nakagawa, and L. Vaccaro, "Nearfield Investigation of Mode Structure in Photonic Crystal Waveguides," ***CLEO/QELS*** **2005**, paper QTuK3
12. M. Abashin, P. Tortora, U. Levy, W. Nakagawa, I. Märki, L. Vaccaro, M. Salt, Y. Fainman, and H. P. Herzig, " Near-Field Amplitude and Phase Measurements of Photonic Crystal Waveguides," ***FIO*** **2005**, paper FTuV5
13. P. Tortora, M. Abashin, I. Marki, W. Nakagawa, L. Vaccaro, M. Salt, H. P. Herzig, U. Levy, and Y. Fainman, " Investigation of the Spectral Characteristics of Photonic Crystal Waveguides with Heterodyne Scanning Near-Field Optical Microscopy," ***NPIS*** **2005**, paper NThC2
14. Y. Fainman, K. Tetz, R. Rokitski, U. Levy, C. -H. Tsai, C. -H. Chen, L. Pang, M. Nezhad, H. C. Kim, and M. Abashin, ***FIO*** **2005**, paper FTuJ1
15. T. K. Chan, M. Abashin, and J. E. Ford, "2-D Array Waveguide Demultiplexing by Hybrid Waveguide and Free-Space Optics," ***OFC*** **2005**, paper OThV7

ABSTRACT OF THE DISSERTATION

Near-field Characterization of Photonic Nanodevices

by

Maxim Abashin

Doctor of Philosophy in Electrical Engineering (Photonics)

University of California, San Diego, 2008

Professor Yeshaiahu Fainman, Chair

The increasing density of data transmission, speed of all-optical signal processing, and demand for higher resolution microscopy and spectroscopy stimulate the development of the nanophotonics. Near-field microscopy is not limited by light diffraction and thus it can achieve sufficiently subwavelength resolution. Therefore this approach is perfect for nanophotonic device characterization. Heterodyne detection allows resolution of the optical phase and improves signal-to-noise performance in near-field microscopy. In this thesis we describe a Heterodyne Near-field Scanning Optical Microscope (HNSOM) and apply this approach to characterization of several classes of the photonic nanodevices.

First, possible effects of the microscope probe are analyzed and experimentally studied. We show that a metal-coated NSOM probe can introduce loss to the waveguides and change the quality factor and resonant wavelength of the microring resonators. These effects should be taken into account especially for characterization of highly resonant photonic structures.

Then various Photonic Crystal (PhC) devices are studied using the HNSOM. The modal structure of the single line defect PhC waveguide is found and the losses between this component and the channel waveguide are estimated. Using near-field characterization the performance of the self-collimating PhC lattice and the PhC polarization beam splitter are demonstrated.

Another approach in nanophotonic device design is to directly transfer free-space functionality to a chip using metamaterials with refractive index variation on a deeply subwavelength scale. Such materials can be described using effective medium theory and have an index of refraction which depends on the structure period, filling factor and light polarization. Several photonic nanodevices utilizing this approach including a planar graded index lens are created and characterized using the HNSOM technique. The viability of the concept is confirmed in these measurements, some fabrication imperfections are found as well.

The HNSOM setup is further enhanced by adding the low-coherence measurement capability which allows local study of the dispersive properties of the photonic nanodevices. The application of the technique to the characterization of group indices of refraction of silicon waveguides is shown.

1. Introduction

1.1. Historical background

Already in the 17th century people had started to use magnified imaging to study nature. In his report "Micrographia" (1665), English scientist Robert Hooke described observations of single cells in a slice of cork under a microscope with 30x magnification. Several years later in 1675 Anton van Leeuwenhoek discovered single-celled organisms in pond water using his 300x microscope. Since then there has been a constant trend to improve the magnification of the imaging to look deeper in the nature. Abbé in his theory of image formation pointed out the theoretical maximum limits to magnification [1]. The fundamental limit to imaging resolution is caused by the diffraction phenomena and incompleteness of the information collected by the lens; it is also known as Rayleigh criterion [2], which can be found as: $d_{\min} = 0.61\lambda / n \cdot \sin\theta$, where λ is the wavelength of light used for observation, $n \cdot \sin\theta$ is the numerical aperture depending on the index of refraction of sample's environment and the collecting angle of the lens. According to this equation, diffraction-limited tools, such as optical microscopes, cannot resolve sample features with lateral spacing smaller than approximately 200 nm for visible light.

The idea to improve resolution of optical measurements by bringing a subwavelength aperture close to the object of interest was first introduced by Synge in 1928 [3]. He suggested an approach where a strong light source is placed behind the 100-nm opening in metal film. The tiny spot of emerging light could be used for illumination

of the sample under investigation, and thus the optical resolution of such a system will be determined by the size of the aperture. To avoid diffraction broadening of the spot this aperture should be placed in the vicinity of the measurement point, in the so-called near-field region. Synge determined that condition by requiring sample-aperture spacing to be less than the size of aperture, i.e. 100 nm in his case. The image of the sample would be formed by point-by-point transmission measurements implementing scanning aperture or sample. He discussed this idea with A. Einstein and they came to the conclusion that it is very challenging to experimentally realize this kind of apparatus. Theoretical aspects concerning this idea were also confirmed in 1956 by O'Keefe [4]. It turned out that it was quite hard to realize near-field imaging experimentally primarily due to the requirement of precise control of aperture-sample distance during scanning process. Of course it is easier to meet the required conditions in the microwave region thus near-field imaging was first demonstrated for λ = 3 cm. In 1972 Ash and Nicholls showed $\lambda/60$ resolution [5] using Synge's approach. Invention in 1981 of Scanning Tunneling Microscopy (STM) and later in 1986 Atomic Force Microscopy (AFM) suggested ways to control the aperture-sample distance precisely. This led to the re-invention of the Synge's ideas and demonstration in 1983 of subwavelength resolution by two independently working research groups: Dieter W. Pohl and his colleagues working at IBM laboratories [6] and Aaron Lewis with colleagues at Cornell University [7]. Since then Near-field Scanning Optical Microscopy (NSOM), or as it is sometimes called Scanning Near-field Optical Microscopy (SNOM), has become a very popular characterization and investigation tool. It is used in a number of applications where measurements of local properties with nanoscale resolution are crucial. Several review articles [8-12] and books [13, 14] were

published on this topic describing the concept of near-field microscopy in details, as well as improvements introduced to this technique over years.

1.2. Experimental realization of a near-field microscope

A typical NSOM consists of four major parts: illumination source and optics; probe — an element with some nanoscale dimensions (e.g. aperture) influencing imaging resolution; scanning and feedback system, which enables detection at the precise positions on the sample, thus forming an image, and keeps the probe at a constant small distance to the sample (in the near-field region) for all detection points; and the optical detection components which in general transform optical radiation to electrical signals for further analysis.

NSOM probes usually have a conical or pyramidal shape to ensure efficient coupling of light to or from the aperture region and to enable short probe-sample distance for non-flat samples. Typically probes are fabricated from optical fiber by pulling under heat [15] or by etching the end of the fiber in acid [16]. It is also possible to produce the probes by micromachining from silicon nitride and other materials [17]. The probes then can be coated with metals (e.g. Al, Au) using vapor deposition; the aperture in this case is created by cutting the tip using focused ion beam. Using this method probes with apertures of 50-200 nm can be fabricated routinely with a good degree of control. This results in transmission efficiencies on the order of 10^{-6}-10^{-9} depending on the wavelength used. To improve the transmission or to further localize the light spot bowtie or small monopole antennas can be created on the aperture [18, 19]. It is also possible to work

with apertureless probes. In this case a sharp edge of a tip or a nanoparticle works as local scatterer or field concentrator depending on the configuration, the illumination and collection of light is performed in the far-field, but the interaction of the probe and sample is occurring in the near-field. The resolution of such apertureless probes is determined by the sharpness of the tip and usually is better than that of aperture probes, but the recovery of signal from the background is very complicated and signal-to-noise ratio is quite poor [20].

There are several possible optical realizations of the NSOM setup. The classical configuration described by Synge implies that the sample is illuminated by small aperture source in the near-field region. This scheme is called *illumination* configuration when the light transmitted or reflected from the sample is observed in the far-field region (see Fig. 1.1a). Another possibility is to use the same aperture to collect the reflected light, which is called *illumination-collection* (or *reflection*) configuration (Fig. 1.1b). If the sample is illuminated from the far-field region either by using classical diffraction elements (mirrors, lenses, total internal reflection (TIR) prisms, etc) or by using photonic circuitry and then transmitted light is detected through the small aperture then such configuration is called *collection* (see Fig. 1.1c). The typical arrangement of the apertureless NSOM experiment is shown on Fig. 1.1d.

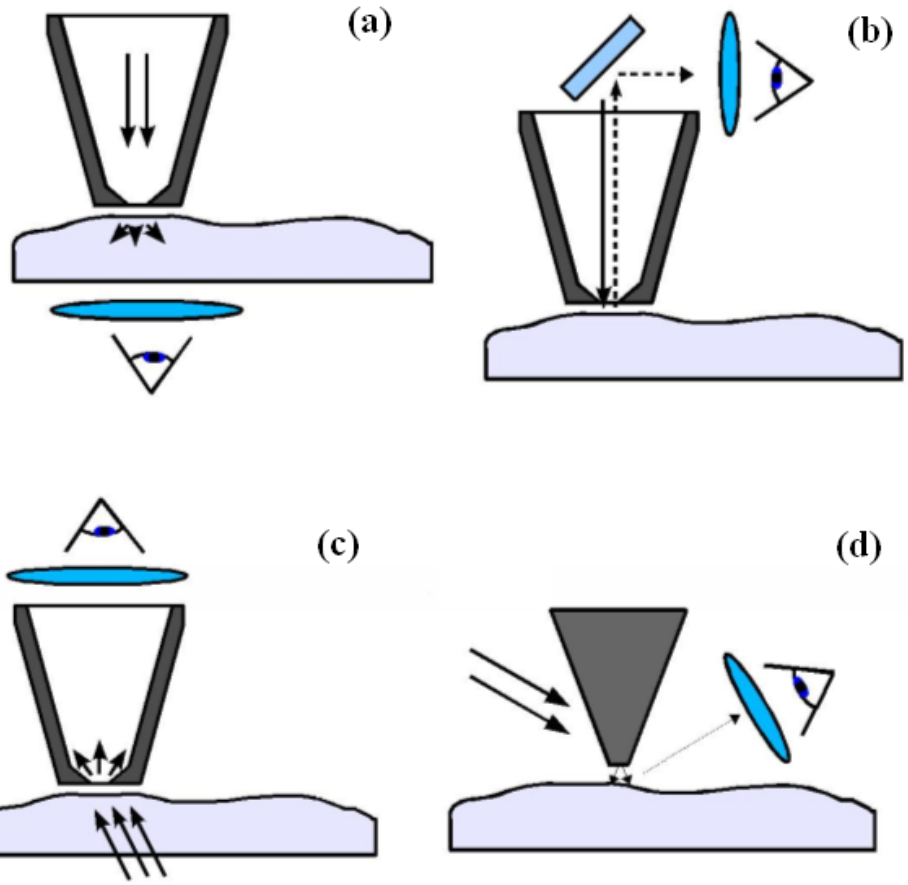

Fig. 1.1. Various arrangements of NSOM optical configuration: (a) near-field illumination; (b) collection-illumination; (c) near-field collection; (d) apertureless NSOM.

Point-by-point image formation is performed using scanners which move either probe or sample. Piezoelectric scanners can provide sub-nanometer resolution over the area of tens of microns, for coarse positioning micrometer stages or motors are usually used. To ensure constant and small probe-sample distance some kind of topography feedback should be used. Most of the NSOM systems now are using atomic force feedback similar to that of used in AFM. Atomic forces become significant when the spacing between the probe and the sample is very small (nanometers to tens of nanometers); they strongly depend on the exact distance and can be attractive or repulsive.

Therefore to keep the same distance throughout the scan one should be able to move the probe relative to the sample and have a feedback loop which keeps constant the measured atomic forces. There are three most common realizations of the atomic force feedback: laser-bounce feedback measuring the bent of the cantilevered probe, tuning fork normal force feedback and tuning fork shear force feedback. The former method (see Fig. 1.2a) is using the fact that cantilevered probe experiences some deformation while affected by atomic forces, thus the laser beam which is reflected from such a probe falls on the different parts of a Position Sensitive Detector (PSD), or quadrant photodiode. The signal from this detector is used to perform topography feedback. The latter two mechanisms (Fig. 1.2b and Fig. 1.2c) are using the fact that when the probe is influenced by atomic forces (their nature is still under discussion, but the most realistic candidates are Van Der Waals forces, capillary forces, dry friction forces and viscous drag) the mechanical resonance of the tuning fork-probe system is affected. By measuring resonance frequency, amplitude of oscillations or phase difference between the modulation voltage and oscillations a proper feedback loop can be established.

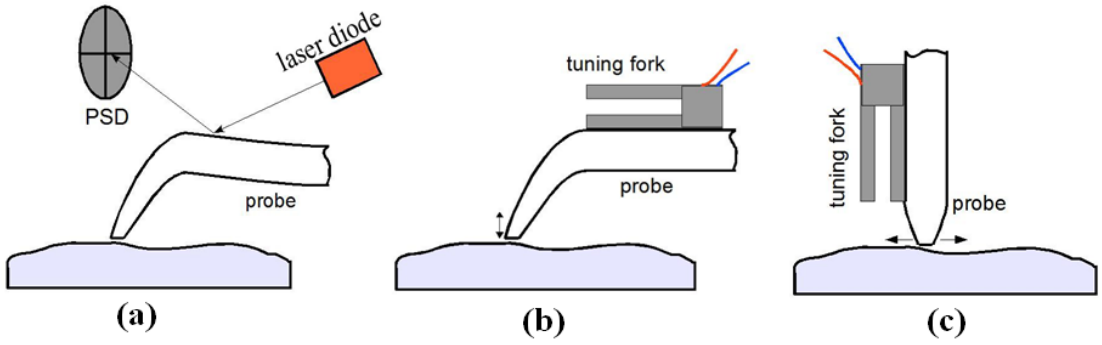

Fig. 1.2. Three types of the atomic force topography feedback for NSOM systems: (a) laser-bounce feedback; (b) tuning fork feedback with normal force; (c) tuning fork feedback with shear force.

Depending on the application, different light sources are used for illumination in NSOM experiments. The efficiency of light transmission through a small aperture ($d << \lambda$) rapidly drops as the aperture size decreases: $T \sim (d/\lambda)^4$ [21], thus for a realistic aperture of 100 nm and visible wavelengths the transmission efficiency only reaches 10^{-6}-10^{-8}[21]. Such small transmission coefficients demands using powerful optical sources (often lasers), efficient detection schemes and detectors.

1.3. Applications of NSOM

Near-field microscopy has a large number of applications in optics, material science, biology, etc. Review papers [8-11] describe the key results and propose literature for further reading. So here I will only highlight the main application fields and shortly discuss the advantages of the NSOM approach for the specific cases.

The local nature of detection process allows characterization of single quantum dots. A particular quantum dot can be found using AFM feedback or near-field imaging and then a series of experiments can be performed. Spectral measurements of a single quantum dot and its dependence on the different parameters such as temperature or magnetic field can be obtained. Temporal parameters such as excited state lifetime can be studied using a pump-probe time-resolving NSOM setup; long term stability or bleaching can be also studied for a particular dot.

The intensity of light emerging from the probe aperture in the illumination NSOM configuration is extremely low, so light sensitive biological systems can be studied using

this technique without any optical damage. The bleaching time of the fluorescent tags can be sufficiently increased in this case too.

The spot size of the illumination NSOM is very low and the piezoscanners positioning the near-field probe can deliver nanometer accuracy, so the same technique can be used for nanofabrication by photolithography. Metal coated NSOM probes can withstand relatively large optical intensities and in the pulsed regime can even allow material ablation from the surface of the specimen [22].

1.4. Motivation and dissertation outline

This thesis describes the application of NSOM measurements for characterization of photonic nanodevices. It discusses validity of such measurements, describes cases where such characterization method is useful, provides several methods of processing the obtained data for studying different parameters, and proposes different improvements to the NSOM setup as well.

The dissertation is organized as follows:

Chapter 2 provides detailed description of the near-field microscope used for subsequent experiments. It also analyses the advantages and drawbacks of heterodyne detection.

Chapter 3 studies the effect of the NSOM probe on the photonic nanodevices under investigation. Preliminary numerical simulations of the probe-sample interaction are followed by experimental analysis of the NSOM probe effect on the silicon waveguide and microring resonator.

Chapter 4 consists of several experiments studying properties of Photonic Crystal waveguides and other components. It also provides explanation of the Fourier analysis method in application to the modal analysis of propagating light.

In Chapter 5 the concept of dielectric metamaterials for Free-space-on-a-Chip applications is introduced. Possible designs of the metamaterial optical components are discussed and the results of the measurements of the Graded Index (GRIN) planar lens are analyzed.

Chapter 6 introduces a new concept of broad-spectrum sources for near-field characterization of dispersive properties of photonic nanodevices. We also use this approach for measurements of the group indices of the silicon waveguides.

Chapter 7 concludes the dissertation with the summary of contributions and proposes future directions for continuation of the research in this direction.

2. Heterodyne NSOM setup and measurement technique

2.1. Description of the experimental apparatus

In our experiments we are using a Heterodyne NSOM (HNSOM) that is based on the commercially available MultiView-2000 head produced by Nanonics Imaging Ltd. (Israel) [23]. This instrument has two sets of three-axis computer-controlled translation stages for independent positioning of the specimen and the probe. By means of the bottom scanner one can move the sample with respect to the light coupling system. Once the optimum coupling has been obtained, one can move the probe above the area of interest and scan the probe to obtain the image with the independent upper scanner. Piezoelectric scanners allow sub-nanometer-resolution in probe positioning over the sample area of 70 x 70 μm and topography feedback using normal force AFM response of the cantilevered tip mounted on the tuning fork (Fig. 2.1a). NSOM tips were also purchased in Nanonics Imaging Ltd. [24]. They are manufactured there from single-mode SMF-28 optical fiber [25] by pulling heated fiber end, thus creating a taper; bending it and then covering with metal (Al or Au). The aperture is created at the tip of the probe (Fig. 2.1b) by using focused ion beam milling. The diameter of the aperture can range from 50 to 250 nm. We mostly use 100-200 nm-aperture tips in our experiments as they provide a good compromise between signal-to-noise ratio (SNR) and image

resolution. The aperture diameter is approximately equal to image resolution, which for our operating wavelength is better than $\lambda/7$.

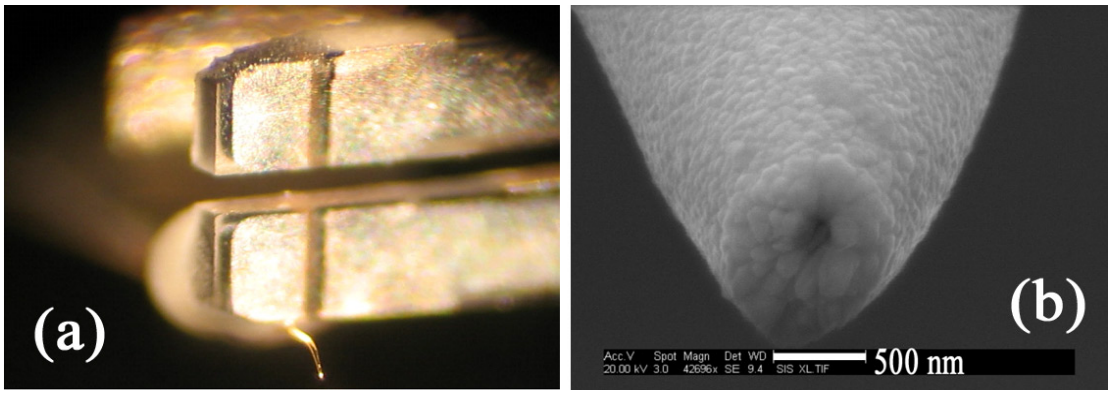

Fig. 2.1. (a) Photograph illustrating NSOM probe attachment to the tuning fork; (b) scanning electron microscopy (SEM) micrograph of the tip showing aperture (darker circle) in the metallic coating.

Probe scanning process was governed using TOPAZ controller and Quartz software provided by Cavendish Instruments. Later the controller was switched to the newer version Integra, which is working with LabView-based NanoWorkShop software.

The described NSOM setup was incorporated in one arm of an all-fiber Mach-Zehnder interferometer (Fig. 2.2) to allow heterodyne detection [26]. This approach enables measurements of extremely low-power optical signals collected through the small aperture of the probe by providing amplification of a coherent detection process. Another advantage of such scheme is the sensitivity to the optical phase since the interference term is detected. The interferometer is composed of readily available telecom components: 10/90 and 5/95 directional couplers, fiber-pigtailed Acousto-Optic Modulators (AOMs), and polarization controllers. The couplers are arranged in such way that they favor the optical power coupling to and from the signal arm.

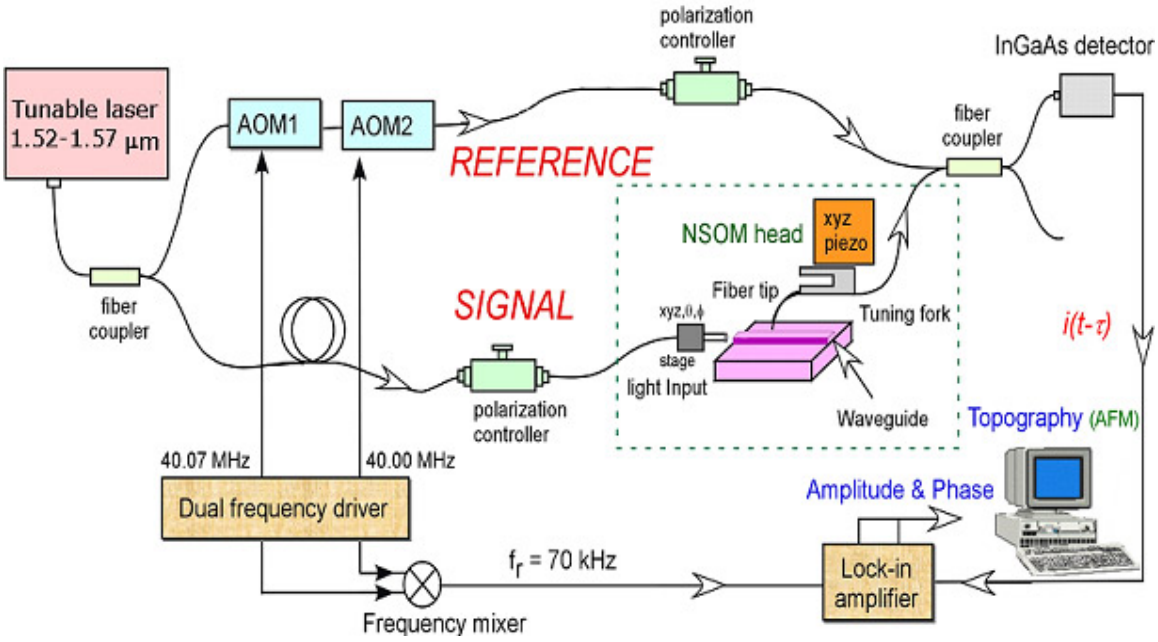

Fig. 2.2. Scheme of the HNSOM setup with the collection system for effect of the tip analysis.

The reference arm consists of a pair of AOMs integrated with single mode fiber and connected in cascade. The first AOM is upshifting the optical frequency by 40.07 MHz and the second one is downshifting the optical frequency by 40 MHz; therefore as a result we have optical frequency in the reference arm shifted by 70 kHz with respect to the optical frequency in the signal arm. The signal acquisition arm of the interferometer consists of a polarization controller and a polarization maintaining lensed fiber used for coupling light into the nanophotonic device under test, the tested device itself, and a near-field probe mounted on a scanning manipulator. The optical fields collected through the near-field aperture are then combined with the optical field from the reference arm using the directional coupler, which produces an interference signal oscillating at heterodyne frequency. The obtained field is introduced onto the photodetector for heterodyne detection and signal processing to extract the amplitude and the phase of the detected

near-field optical signal in addition to the topology image simultaneously obtained by the AFM feedback. The optical detector is connected to a Stanford Research Systems SR530 lock-in amplifier which is also fed with the signal from the RF mixer (70 kHz electrical reference). Amplifier outputs are the amplitude and the relative phase of the detected signal to the reference. These two signals along with the AFM feedback parameters are transmitted to the computer via an analogue-to-digital converter for further analysis and recording. To improve the interferometric stability of the setup the head and the fiber optics arrangement are covered with custom-made plastic boxes.

2.2. Principle of heterodyne detection

Interferometric detection was first reported in as early as 1955 [27] even before the advent of lasers. Later it was shown [28] that the heterodyne technique provides improvement of SNR in detection. Another advantage of interferometric detection is sensitivity to the optical phase. Photodetectors are only sensitive to the photon flux and the phase information is lost in direct detection, but coherent phenomena, such as interference, transform phase difference in optical waves to amplitude variations, thus providing an efficient method of more detailed characterization of photonic phenomena.

The concept of heterodyne detection is to mix the signal of interest with a coherent reference beam possessing slightly shifted optical frequency. Relating to the Fig. 2.2 the signal detected by the near-field probe depends on the position of the tip with respect of the device under study:

$$E_S(x,y) = A_S(x,y)e^{j[\omega_0 t+\phi_S(x,y)+\beta_S]} \qquad (2.1).$$

Note, that the vertical tip-sample gap in our experiments is constant and is approximately zero ($z \approx 0$ for contact mode scanning), the scan coordinates are x and y, and both signal's amplitude and phase depend on the probe position. The heterodyne frequency, $\Delta\omega$, spectrally shifting the field in the reference arm, is set by the two AOMs driven from two phase-locked radio frequency (RF) oscillators and arranged to operate in the positive and negative diffraction orders, yielding the optical field in the reference arm

$$E_R = A_R e^{j[\omega_0 t + \Delta\omega t + \beta_R]} \qquad (2.2),$$

where $\Delta\omega$ in our experimental setup is set to 70 kHz, which is sufficient to avoid the significant $1/f$ noise, but simultaneously lies within the bandwidth of the InGaAs high-sensitivity photodetector. The two fields given by Eq. 2.1 and Eq. 2.2 are added coherently, yielding intensity:

$$I(x,y) \sim A_R^{\,2} + 2A_S(x,y)A_R \sin\left[\phi_S(x,y) + \Delta\omega t + \beta_0\right] + A_S^{\,2} \qquad (2.3),$$

where the first term represents a constant bias, the second term contains the desired interference signal of interest oscillating at the heterodyne frequency, $\Delta\omega$, and the term proportional to $A_S^{\,2}(x,y)$ can be neglected since $A_R >> A_S$. This equation assumes that the beams are perfectly coherent and the polarization of light in the two arms is the same; if this is not true, then the portion of the signal with polarization perpendicular to the reference is essentially lost.

The lock-in amplifier has a reference input which is fed with the output of a frequency mixer providing the difference frequency between two signals driving AOMs $\Delta\omega$ = 40.07 MHz - 40 MHz = 70 kHz. The electrical circuitry of the amplifier produces two additional internal references:

$$U_X \sim U_R \sin[\Delta\omega t + \beta_E] \quad (2.4a)$$

and

$$U_Y \sim U_R \cos[\Delta\omega t + \beta_E] \quad (2.4b),$$

where U_R is the amplitude of electrical signal $U_R \sim 2A_S(x, y)\, A_R$, and β_E is the phase delay in the electrical circuits. From equations (2.4a) and (2.4b) it is easy to see how in lock-in amplifier electrical signals are processed to provide separate outputs corresponding to the amplitude and phase of the detected light:

$$V_A(x, y) \sim \left(U_X{}^2 + U_Y{}^2\right)^{1/2}$$

and

$$V_\phi(x, y) \sim \arctan[U_Y / U_X]$$

which are proportional to the $A_S(x, y)$ and $\phi_S(x, y)$ values respectively.

The advantage in using heterodyne detection can also be seen from Eq. 2.3, demonstrating how coherent amplification improves detection of extremely weak near-field signals. In contrast to the conventional NSOM systems that use direct detection of the weak intensity signal collected by the near-field tip, $A_S{}^2(x, y)$, we detect an amplified value, since $A_R >> A_S$. The coherent gain of the HNSOM system is estimated by $G_C \sim A_R A_S / A_S{}^2 = A_R{}^2 / A_R A_S = P_{DC}/P_{AC} \sim 10$ V/1 mV = 10^4. Moreover, a lock-in amplifier, with reference given by the difference frequency from the two AOM drivers, can be used to further enhance the detected near-field signal by rejecting noise outside the narrow pass band centered at $\Delta\omega$. For our typical experiments the lock-in amplifier increases the signal from 1 mV to 10 V providing additional improvement factor of 10^4. Thus the total

gain of our HNSOM system is 10^8. Most importantly, the detected heterodyne signal allows separate measurement of the amplitude and the phase of the collected near-field signal, providing the complex amplitude information of the nanophotonic device under investigation.

Note that the ability of HNSOM system to detect near-field optical phase of the nanophotonic devices enables quantitative experimental measurement of various important parameters including phase velocity, effective index of refraction, etc. Furthermore, by combining the optical phase information with the amplitude of the detected fields, it is possible to perform spectral analysis of the near-fields by performing Fourier transformation of the detected complex amplitude, providing measured modal content of the propagating optical fields. Signal-to-Noise Ratio (SNR) for the typical measurements can reach 40 to 60 dB at maxima of amplitude, thus according to [29] $\delta\varphi = 1/\sqrt{SNR}$ corresponding to the phase measurements accuracy of about 0.57 to 0.06 degrees, respectively.

2.3. Near-field characterization of nanodevices

To test the performance of the HNSOM we study light propagation in a simple nanodevice such as a silicon-on-insulator (SOI) channel waveguide. The waveguide has a rectangular cross section of 290 nm x 10 μm and is sitting on top of the 1 μm-thick silicon dioxide layer of a silicon wafer. The process of the HNSOM characterization is as follows: the sample is placed below the piezoelectric scanner with the attached near-field probe. Then a lensed fiber is used to couple the light into the waveguide. This fiber

concentrates light into a 2.5 µm focal spot, which improves the coupling efficiency. In the vertical direction dimension of the waveguide is still much smaller than the focal spot, thus inevitable free-space propagating light can affect our measurements. To avoid the parasitic light in the investigation area L-shaped waveguides can be used, where the injection of light is performed in one section and the measurements are taken on the other straight section around the corner. The lensed fiber is aligned for optimal coupling; this can be checked by measuring intensity of light at the output or sometimes by imaging the device from the top. Polarization of the light can be adjusted using the polarization controller, to simplify control and adjustments in-fiber polarizer can be used after controller. Following the alignment procedure the tip is approached to the near-field region of the device and performs scanning while the topography feedback ensures that the tip does not exert excessive force to the sample (does not crush into the geometrical features). Typical scan resolutions are 128x128 or 256x256 points with the acquisition time at each point of 3-30 milliseconds, and it takes 2-5 minutes for low resolution images up to 20-40 minutes for higher resolutions with longer point acquisition time.

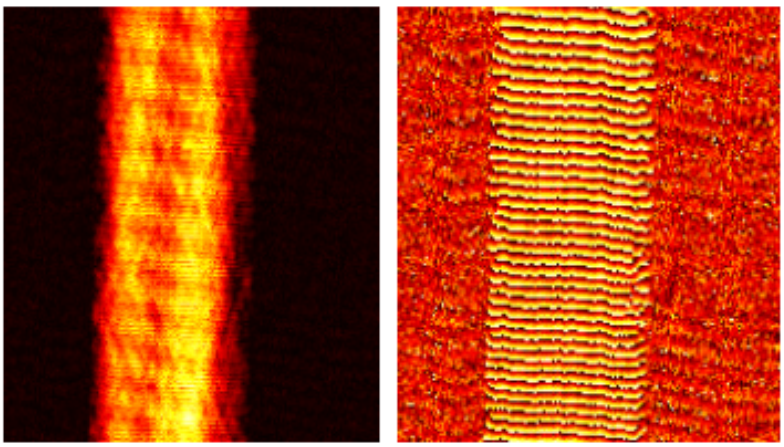

Fig. 2.3. Near-field distributions of the amplitude (left) and phase (right) above the waveguide. The sections are 25 µm (along the waveguide) x 20 µm (wide).

Obtained near-field images show amplitude and phase distributions (Fig. 2.3) on the surface of the sample (or within several nm distance from it), since we operate in contact mode of topography feedback. Phase distribution images can be used to calculate the effective refractive index of the waveguide. The average spacing between phase fronts in Fig. 2.3 is λ_{eff} = 640 nm, which for coupled light with free-space wavelength λ = 1550 nm gives n_{eff} = 2.4, a realistic value for TM-polarization mode (E-field vector is perpendicular to the wafer plane). Theoretical prediction gives n_{eff} = 2.5 for the fundamental TM-polarized mode [30], which gives a good match (within 5%) to our experimentally obtained results.

3. Influence of the near-field probe on the measurements

3.1. Action of the probe on the investigated device

In conventional microscopy the interaction between the observing tool (microscope) and the specimen is essentially one-way – the observation process does not affect the sample. For near-field microscopes it is essential that the probe should be brought very close to the sample, and thus we can no longer ignore the action of the probe on the device under study. The first investigations of the effects of the probe vicinity on the image formation for reflection NSOM were made in the 90's [31, 32], but the effects of the probe on device under study itself were not discussed in broad before 2005 [33], when the theoretical aspects of the probe influencing a waveguide and planar Bragg grating are discussed. In general this research is greatly dependent on the experimental arrangement; this motivated the investigation of this phenomenon using our NSOM setup and typical samples.

First, to predict the possible effects, finite element method (FEM) numerical simulations were performed for a simple silicon waveguide on silicon dioxide cladding layer assuming SOI material system. Due to computational complexity associated with combination of small skin-depth of metallic overcoating of the tip that requires high resolution, and a large scale of the waveguide length, only two-dimensional (2D)

modeling was used. The parameters of the device were chosen to be compatible with typical values of the fabricated SOI sample: height of silicon layer h = 300 nm on top of 3 µm thick layer of silica (SiO_2); the free-space wavelength λ = 1.55 µm. The tip geometry used was: diameter at the apex before coating of 400 nm, taper angle of 30 degrees, Aluminum coating of thickness 200 nm with material constants from FEMLAB data, and opening (i.e., uncoated aperture) of 200 nm. These parameters are typical values provided by the manufacturer of the tips (i.e., Nanonics Ltd.), and confirmed by our scanning electron microscope (SEM) micrographs (Fig. 2.1b).

For comparison, the same geometry with tips of identical geometry but without Al coating was also modeled. These pure dielectric tips are expected to have much smaller effect on the guided optical fields, but in general at the expense of providing much smaller signal caused by their weaker scattering capabilities. In fact we could not get any signal from those tips in our cantilevered configuration possibly due to large waveguiding loss through the small-radius bend.

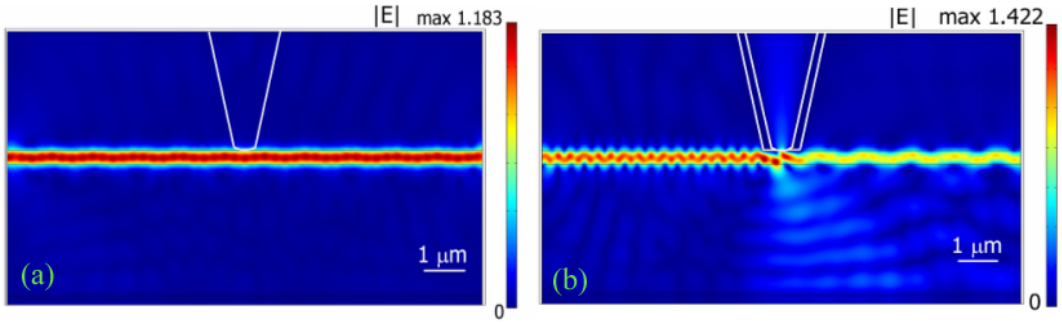

Fig. 3.1. Results of the FEM simulations showing TE-polarized field within a silicon waveguide: (a) with uncoated glass tip; (b) with Al-coated tip. Tip-sample gap is assumed to be 0 nm (contact mode).

The modeling results for uncoated and coated near-field tips are shown on Fig. 3.1 (a) and (b) respectively. The uncoated tip has very little effect on the optical field propagating in the waveguide, whereas the coated tip significantly perturbs the propagating optical mode in the silicon waveguide. The presence of the tip causes a significant propagation loss caused by out-of plane radiation and back-reflection, which can be crucial for active nanophotonic devices. The effect of the metal coating is expected since the refractive index of the metal (primarily its imaginary part) is much larger than that of the waveguide cladding (i.e., air). Quantitatively, FEM simulations predict that the coated tip brought in contact with the waveguide, introduces approximately 1.2 dB loss in amplitude (or 2.4 dB in intensity) and 0.6 rad phase shift to the optical field at the output of the waveguide. The influence of the uncoated tip with the same geometry is negligibly small and cannot be quantified within the accuracy margins of our numeric simulations; however we also observed that the intensity of light coupled to the uncoated tip is much lower.

3.2. Experimental investigation of probe effects on the silicon waveguide

For experimental study of the probe effects an L-shaped SOI channel waveguide with cross section height of 280 nm and width of 500 nm cleaved at the input and output facets was used. Lensed polarization maintaining fiber was coupling into the waveguide input light with TE polarization (E-field in plane of the sample); the output radiation was collected with a similar lensed fiber (Fig. 3.2).

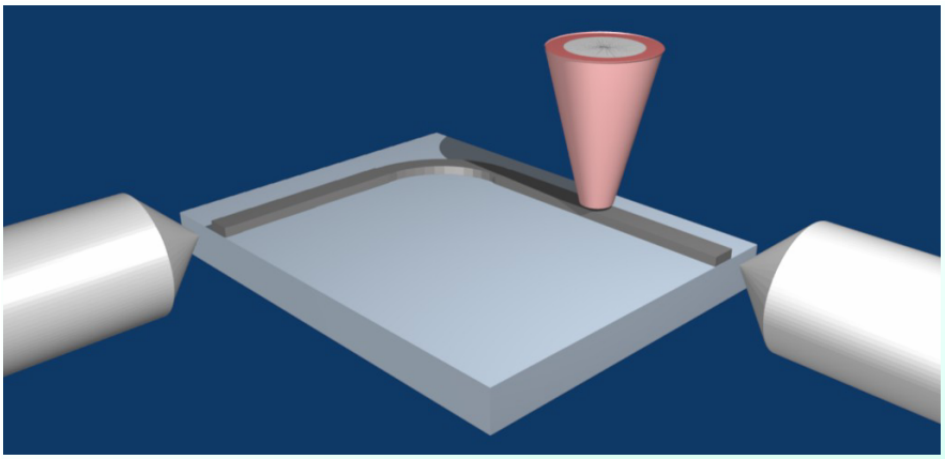

Fig. 3.2. Schematic diagram describing the experimental geometry for studying the effect of the tip on the silicon channel waveguide.

The transmitted light was used to experimentally analyze the influence of the tip on the transmission properties of the waveguide. Note that during these experiments the complex amplitude of light collected by the lensed fiber at the output of the waveguide was analyzed using our heterodyne detection system. The output of the waveguide was monitored in real time while the NSOM tip was scanning the structure in the transverse direction, perpendicular to the direction of the propagating mode. The experimental results are summarized in Fig. 3.3 showing the amplitude of near-field collected by the tip (Fig. 3.3a), the amplitude (Fig. 3.3b) and phase (Fig. 3.3c) of the waveguide output, with respect to the tip position ***x***.

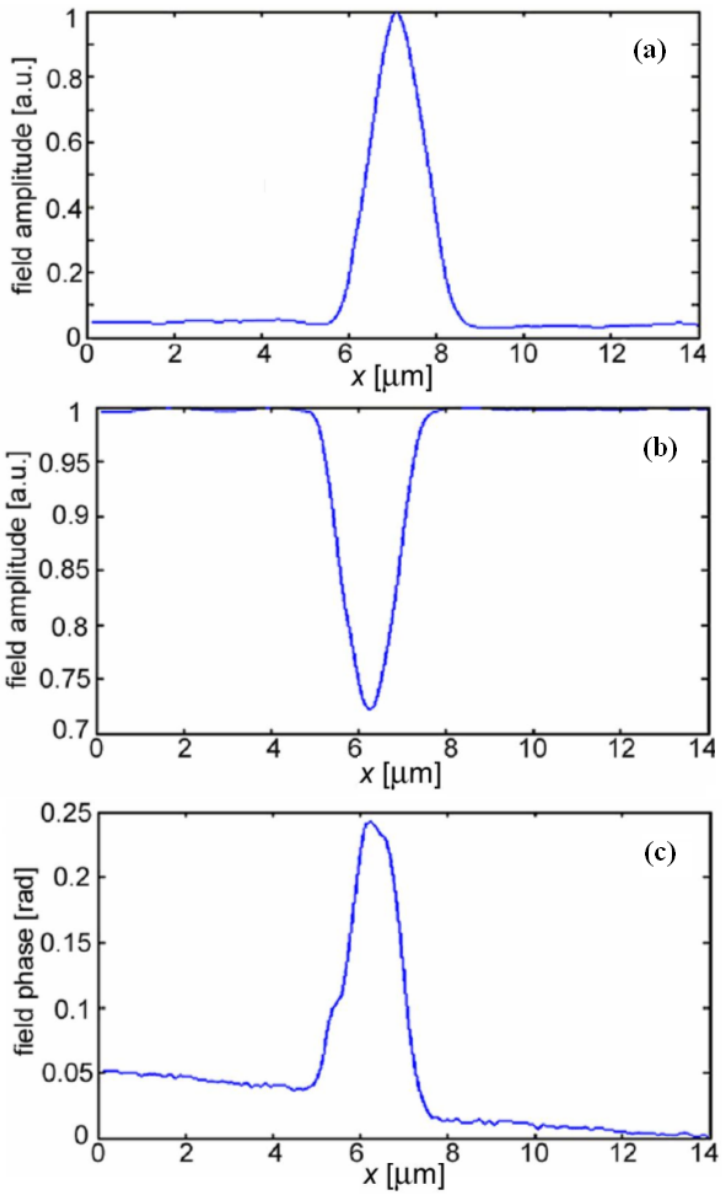

Fig. 3.3. Effect of the position of the tip on the collection of the near-field amplitude and the complex amplitude of the transmitted guided field: (a) amplitude of the optical field collected by the tip, (b) amplitude of the optical field at the output of the waveguide, (c) phase of the optical field at the output of the waveguide (in radians) vs. position of the tip.

The measured effect of the scanning tip on the loss in transmitted guided wave amplitude (see Fig. 3.3b) is about 1.5 dB corresponding to a 3 dB intensity loss. This result is in close agreement with our numeric modeling results predicting intensity loss of

about 2.4 dB for the assumed 2D geometry. The measured phase shift reaches a maximum of about 0.2 rad (see Fig. 3.3c). For the reflection measurement an additional 3 dB directional coupler was introduced before the lensed fiber that couples light into the waveguide. No modulation was observed in the reflected signal when the near-field tip was scanning the sample. One possible reason is lower SNR in the measurement of the reflected field since the near-field tip simply causes scattering that has extremely weak coupling to the waveguide modes. Near-field imaging of the device with uncoated tips was not feasible, primarily since the small (if any) amount of the light coupled at the apex was flooded with the free-space propagating light coupled by other parts of the probe (thus no meaningful information could be gathered). It is also evident that using uncoated tips with silicon nanophotonic devices is not very practical since the refractive index of glass is small compared to silicon, and thus they do not always provide frustration of propagating fields to the tip via evanescent coupling (as an example see the overcladding of the silicon devices with silica, which in fact reduce losses, by reducing coupling the light out of the waveguides). In contrast, metal-coated tips produce large scattering, but this simplifies probing of evanescent fields of devices on SOI substrates.

3.3. Probe effects on the silicon microring resonator

The presence of optical feedback in resonant photonic devices causes multiple interactions between the propagating field and the near-field tip; hence a significant enhancement in the effect of the tip on the performance of these nanophotonic devices can be expected. The previous section shows that the tip introduces a phase shift into the

propagating optical field and therefore one can predict a change in the resonance conditions, resulting in a shift of the resonant frequency and a change of the transmission amplitude. In addition, since the tip introduces loss, the quality factor of the resonator (*Q)* is expected to decrease as the tip scans the resonator device. These issues can lead to unreliable NSOM measurements of resonant nanophotonic devices.

For experimental validation of the effect of the tip on resonant devices silicon microring resonators can be used (see Fig. 3.4). The geometry of our resonant device has waveguide dimensions comparable to those used in the waveguide experiments, i.e. height of 280 nm and width of 500 nm. The microring radius and the gap between the bus waveguides and the microring are 5 μm and 250 nm, respectively. We performed experiments similar to those we did for the silicon waveguide using the bus waveguides (see the sample geometry on Fig. 3.4b). Throughput power was measured with and without Al-coated tip in a stationary position above the waveguide and also during the scanning process of the tip (see the diagram Fig. 3.4a).

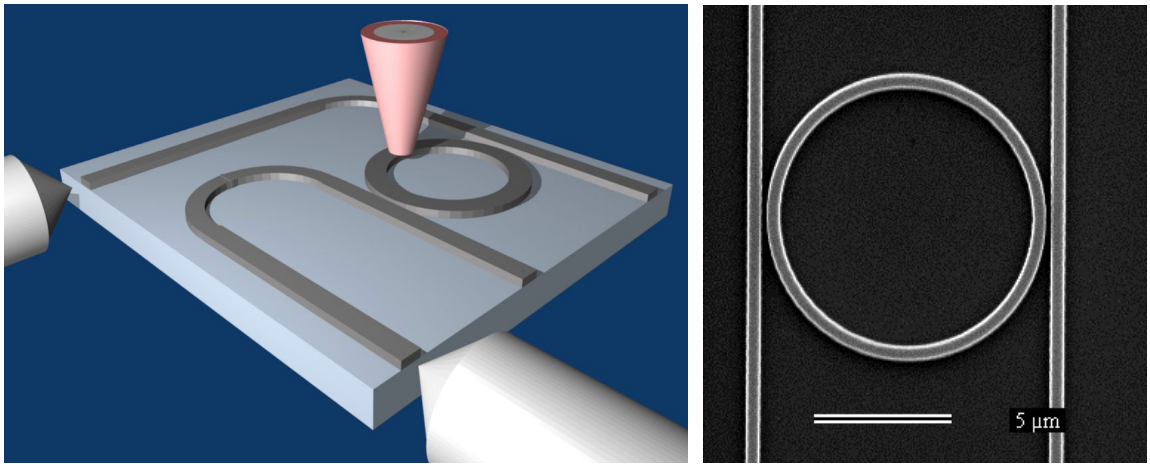

Fig. 3.4. (a) Schematic diagram describing the experimental geometry for studying the effect of the tip on the silicon microring resonator; (b) SEM micrograph of a microring resonator coupled to bus waveguides

Results of the HNSOM microring resonator investigation are summarized in Fig. 3.5. When the wavelength of light is resonant with the ring resonator, the field is coupled from the input bus waveguide to the output bus waveguide via the microring and is collected by the lensed fiber (Fig. 3.5b). It was found that at a fixed wavelength, as the tip scans the bus waveguides the output intensity always decreases, due to introduced losses similar to those observed in our experiments with a simple straight waveguide. However, when the tip is scanning above the microring, either increase or decrease of the transmitted light is observed depending on the wavelength of propagating light, which indicates that the tip causes a shift of the resonant wavelength (Fig. 3.5d).

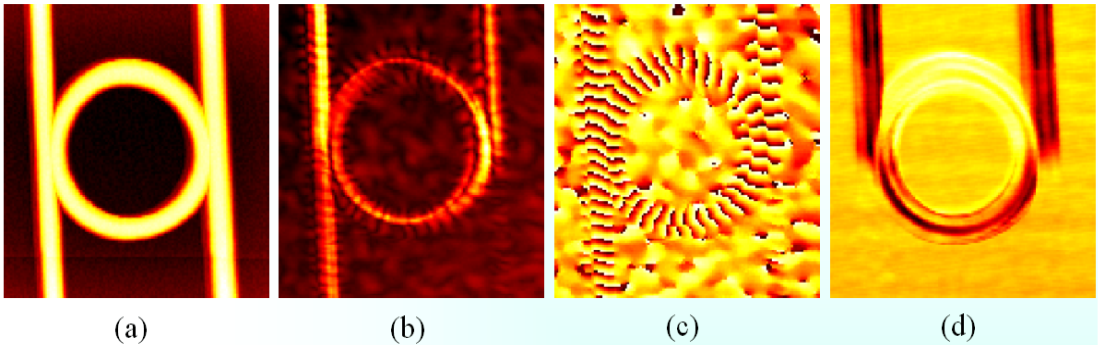

Fig. 3.5. (a) Microring resonator topography obtained in NSOM measurements; (b) and (c) near-field amplitude and phase distributions (respectively), obtained for resonance free-space wavelength of λ=1535 nm; (d) Example of output amplitude for different probe positions collected during the scanning process.

Spectral transmission data for the unperturbed microring resonator and for the microring resonator with the near-field probe in contact with different points of the device are given in Fig. 6.

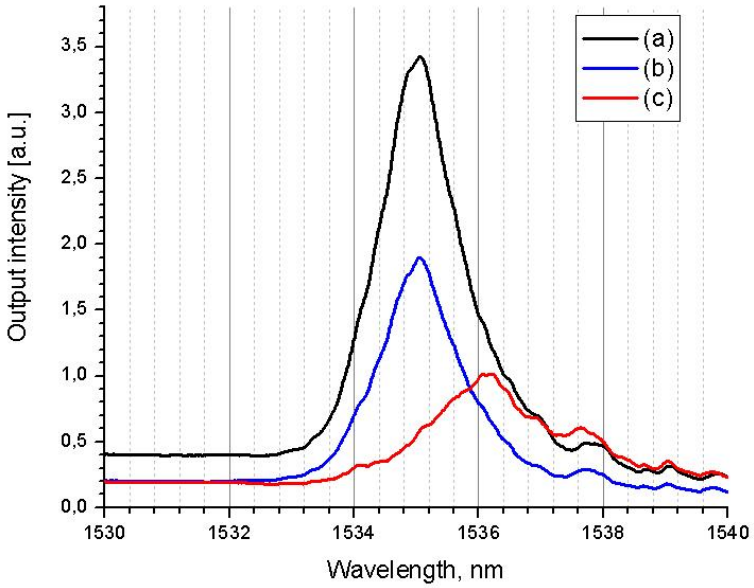

Fig. 3.6. Spectral characteristics of the ring resonator device: (a) the probe is above the non-guiding parts of the device, (b) the probe is above the bus waveguide interfacing to the microring and the drop port waveguide, (c) the probe is above the microring.

The resonance in the unperturbed device occurs with a center wavelength of 1535.1 nm (when the near-field tip is outside the device region). Furthermore, when the tip is located above the bus waveguide, it has no effect on the center wavelength of the resonance. However, when the near-field tip is located above the microring resonator it introduces a shift to the phase of the propagating light, and thus the resonant wavelength is shifted to a longer wavelength of 1536.1 nm. In addition to the redshift in resonance wavelength we also observed a significant decrease in *Q*-factor which results from the additional loss introduced by the tip. This effect can be evaluated from the relation:

$$\frac{1}{Q} = \frac{1}{Q_{wot}} + \frac{1}{Q_{tip}},$$

where Q_{wot} is the quality factor of the microring resonator without the presence of the tip, and $Q_{tip} = \frac{4\pi^2 R n_{eff}}{\alpha_{tip}\lambda_0}$ is the quality factor associated with the power loss resulted by the tip (α_{tip}); R is the microring radius, n_{eff} is the effective refractive index of the Silicon waveguides and λ_0 is the resonant wavelength. From the difference in peak transmission between curves (a) and (b) on Fig. 3.6 we estimate α_{tip} to be around 0.42, using n_{eff} = 2.75 (typical value for similar geometry and TE polarized light) we obtain Q_{tip} ~ 820. The width of the resonant peak is about 1.4 nm, from which we estimate Q_{wot} to be ~ 1100. Therefore, the overall quality factor for curve (c) is expected to be around 470. From Fig. 3.6 we estimate the width of the resonance peak to be about 3.2 nm (including the ripple), giving experimental quality factor of about 480, very close to the predicted value.

3.4. Validity of NSOM measurements

So the NSOM probe can modify the properties of the studied device during the measurements. Specifically it was shown, that for the straight silicon waveguide metal-coated tips can introduce 3 dB intensity loss and 0.2 rad phase shift. For a 10-µm-diameter microring resonator, the tips can induce 1 nm shift of resonant wavelength and decrease resonator *Q* from 1100 to 480. As a result, for reliable measurements the effect of the tip needs to be considered especially in some particular cases. For the non-resonant devices the effect of the probe is spatially similar and the tip does not influence light propagation before the point of measurement. Thus the effect can be factored out and the measurements, for example propagation loss estimation, can be performed without accounting for the perturbations. Other measurements, such as mode profile analysis, should probably take into account the geometry of the probe (thickness of metallic coating) and at least some comparison to the numerical simulations should be performed to understand if the obtained experimental data are valid. For highly resonant devices the effect of the tip in NSOM measurements should be studied and accounted for in experiments as the probe greatly influences the parameters of the device.

Although the effect of the tip can be significantly reduced by using uncoated tips, such probes are typically undesired because of their low coupling efficiency and higher sensitivity to scattered light. Moreover, for characterization of high-index devices (such as SOI), uncoated tips cannot always provide evanescent coupling (tunneling) of the fields propagating in the nanostructures.

4. NSOM measurements of the photonic crystal devices

4.1. Photonic crystal concept

Photonic crystals (PhC) are materials with periodically changing refractive index which provide conditions for photon Bragg diffraction. These structures influence photons similarly to how the atomic lattices of semiconductor crystals affect properties of the electrons, which was first noticed by Yablonovich and John in 1987 [34, 35]. One of the key features of PhC structures is the possibility to have band gaps in which propagation of light with certain wavelengths is forbidden, in the same way that semiconductors have gaps between the conduction and valence energy bands. To achieve Bragg conditions the spatial period of index variation should be approximately equal to a half the effective wavelength of light inside the medium. The width of the photonic band gap (PBG) depends on the amount of index variation (index contrast). Introducing defects in the crystal structures creates localized photonic states in the forbidden gap. The properties of such states depend on the nature of the defect: values of the dielectric constants (i.e., materials involved) and the shape of the defects. Using this concept it is possible to create materials with extraordinary optical properties and wide possibilities for engineering [36]. One-dimensional (1D) PhC has been known for a long time [37, 38] and it is widely used for dielectric mirrors, in active photonic devices with distributed

feedback, etc. With the development of fabrication techniques two-dimensional (2D) PhC manufacturing became feasible. Such devices are promising for planar optics and on-chip optical signal processing. At this point PhC research is still at the components level – properties of waveguides, resonators, prisms, etc. are studied. It is worth mentioning that the PhC concept brings several advantages to on-chip photonic devices: waveguides can provide sharp bending with low loss, resonators can concentrate large optical intensities in small volumes, and prisms provide extraordinary large dispersion.

4.2. PhC waveguide

A waveguide can be created in the photonic crystal lattice by making a defect in the periodic lattice. In collaboration with Swiss Institute of Micro Technology at University of Neuchatel we studied devices based on this principle. These samples are based on a square mesh PhC lattice with a period of a = 496 nm, air holes of radius r = 190 nm, and a membrane thickness of t = 290 nm (see Fig. 4.1). W1 PhC waveguide in our experiments is created by removing (on a lithographic patterning stage) a single row of air holes (here W1 stands for a PhC waveguide with one missing row of holes). The total length of the fabricated waveguide is about 25 microns. The device is made from an SOI wafer by electron beam lithography of PMMA resist for patterning, followed by reactive ion etching to transfer the pattern into the substrate. The oxide layer below the PhC structure was undercut using a buffered hydrofluoric acid vapor etching, thereby creating a free-standing membrane in the PhC region. With this configuration a symmetric mode in the vertical direction can be obtained, and the radiation loss is reduced significantly.

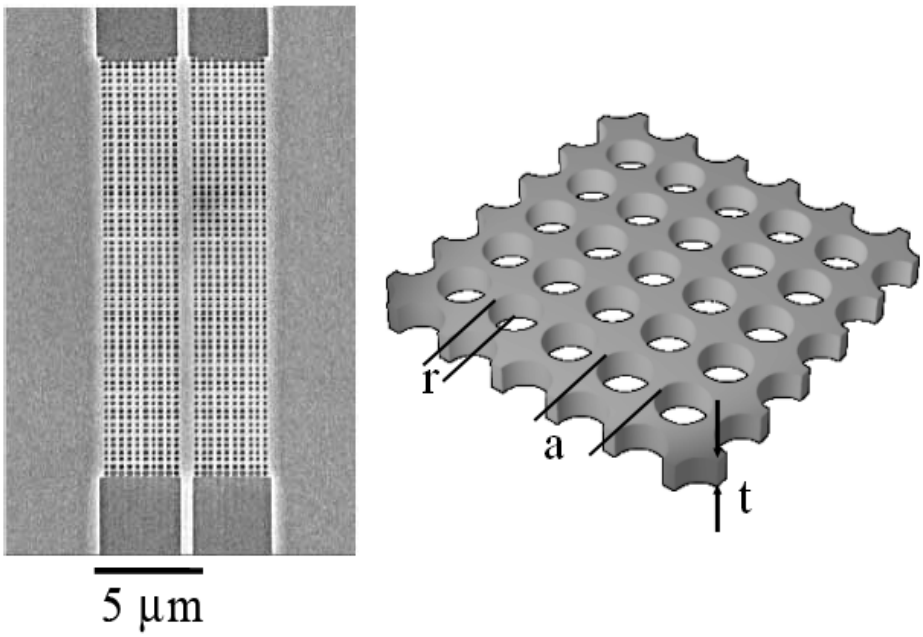

Fig. 4.1. Description of the device: SEM micrograph of the waveguide in PhC membrane (left); drawing illustrating geometry of the PhC lattice (right).

Maxwell's equations can be solved for the modeled structure with any desired degree of accuracy. Using Maxwell's equations in a form comparable to Schrödinger's equations which was used to study the electron properties in solids can also be applied to the study of photonic states in the PhC [39]. Since photons, unlike electrons, are non-interacting particles, the equation solutions do not rely on approximations and thus numerical problems can be solved exactly.

The expected dispersion diagram for the TE-like modes of this PhC structure was numerically determined [40] using a fully three-dimensional calculation based on a plane-wave expansion method [41]. The results of this analysis are summarized in Fig. 4.2: solid black lines represent the guided defect modes (labeled e1, e2, e3, and e4); the dark gray shaded regions in Fig. 4.2 represent modes that can propagate through the crystal (i.e., no confinement by PhC lattice). In the vertical direction the light is confined

by the difference in the refractive indices of the silicon patterned slab and of free space. The light line is introduced in Fig. 4.2 to define the boundary between the leaky and propagating modes: modes above the light line are not confined in the slab whereas modes lying below the light line are guided; the blue shaded region in Fig. 4.2 shows the approximate measurement region (determined by the wavelength range of the tunable laser used).

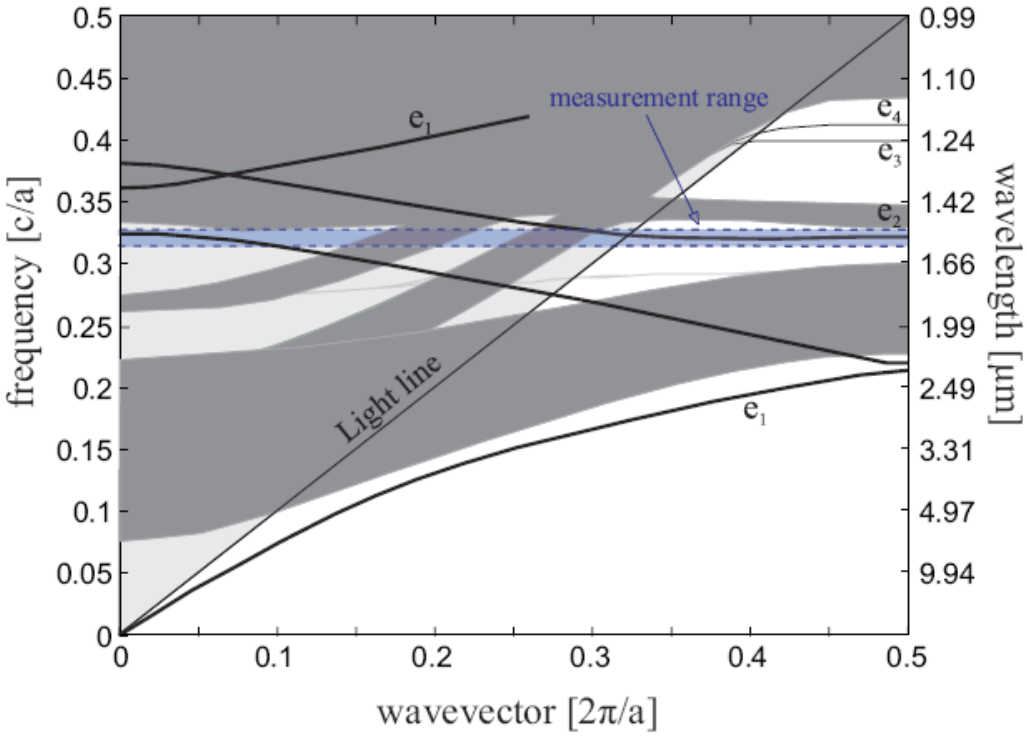

Fig. 4.2. Calculated dispersion diagram for TE-like guided modes in the photonic crystal waveguide. Solid black lines represent the guided defect modes; the dark gray shaded regions show modes that can propagate through the crystal; the light line defines the boundary between the leaky and the propagating modes; the blue shaded region between dashed lines shows the measurement region determined by the source 1520-1570 nm.

The dispersion diagram shows that in the 1520-1570 nm wavelength region there are two guided modes possible – e_1 and e_2. Mode profiles were also found using an

approximate supercell-based model of the ideal structure showing that mode e_1 has a symmetric (laterally even) pattern (Fig. 4.3a) and mode e_2 has an anti-symmetric (laterally odd) pattern (Fig. 4.3b).

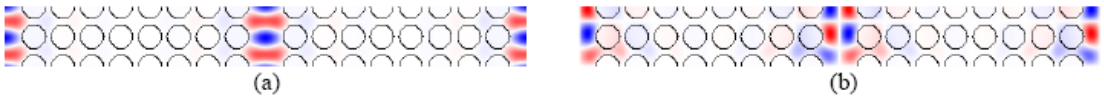

Fig. 4.3. Mode profiles in the PhC waveguide: (a) symmetric even mode, (b) anti-symmetric odd mode.

The fundamental mode e_1 has a bandgap below approximately 1530 nm, also for e_2 at wavelengths below 1520 nm the PhC lattice is no longer confining light in the waveguide region. We experimentally confirm this by coupling the light of different wavelengths to the PhC waveguide and studying near-field optical distributions using our NSOM. As Fig. 4.4 shows, the light is not confined in the center waveguide region at free-space wavelength 1520 nm, the phase fronts are also irregular but somewhat similar to the circular wave emerging from the coupling point. When 1560 nm light is coupled to the structure the light is well confined in the lattice defect and the phase fronts are flat, which shows propagation along the waveguide.

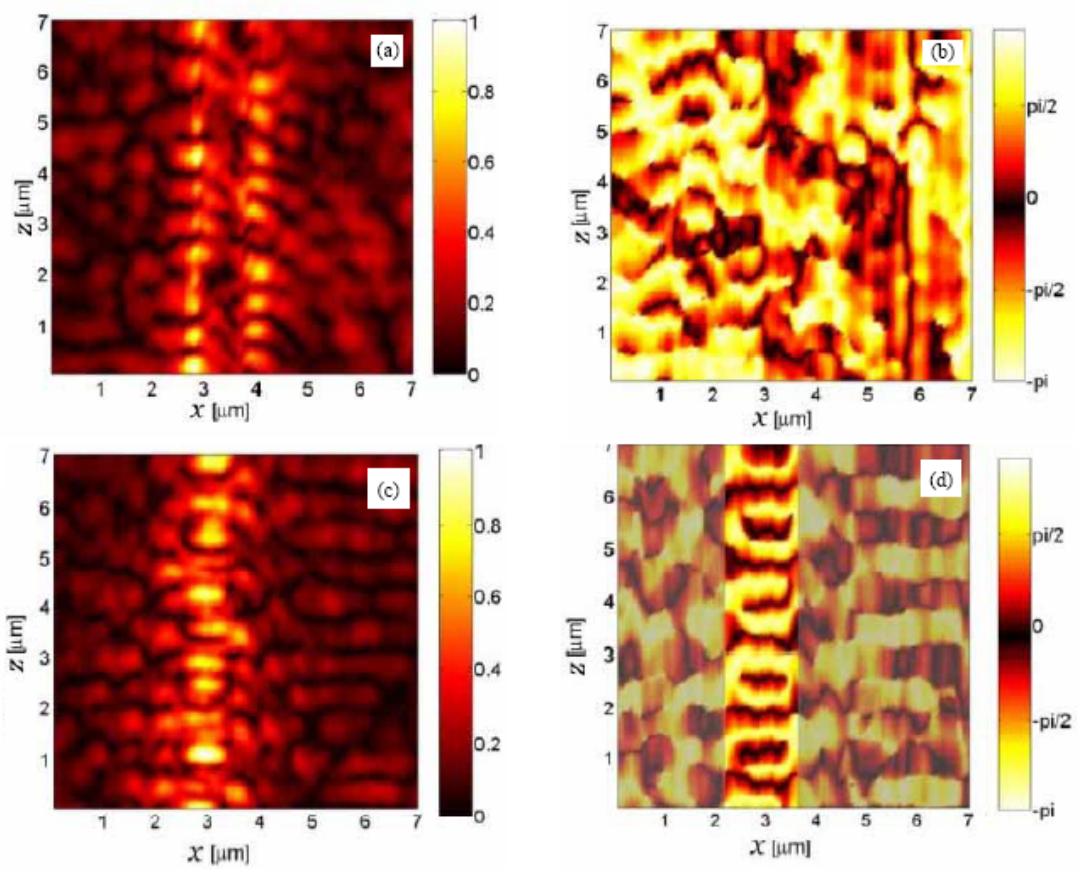

Fig. 4.4. Images of measured amplitude and phase of the optical fields propagating in the W1 PhC waveguide at wavelengths of 1520 nm (a, b) and 1560 nm (c, d), below band edge and in the lattice bandgap region respectively.

Detailed investigation with fine spectral steps has shown that the character of propagation depends on the wavelength of the coupled light (Fig. 4.5). At the 1556.6 nm and 1559.8 nm wavelengths the transverse profiles of the propagating modes appear to be that of the fundamental mode – the amplitude has a single lobe with spatially even transverse symmetry and the phase fronts within the waveguide channel are flat along the transverse direction and uniformly spaced. However, at a wavelength of 1558.2 nm (i.e., halfway between these two values), a very different profile with odd transverse symmetry is observed. For the intermediate wavelengths we see a gradual transition between the

dominant even and odd mode structures. These results reveal a periodic variation of the propagating mode characteristics with respect to the optical frequency. In order to investigate the periodicity of this effect, we extended the measurements spectral region. It was found that the process was repeated almost identically: a new straight pattern was found after 3.1nm at a wavelength of 1553.50nm.

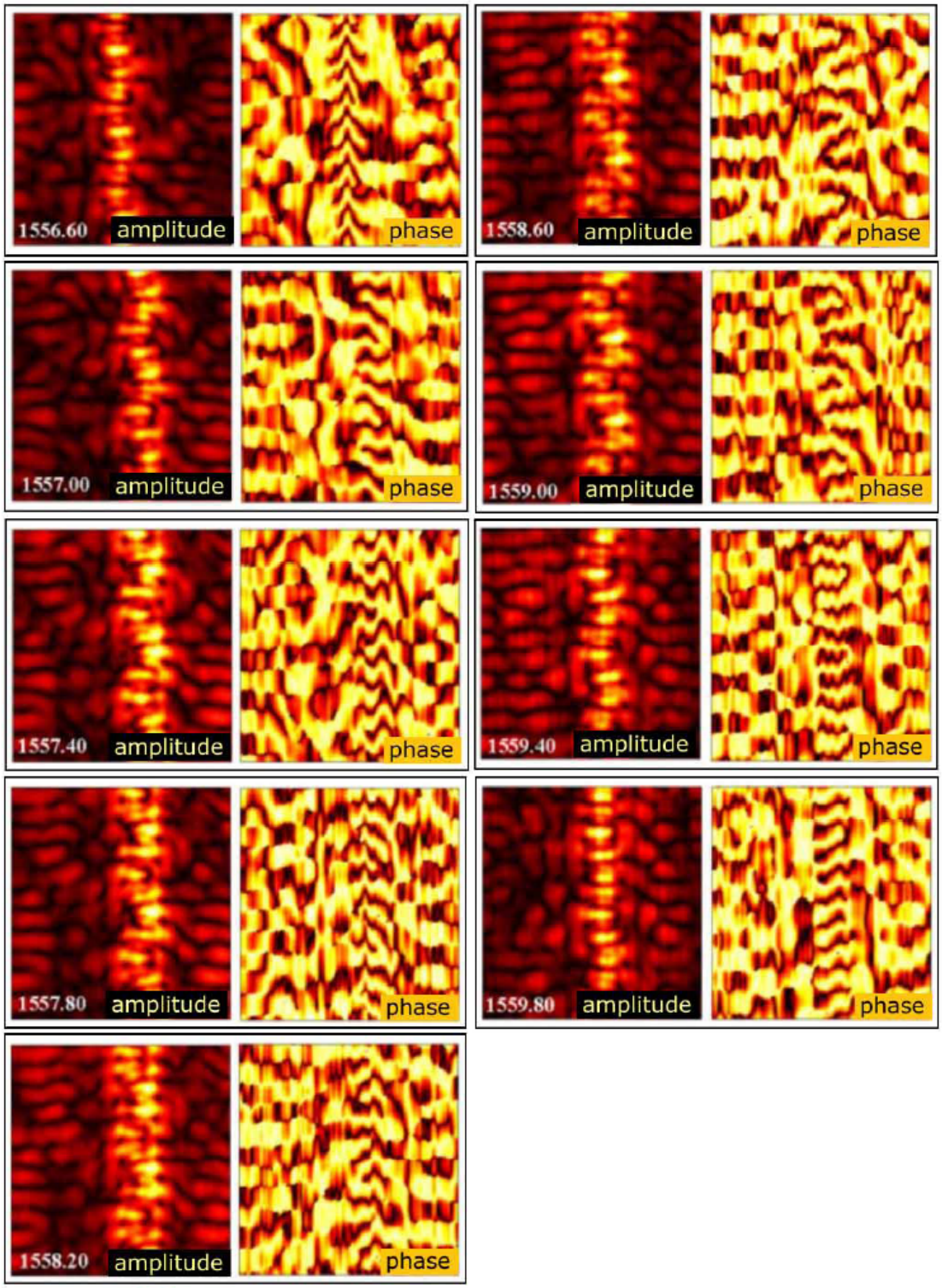

Fig. 4.5. 7 µm x 7 µm amplitude and phase near-field distributions of the light guided in the PhC waveguide for 1556.6 nm – 1559.8 nm free-space wavelengths with step of 0.4 nm. Color map scheme is the same as on the previous figure.

For detailed study of the modal character we perform Fourier analysis of the complex amplitude obtained from our HNSOM investigation. The complex amplitude distribution can be obtained by combining amplitude and phase images according to the equation:

$$C(x,z) = A(x,z) \cdot e^{j \cdot P(x,z)},$$

where A (x, z) and P (x, z) are amplitude and phase distributions respectively; x is the direction across the waveguide and the axis z is in the direction of propagation. Then a one-dimensional (1D) Fourier transform operation is applied to this complex distribution in the z-direction. We leave the x-direction as a spatial coordinate, but the z-direction represents frequency now. Images from Fig. 4.5 a processed in such manner to obtain spatio-spectral distributions. Examples for wavelengths of 1556.6 nm (narrow and even modal distribution) and 1558.2 nm (wide and odd modal distribution) are given on the Fig. 4.6.

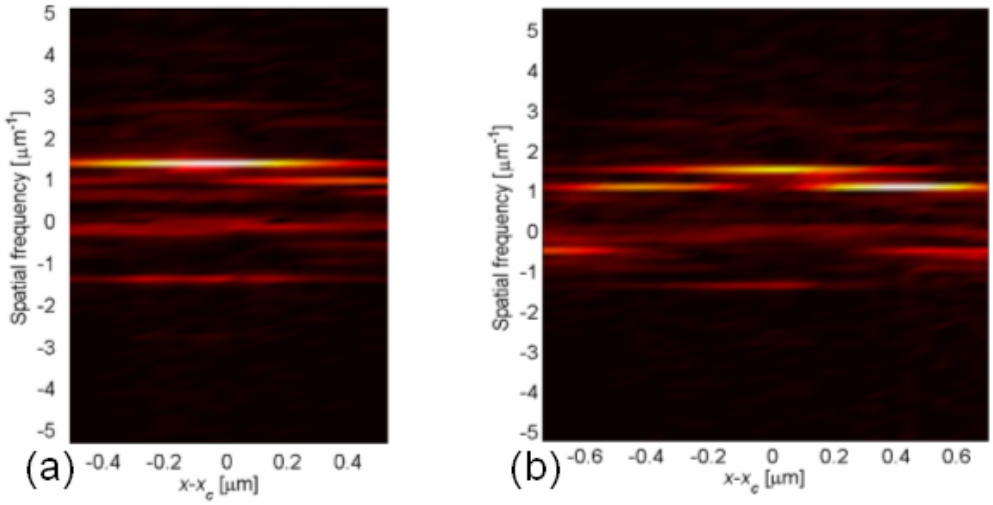

Fig. 4.6. Spatio-spectral content of the light in PhC waveguide at the excitation wavelengths of (a) 1556.6 nm and (b) 1558.2 nm.

Note that Fig. 4.6a has a clear maximum in the center of the waveguide $x = x_c$, which contains most of the power. This mode has a corresponding effective wavelength of $\lambda_{eff,\,e}$= 0.67 μm or the effective refractive index for this mode $n_{eff,\,e}$ = 2.34. There is also a small peak located symmetrically in the negative spatial frequency region, which corresponds to light reflected at the output of the waveguide and propagating in the opposite direction. This illustrates the ability of HNSOM and complex amplitude analysis to be able to resolve direction of the light propagation, since the conventional NSOM is only able to provide intensity mapping. For 1558.2 nm excitation Fig. 4.6b shows on the waveguide boundaries two additional which correspond to another mode (they have the same spatial frequency in the *z*-direction). The first mode in the center of the waveguide has exactly the same parameters as in Fig. 4.6a: effective wavelength of $\lambda_{eff,\,e}$ = 0.67 μm or the effective refractive index for this mode $n_{eff,\,e}$ = 2.3. The second mode which has maxima of amplitude on the sides of the waveguide has the following parameters: effective wavelength of $\lambda_{eff,\,o}$= 0.93 μm or the effective refractive index for this mode $n_{eff,\,o}$ = 1.7.

To analyze the contributions of the different modes in the modal content of the propagating light we integrate distributions on the Fig. 4.6 with respect to the *x* coordinate. This procedure confirms that while in the case of 1556.6 nm excitation the even mode dominates light propagation (Fig. 4.7a), for the 1558.2 nm exciting wavelength the contribution of the odd mode surpasses that of the even mode (Fig. 4.7b).

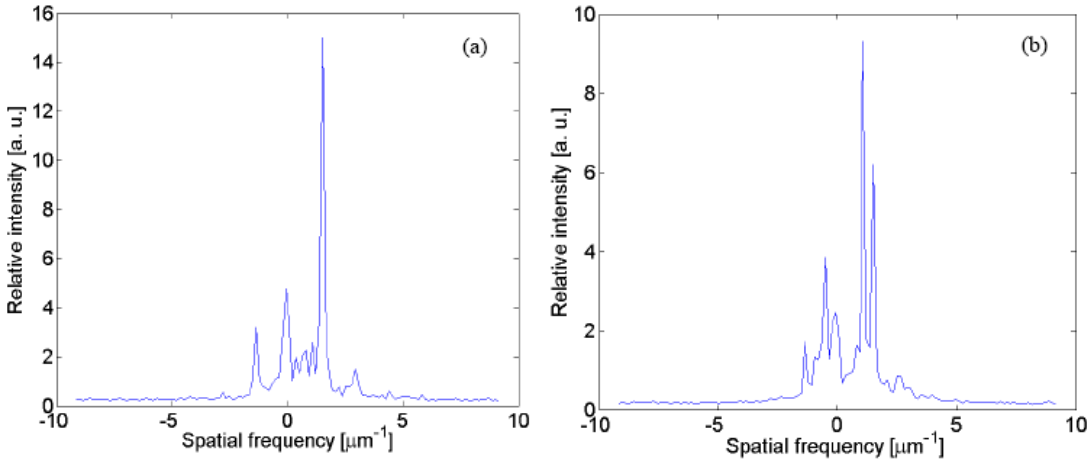

Fig. 4.7. Integral spectral content of the light in PhC waveguide at the excitation wavelengths of (a) 1556.6 nm and (b) 1558.2 nm.

We perform such analysis for all the images from Fig. 4.5 to analyze the evolution of the different modes contributions with respect to change in the excitation wavelengths. This reveals periodic interdependence of the even and odd modes – gradual transition from the single-mode propagation regime to two propagating modes and back with the change in the wavelength of the coupled light (Fig. 4.8).

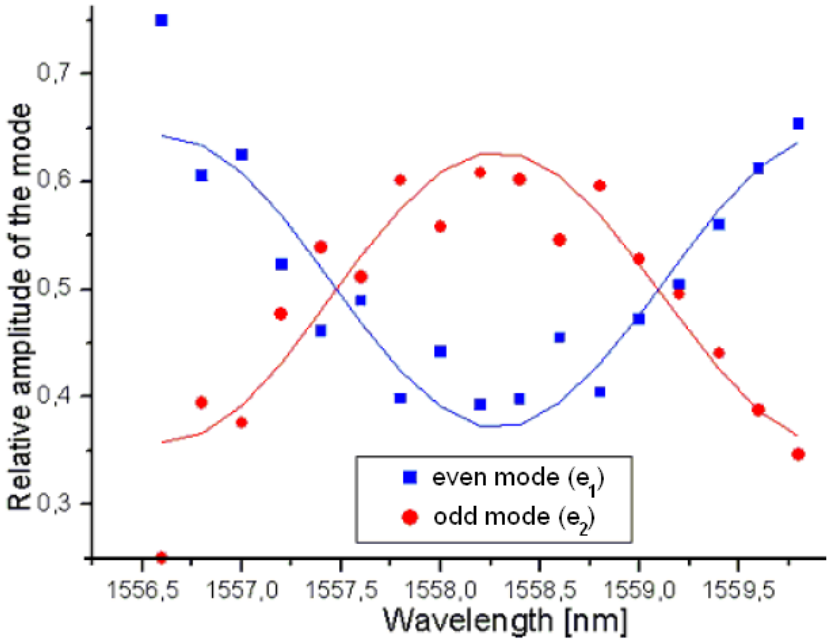

Fig. 4.8. Dependence of the relative amplitudes of the even and odd mode with wavelength of the light coupled to the PhC waveguide.

Numerical simulations using the finite-integral time domain method (CST Microwave Studio 5) performed for the geometry of the device confirm that in case of a single fundamental mode present in the waveguide (Fig. 4.9a) a narrow distribution of a straight mode appears, while for case where both modes e_1 (Fig. 4.9a) and e_2 (Fig. 4.9b) are present the coherent addition of amplitudes (interference) depending on the relative phase delay leads to a "snake-like" mode pattern (Fig. 4.9c).

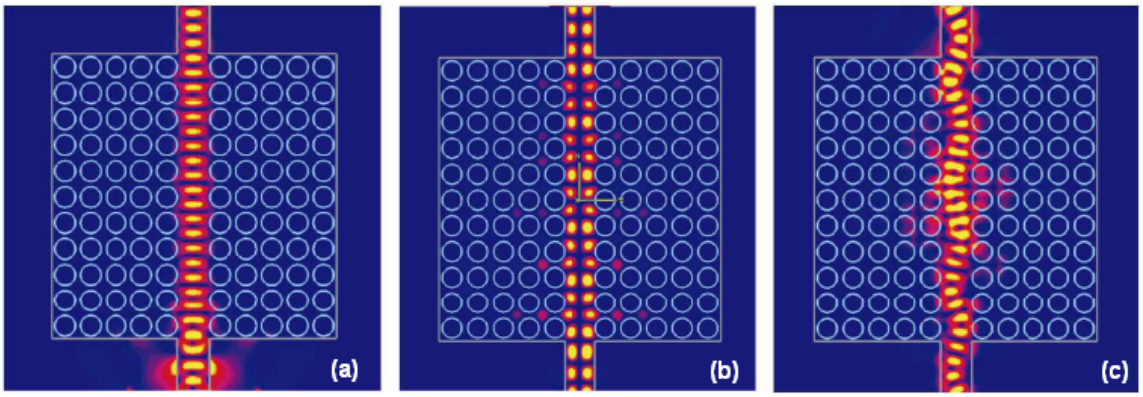

Fig. 4.9. Finite integral time domain simulations showing the propagation of: (a) even mode e_1, (b) odd mode e_2 and (c) interference pattern of superposition of these two modes.

In the studied sample tapered channel waveguides were used for optimizing the coupling from the optical fiber with attached graded index lens to the PhC waveguide. The channel waveguide had a rectangular cross section with the height of 290 nm and the initial width of 10 µm was gradually tapered to 1 µm towards the junction with the PhC membrane. This provides an opportunity to show how the NSOM technique can be used for measuring coupling losses caused by mode mismatch between different components of the photonic circuit.

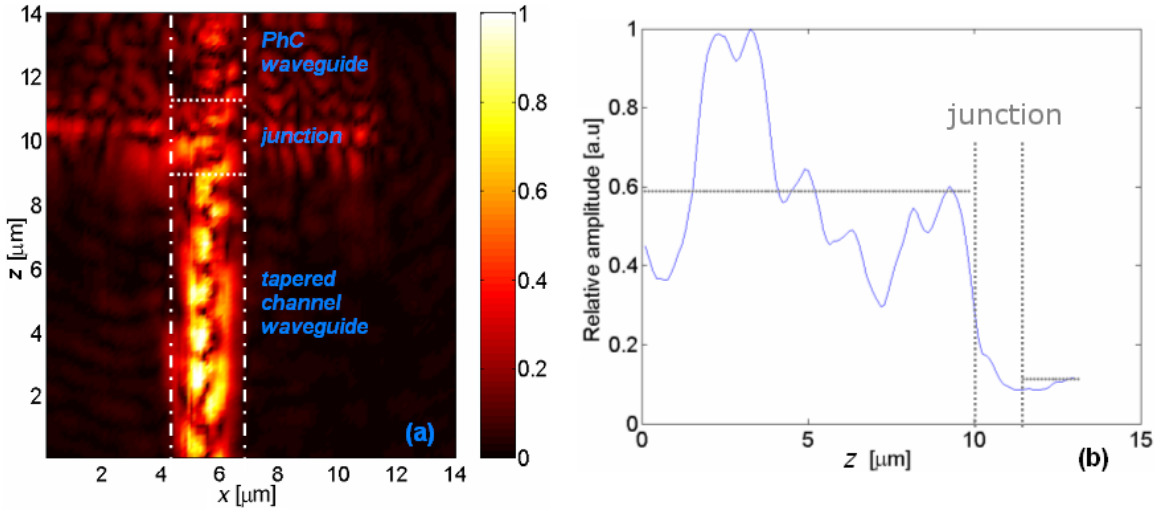

Fig. 4.10. Loss measurements at the junction between channel waveguide and PhC waveguide: (a) HNSOM amplitude image with the shown boxed integration areas; (b) total amplitude vs. propagation distance showing a drop due to the junction loss.

The near-field approach provides exact information about the losses independent of the initial coupling conditions as it provides local measurements of the amplitudes in the two components of interest. The HNSOM amplitude image (Fig. 4.10a) shows the clear drop in the amplitude in the PhC waveguide compared to the amplitude in the tapered channel waveguide. To provide quantitative data we integrated amplitudes across the propagation direction in the boxed areas and plotted the dependence of the amplitude on the propagation distance (Fig. 4.10b); this plot shows that for the coupled wavelength of 1553.5 nm intensity loss of 7.1 dB occurs in the junction. Similar measurements were performed for other wavelengths and it was found that loss ranges from 2.7 dB at wavelength of 1554.5 nm to 7.1 dB at 1553.5 nm; moreover the spectral dependence of the junction loss demonstrates the same ~3 nm periodicity as the modal pattern (Fig. 4.8).

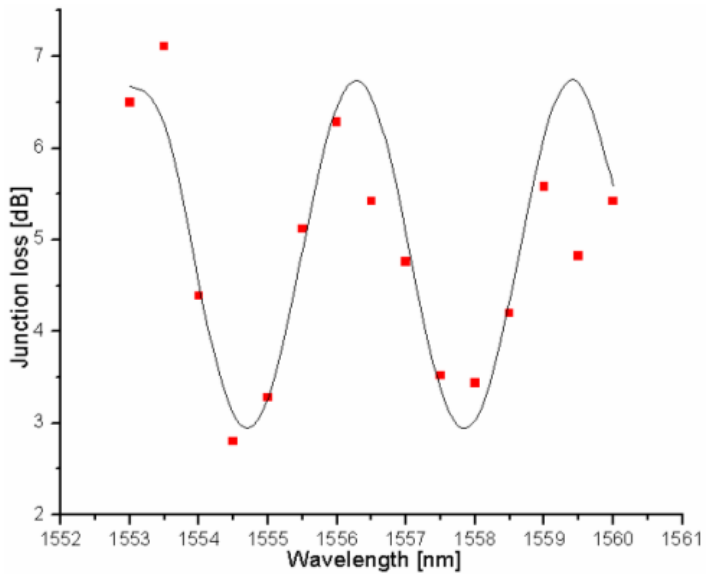

Fig. 4.11. Loss at the junction between the tapered channel waveguide and PhC defect waveguide for different wavelengths.

It was also found that the maximal loss is observed when the odd mode is not excited in the PhC waveguide (λ = 1558 nm minimum on the loss graph approximately corresponds to the maximum of the odd mode contribution on the Fig. 4.8). In this case assuming there is no strong coupling between the two modes inside the PhC waveguide, since one mode is universally present and the second mode varies in amplitude, it is reasonable to expect that we should see the greatest transmission of energy through the waveguide when the both modes are present. This is probably a sign that if the conditions do not allow odd mode propagation all of its intensity is lost in the PhC junction. Although there is insufficient information to draw a firm conclusion, these results reveal an agreement between near-field measurements made on differing areas of the PhC waveguide. Further analysis is needed to confirm this theory, but the results found also show that special care should be taken in the design at the junctions of the different components in the photonic circuit. Our measurements reveal that the loss due to mode

mismatch can be significant even in the case where the geometrical sizes of the waveguides are quite close.

4.3. Demonstration of the self-collimation in PhC

With a more sophisticated PhC lattice engineering it is possible to create even more interesting devices and components. A lot of research has been dedicated to tailoring the dispersion characteristics of PhC to achieve special optical properties [42, 43].

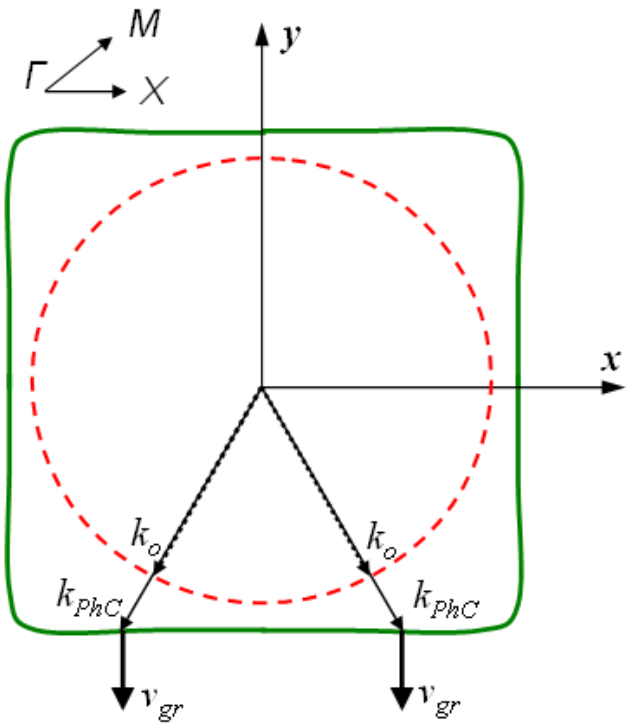

Fig. 4.12. Typical equi-frequency dispersion surfaces of the wave propagating in the uniform slab (red dashed) and in the planar photonic crystal lattice (green solid).

Dispersion surfaces for the PhC structures can be obtained by solving Maxwell's equations, for example by numerical methods such as plane-wave expansion. For a

specific frequency the dispersion surface will give a cross section which is called the equifrequency contour (EFC) [44]. For a square-shaped EFC (Fig. 4.12), which can be designed by choosing parameters of the square PhC lattice [45], we can obtain a regime of self-collimation. This phenomenon characterizes propagation of an optical beam in a uniform or periodic medium for which diffraction does not result in broadening of the beam. It can be shown that the group velocity and the direction of energy flow are determined by the gradient of frequency as a function of $\boldsymbol{k}$ and coincide with the normal to the EFC at the point of intersection of the EFC with the direction of the wave vector. Thus for a square-shaped EFC the $\boldsymbol{k}$-vectors not parallel to the direction of beam propagation, occurring due to diffraction, do not lead to the energy flow to the sides – the beam diameter remains constant as it propagates inside such a lattice.

To experimentally demonstrate the self-collimation phenomenon a 10-µm-wide and 45-µm-long PhC structure with lattice constant of 350 nm was fabricated (Fig. 4.13a). Near-infrared light λ = 1560 nm with TE-polarization was delivered to the lattice section of the sample via a silicon channel 2-µm-wide waveguide. The diffraction in the PhC structure was compared to that inside the unpatterned uniform slab. Near-field investigation performed with our HNSOM has shown significant differences between these two cases: while for the unpatterned slab as light propagates from the channel waveguide its width changes from 2 µm to approximately 16 µm due to diffraction (Fig. 4.13b), for PhC lattice propagation the diffraction has almost no effect on the beam width which changes to only approximately 2.25 µm at the end of the membrane (Fig. 4.13c).

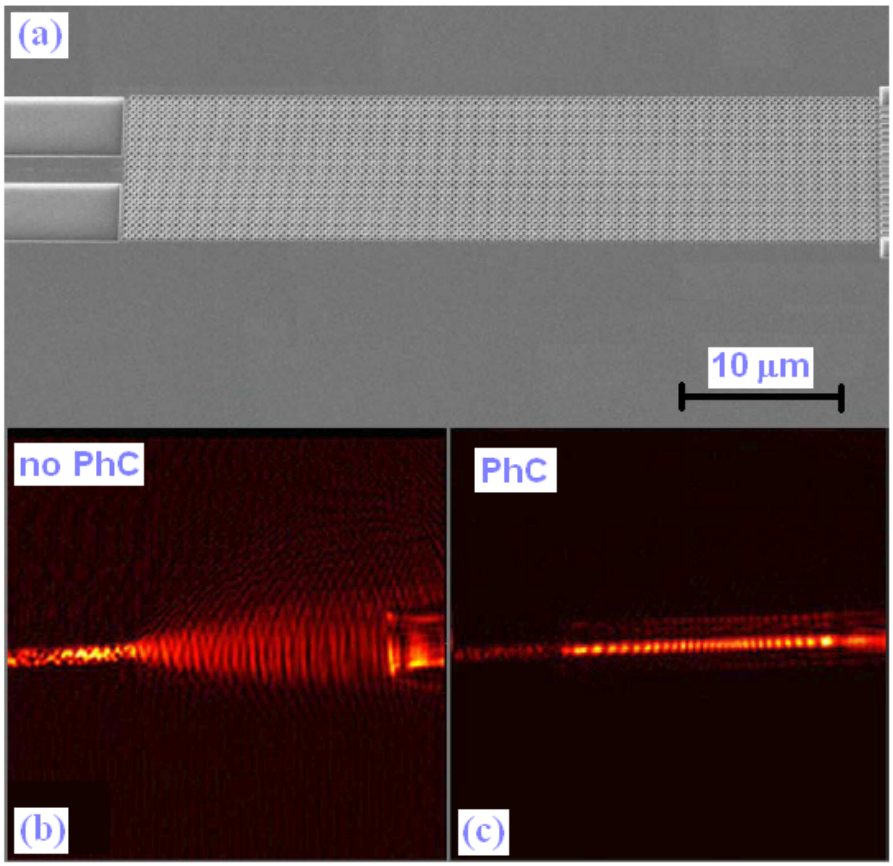

Fig. 4.13. Near-field investigation of self-collimation phenomena in PhC lattice: (a) SEM micrograph of the PhC structure with channel waveguide delivering light on the left; (b) 70 µm x 70 µm near-field amplitude image showing diffractive propagation in the unpatterned silicon slab; (c) 70 µm x 70 µm near-field amplitude image showing self-collimation in the PhC.

Some widening of the beam in our experiments with PhC structure occurs probably due to fabrication errors with respect to the designed parameters since numerically obtained optical phase distribution shows flat phase fronts (Fig. 4.14a). Experimentally measured using our HNSOM, phase distributions (Fig. 4.14b) show some signs of the beam widening and enable calculation of effective index of the TE-polarized light in our PhC structure $n_{eff} = 2.23$.

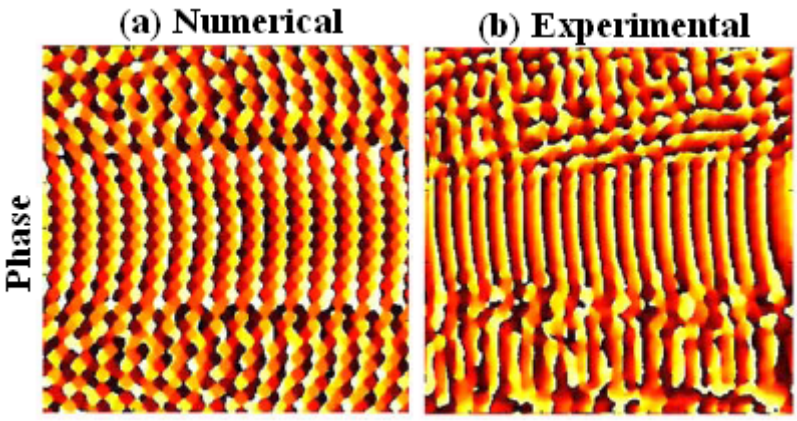

Fig. 4.14. Numerical (a) and experimentally obtained near-field (b) phase distributions characterizing self-collimation propagation regime in the PhC lattice**.**

The demonstrated phenomenon of self-collimation can be used for low-loss waveguides [46] in which the mode size is not determined by the geometrical parameters but rather by mode size of the input light. Other possible applications include beam splitting and switching [47] and light modulation [48]. This phenomenon can also be extended to self-collimation in 3D PhC structures [49].

4.4. Polarization beam splitter based on the PhC approach

It was proposed recently to use PhC for separating different polarizations in planar photonic devices [50]. In this approach a uniform PhC structure is used in combination with the channel waveguide delivering light to the lattice at the particular angle (45°). This angle ensures that one of the polarizations (TM) is reflected since it falls in the bandgap region, while the other (TE) is transmitted virtually without any losses (TE-polarized mode propagation is not forbidden in the PhC, also incidence angle is close to the Brewster angle in this case). This result shows that photonic crystals enable table-top functionality, such as a Glan-Thompson polarization beam splitting (PBS) cube, to be

transferred to planar on-chip devices enabling separate processing (dispersion compensation, etc.) for different polarization modes. Additional advantage can be gained by using enhanced engineering capabilities for PhC lattices, for example the self-collimation described above.

Another method that can be used to realize PBS functionality is the PhC heterostructure. This method was demonstrated to work for a SOI material system [51]. In this approach there are two PhC lattices with different geometrical parameters adjoined together (Fig. 4.15).

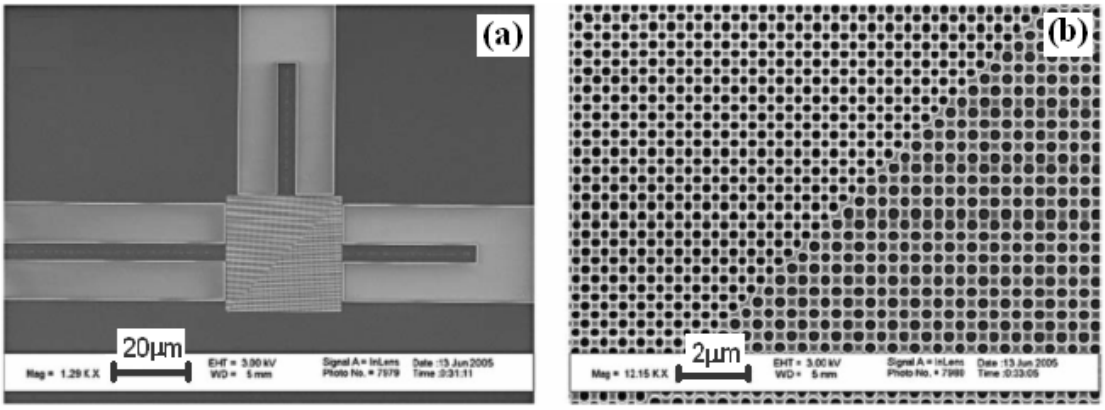

Fig. 4.15. SEM micrographs of the device (a) and higher magnification of the boundary between two PhC lattice boundary (b).

The lattices are engineered in such a way that TE-like mode is close to a directional gap at the top of the band and has very high reflection at the boundary between the two PhCs. At the same time the mode with TM polarization is in a low frequency regime and has high transmission through the boundary.

To demonstrate the PBS functionality a PhC device splitting two polarization modes coming from the channel silicon waveguide with width of 5 µm was designed. At

the outputs similar 5-µm-wide channel waveguides were placed to couple out obtained TE and TM modes. We performed HNSOM investigation (Fig. 4.16) of this device and confirmed the polarization resolving capability. For the incoming TE-polarized mode the light was mostly reflected at the boundary (Fig. 4.16c) and propagated towards the upper output waveguide. Some of the light was still propagating into the second PhC lattice and coupled to the output TM-waveguide (Fig. 4.16a), which occurred probably due to the parasitic TM polarization in the input waveguide arising due to non-ideal extinction at the input fiber coupling system to the sample or some polarization mixing in the input channel waveguide. Polarization resolving NSOM capabilities or modal analysis of the light in the input waveguide could be used to confirm this assumption. On the positive side the first PhC lattice seems to possess the property of self-collimation to the TE-polarized mode, thus the efficiency of the coupling to the output waveguide is relatively high – the beam size is almost intact as it propagates through the PhC structure.

The TM-polarized mode has almost no reflection at the PhC lattice transition boundary thus it is transmitted right through towards the TM-output waveguide. For this polarization however the diffraction is quite significant and thus a considerable amount of light is lost at the output PhC-channel waveguide coupling point. Similar polarization splitting devices based on the PhC heterostructures which provide self-collimation for both TE and TM polarization modes were proposed recently [52, 53].

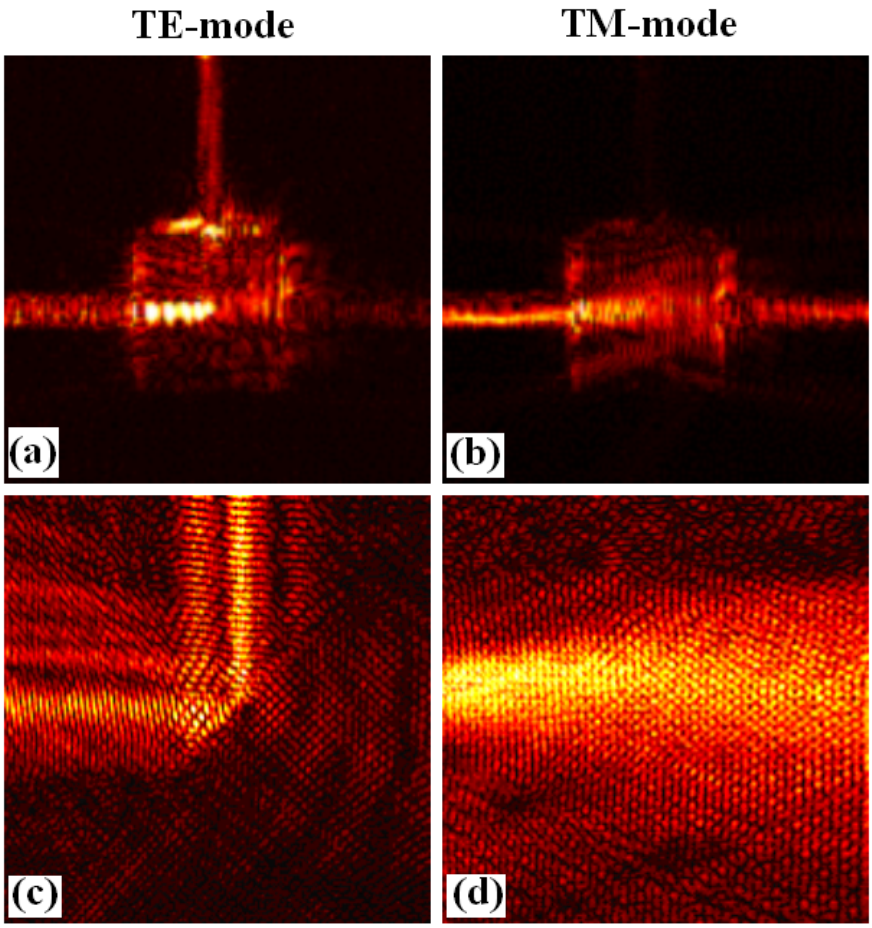

Fig. 4.16.(a) and (b) near-field amplitude 70 µm x 70 µm distributions on the surface of PhC PBS device for TE and TM modes respectively; (c) and (d) high resolution images showing beam propagation around PhC lattices transition boundary.

5. Dielectric metamaterials for the on-chip photonic devices

5.1. Dielectric metamaterials concept

Materials having refractive index varying with characteristic distances much smaller than the wavelength of light cannot behave as photonic crystals, but nevertheless they can also have very unusual and interesting properties. We will call such structures "metamaterials" (from the Greek word "μετά" = "after", "beyond") – materials that gain their properties from their structure rather than only from their constituents. This approach can be illustrated by form-birefringent materials – one-dimensional periodic structures which have polarization-dependent index of refraction [54, 55] and unusual nonlinear properties [56]. Extending this concept to 2D geometry or implementing aperiodicity enables other useful functionalities such as converting a linear polarization state to radial or azimuthal polarization [57] and creating a graded-index medium [58]. It was also shown that the metamaterial approach can help to overcome fabrication difficulties and create a Fresnel lens analogue using a binary lithographic approach with feature size of less than 60 nm [59].

Bringing the functionality of table-top optical information processing components to a chip will create compact devices, which can benefit from fast data transfer, small form-factor, parallel processing, and low power consumption. Implementing free-space-

like propagation for planar optics means that while the light is confined by index difference in the chip plane, the beam size is regulated by phenomena similar to those in 3D free-space optics such as diffraction and refraction. This will allow a direct and more natural transition from conventional bulk optics devices to photonic integrated circuits.

To create a dielectric planar metamaterial a subwavelength structure can be fabricated in a high refractive index slab (Fig. 5.1).

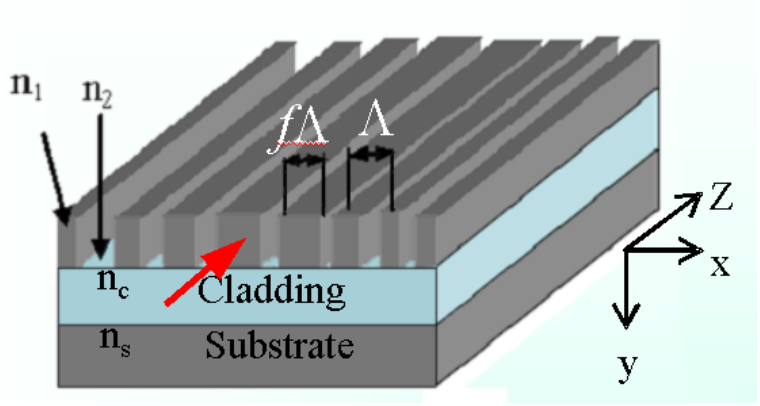

Fig. 5.1. Schematics of the subwavelength grating planar metamaterial.

The slab has index of refraction of n_1, we assume that the gaps in the etched subwavelength structure are filled with air so $n_2 = 1$. This slab is sitting on a cladding with lower index of refraction $n_c < n_1$, to ensure confinement in the vertical direction. For some material systems, for example for silicon-on-insulator technology, the cladding with the guiding slab is sitting on top of the thicker substrate n_s, which provides durability. The period of the grating is Λ. $f\Lambda$ is the fraction of the unit cell filled with high-index material. From second-order effective medium theory [60]:

$$n_{TE}^{(2)} = \sqrt{\left(n_{TE}^{(0)}\right)^2 + \frac{1}{3}\left[\frac{\Lambda}{\lambda}\pi f\left(1-f\right)\left(n_1^2 - n_2^2\right)\right]^2} \qquad \text{(Eq. 5.1a)}$$

and

$$n_{TM}^{(2)} = \sqrt{\left(n_{TM}^{(0)}\right)^2 + \frac{1}{3}\left[\frac{\Lambda}{\lambda}\pi f\left(1-f\right)\left(\frac{1}{n_1^2}-\frac{1}{n_2^2}\right)n_{TE}^{(0)}\left\{n_{TM}^{(0)}\right\}^3\right]^2} \qquad \text{(Eq. 5.1b)},$$

where

$$n_{TE}^{(0)} = \sqrt{fn_1^2 + \left(1-f\right)n_2^2} \qquad \text{(Eq. 5.1c)}$$

and

$$n_{TM}^{(0)} = \frac{n_1 n_2}{\sqrt{fn_2^2 + \left(1-f\right)n_1^2}} \qquad \text{(Eq. 5.1d)}$$

are the initial index approximations for TE (E-field vector is in vertical direction) and TM (H-field vector is in vertical direction) polarizations respectively. This set of equations (Eq. 5.1) was shown to be realistically accurate for small grating periods $\Lambda < \lambda/n$ [61] and for grating thickness larger than $\lambda/3$ [62]. Other approaches in design and analysis of these subwavelength grating metamaterial structures include numerical methods such as rigorous coupled-wave analysis, finite element method, and the finite-difference time-domain (FDTD) approach.

This concept can be used, for example, in creating new materials with refractive indices different from that of the constituents. For example for a silicon-on-insulator material system we usually have silicon with index of refraction of $n_{Si} = 3.48$ and silicon dioxide with $n_{SiO2} = 1.46$ as the only materials available for structure design. In table-top free-space optics, on the other hand, we have a variety of materials such as different glasses, crystals, polymers. This fact makes it difficult to directly transfer table-top optical setups to on-chip implementations. To overcome this difficulty metamaterials can

provide an elegant solution. For example by implementing the scheme of subwavelength gratings the index achievable for an SOI material system varies from 1.5 to 3.4, thus covering almost fully the range between high-index silicon and low-index oxide. This range was calculated for a period of Λ = 400 nm (to fulfill subwavelength condition of $\Lambda < \lambda / n = 1500\,\text{nm}/3.5 \approx 400\,\text{nm}$) and for filling factors from 0.1 to 0.9 to ensure fabrication capabilities (feature size > 40 nm). Polarization of the optical field was taken as TE.

5.2. Graded index structures

If we have a variable filling factor in such a subwavelength structure we will naturally obtain graded index metamaterial media. It is well known that light bends towards higher index of refraction in such materials, and thus we can check performance of the obtained structure by studying light propagation. Numerical simulations for the light propagation in the SOI structure with subwavelength grating structure having a variable filling factor and periods of Λ = 150 nm and Λ = 300 nm show the bending of light towards the higher filling factor areas (Fig. 5.2).

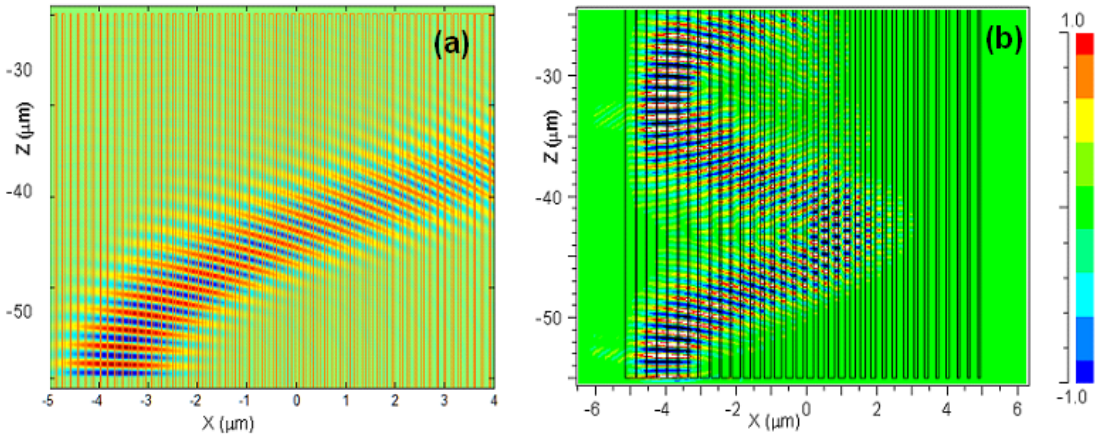

Fig. 5.2. Numerical modeling results showing light propagation in subwavelength SOI gratings with variable filling factor (increasing from left to right) and periods of (a) Λ = 150 nm and (b) Λ = 300 nm.

The propagation of light for the structure modeled with long wavelength limit (Fig. 5.2a) shows truly graded index behavior, while for larger period (Fig. 5.2b) we can observe some reflection. This Bragg reflection resonance occurs due to the fact that as light propagates close to normal to the gradient of index its effective wavelength becomes smaller (as the index increases) until the Bragg condition is satisfied $\lambda_{eff} = \lambda / n = 2\Lambda \sin\theta$ (for the first diffraction order). After the reflection light propagation is again governed by the metamaterial graded index property, so we have a situation of periodically repeating bending and reflection. This type of light propagation ("snake" propagation), occurring due to a combination of non-resonant and resonant behavior, is quite unusual and cannot be observed in natural materials.

To experimentally demonstrate this possibility we fabricated a silicon subwavelength structure with period Λ = 500 nm and variable filling factor (Fig. 5.3).

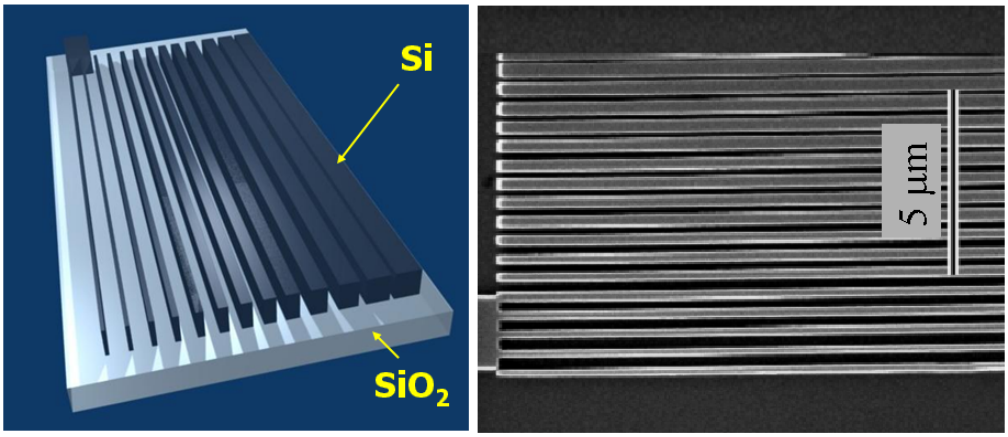

Fig. 5.3. (a) Schematic picture and (b) SEM micrograph of the fabricated graded index dielectric metamaterial.

Light was delivered to the structure via a 2-μm-wide silicon channel waveguide with narrow section and bend prior the grating to filter out higher modes and free-space propagating light. The propagation of light in the graded index medium was studied using our HNSOM. Amplitude distribution ove the larger area shows "snake" propagation of light in the structure (Fig. 5.4a), while smaller area scans clearly demonstrate (Fig. 5.4 b, c) light bending towards the higher refractive index as well as decreasing in wavelength, which results in smaller spacing between phase fronts, as a result of such propagation. The spacing between the phase fronts at the input to the device (lower left corner of Fig. 5.4c) corresponds to the wavelength of approximately 1.4 μm and at the higher effective index medium (right side of Fig. 5.4c) λ_{eff} = 1 μm.

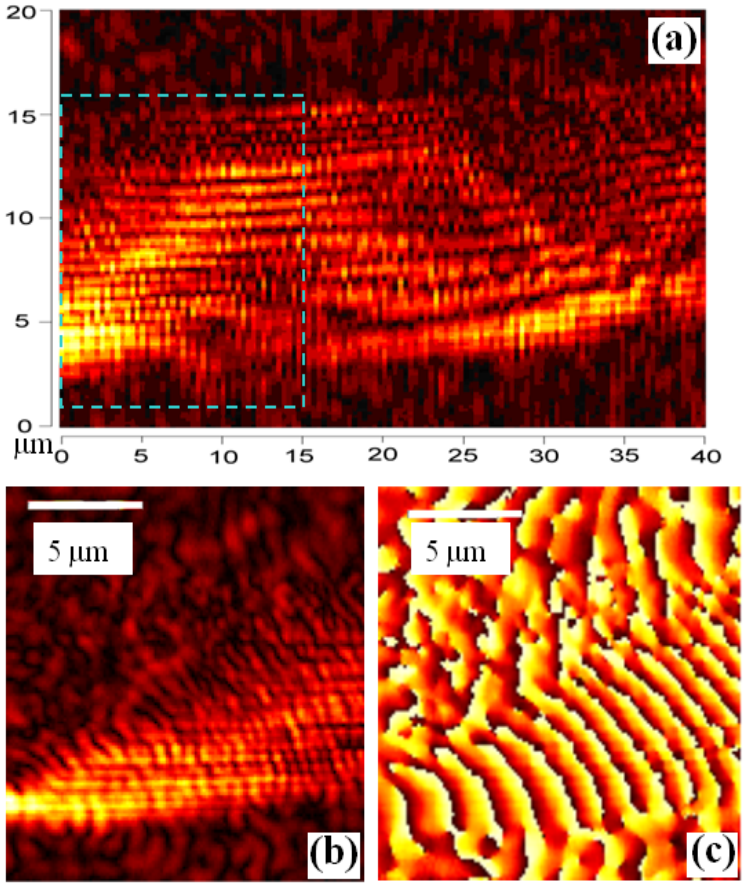

Fig. 5.4. HNSOM measurements of the light propagating in the graded index metamaterial: (a) amplitude distribution shown propagation consisting of periodic reflections with bending towards refractive index gradient; (b) and (c) near-field amplitude and phase distributions of the boxed area showing light bending and decreasing effective wavelength.

The presented experimental results prove the concept of dielectric metamaterial realization as a subwavelength grating to work well in creating graded index media. Similar devices can be used for spectral demultiplexing (WDM coupler), in which two signals with different carrier wavelengths can be spatially separated after several periods of “snake” mode based on the spectral dependence of the Bragg reflection phenomena.

5.3. Quadratic effective index profile and applications

For focusing and waveguiding quadratic phase should be added to a propagating beam. In the table top optics approach lenses are used to achieve this functionality, whereas for on-chip planar optics it is possible to use a dielectric metamaterial approach for this purpose. In the design of such a material equations Eq. (5.1 a, c) can be used to provide a quadratic profile of the refractive index by varying the filling factor of a subwavelength grating (TE-polarization assumed). The quadratic index dependence can be specified as:

$$n(x) = n_0\left(1-\frac{1}{2}\alpha x^2\right)$$

with the desired parameters of $n_0 = 3.2$ and $\alpha = 0.01$ in the SOI material system without SiO_2 overcoating (air in the grating gaps), which gives $n_1 = 3.5$ and $n_2 = 1$; chosen wavelength $\lambda = 1550$ nm and grating period $\Lambda = 400$ nm. For these values dependence of the filling factor on the linear coordinate across the direction of propagation, lens geometry, can be calculated (Fig. 5.5).

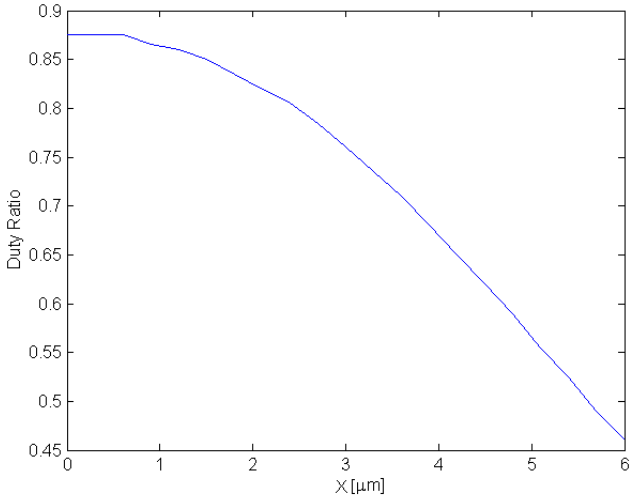

Fig. 5.5. Calculated theoretical dependence of the filling factor on the spatial coordinate across the light propagation direction to achieve quadratic index profile.

Light propagation in this or similar structures can be calculated by various numerical methods. Specifically it is possible to implement the FDTD approach provided by the Rsoft's FullWAVE software package [58]. Results of this analysis show that the similar structure designed for grating period Λ = 400 nm and filling factors ranging from 0.25 to 0.75 to ensure fabrication capabilities for the smallest feature size of 100 nm indeed provides focusing capabilities (Fig. 5.6). The device length was 10 μm and the focal distance obtained in the simulations turned out to be around 8 μm.

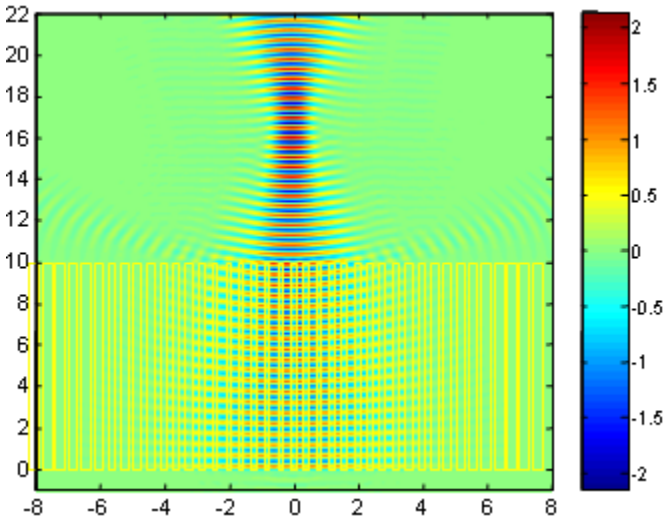

Fig. 5.6. Result of the FDTD modeling of light propagating in the slab with the embedded subwavelength grating with parameters providing quadratic refractive index.

This focusing capability can be used for integration of nanophotonic components into on-chip photonic circuits. In bulk optics lenses are usually used for adjusting beam waist size, and for on-chip devices adiabatic tapers usually serve this purpose. Planar lenses made of subwavelength grating dielectric metamaterial can provide a more natural approach for matching mode sizes in planar integrated photonics. Additional advantages of this approach are more flexible engineering capabilities and the smaller footprint of such mode matching components. Numerical modeling shows (Fig. 5.7) that the planar lens made with dielectric metamaterial can provide mode matching between a 5-μm-wide channel waveguide and a 1-μm-wide waveguide with efficiency of better than 90% and the device length in this case is smaller than 10 μm. Adiabatic tapers need to be significantly longer to provide similar efficiency under these conditions.

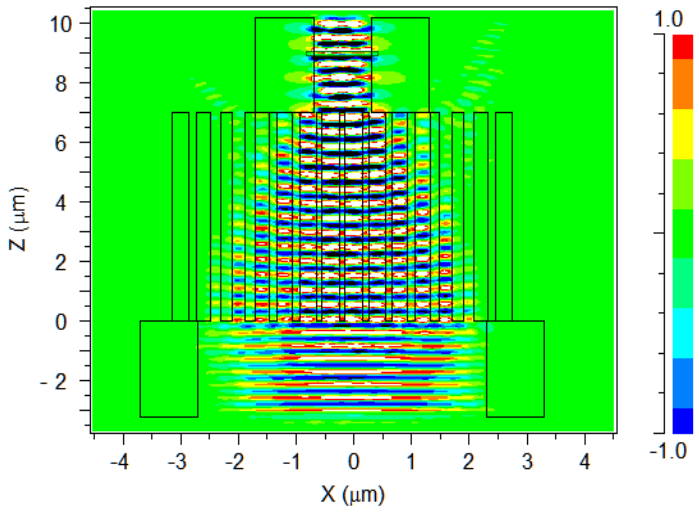

Fig. 5.7. Numerical modeling of mode matching capability of the planar lens designed using subwavelength grating metamaterial approach.

5.4. Experimental investigation of the planar metamaterial lens

To demonstrate this concept we designed and fabricated a specific device based on the SOI material system. A silicon slab with a height of 250 nm sitting on top of an SiO_2 oxide layer is providing light confinement in the vertical direction. The proposed device would match the modes between two similar 2-µm-wide silicon channel waveguides located 15 µm apart and divided by the silicon slab. Diffraction caused by the lack of confinement in the horizontal direction broadens the beam emerging from the first waveguide on the left, thus only a small fraction of light couples to the second waveguide at the right side of the picture (Fig. 5.8a).The coupling efficiency can be estimated in this case as only approximately 20%. We place a 20-µm-long planar lens, which efficiently matches the free-space (in the horizontal direction) propagating mode, after 5 µm propagation in the unpatterned slab to the 2-µm-wide silicon channel

waveguide mode towards its right side. Here again we chose the period of the grating structure as $\Lambda = 400$ nm and the largest filling factor $f_{max} = 0.75$ to ensure that the smallest feature size is not exceeding the 100 nm resolution limit. The smallest filling factor cannot exceed $f_{min} = 0.35$ to provide confinement of the mode in vertical direction. The result of numerical FDTD simulation (Fig. 5.8b) shows that in this case the efficiency of coupling light between the waveguides is approximately 95%.

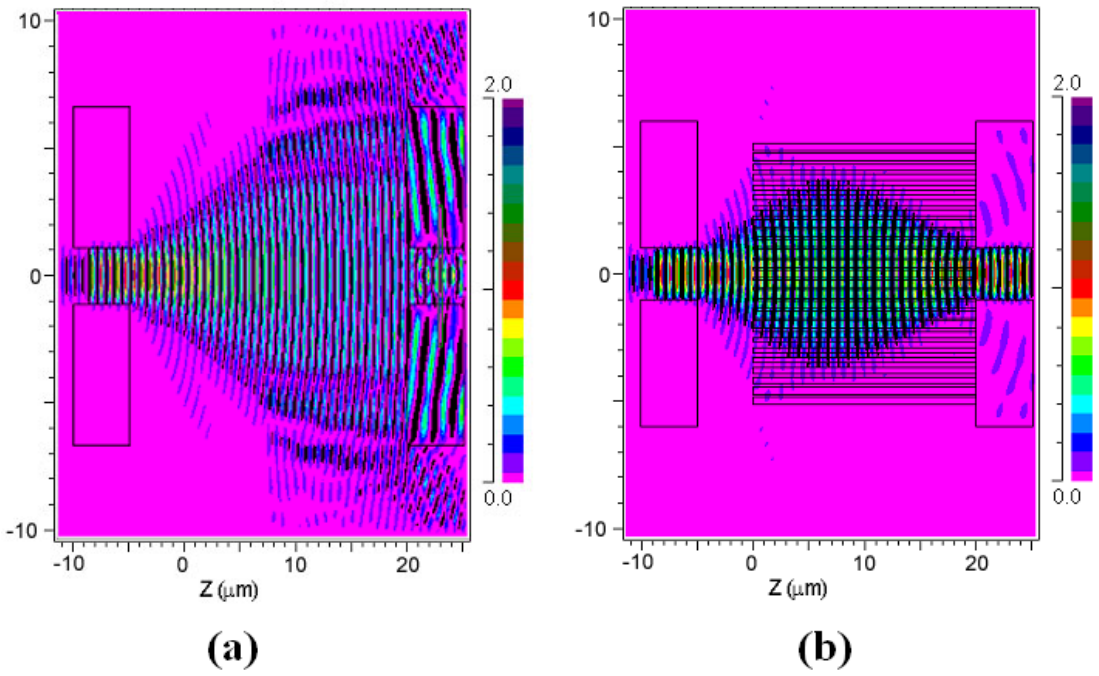

Fig. 5.8. Results of FDTD modeling showing (a) inefficient coupling between the waveguides due to the diffraction in the silicon slab and (b) efficient coupling due to the subwavelength dielectric grating action as a planar lens cancelling diffraction and focusing the light towards the input on the second waveguide.

This approach where the light is allowed to propagate in non-confining slab regions can be called free space optics on a chip – the closest to the functionality of the table-top bulk optics setups.

The designed device was fabricated in our lab by patterning the device using e-beam lithography with the converted SEM. The pattern was then transferred to a metal mask using liftoff and etched into the silicon slab using Chlorine based chemistry and reactive ion etching technique. Fabrication results were validated using SEM imaging (Fig. 5.9).

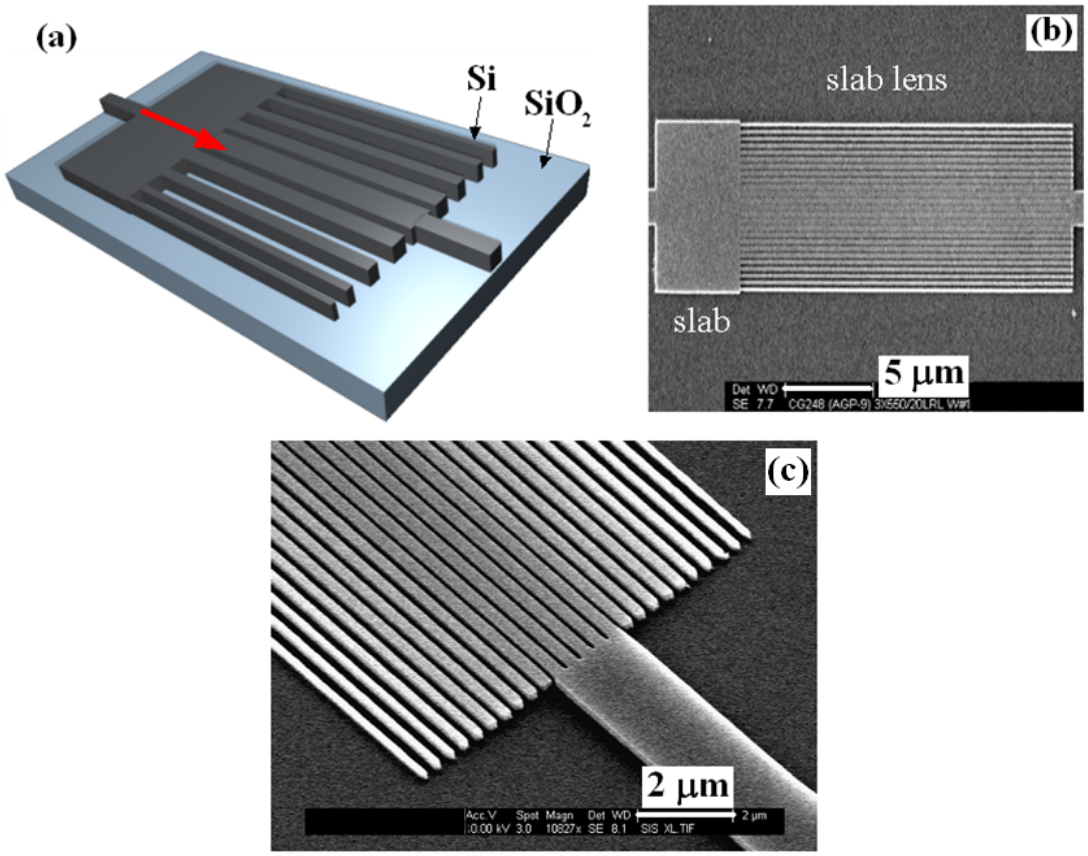

Fig. 5.9. (a) Schematics of the SOI subwavelength structured slab lens; (b) SEM micrograph showing fabricated device; (c) zoomed image of the SEM micrograph taken under an angle to show the grating features resolved in fabrication.

Optical properties of this planar lens were studied using the HNSOM technique. Images in this section were taken using NSOM probes with aperture of 100 nm. The large-scan-area image (Fig. 5.10) describes the propagation of light in the structure: first

light propagating in the 2-μm-wide silicon channel waveguide is coupled into the unpatterned slab region and it starts to broaden due to diffraction, then as the light enters the subwavelength grating it is still increasing its width, but then at some distance it focuses to a narrow waist. In contradiction to the predicted behavior the focusing point is not at the end of the lens (Fig. 5.8b) but rather in the middle of the lens. This is a consistent result for several samples and we will return to this issue later. After passing the focus the light naturally starts to increase its beam size and then it is partially coupling to the output waveguide. The coupling efficiency estimated by integration of the values over equal sections of the input and output waveguides gives coupling efficiency only 60%. Such a discrepancy with the numerically obtained efficiency of 95% can be explained by the wrong positioning of the focal spot.

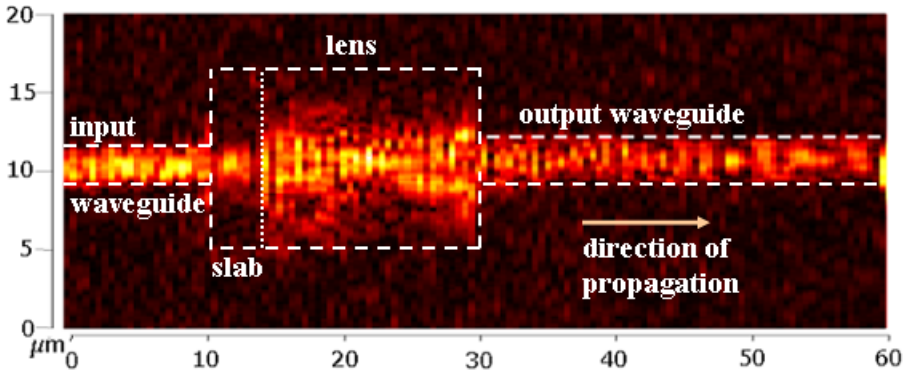

Fig. 5.10. Near-field amplitude distribution showing light propagation in the device. Geometry of the device is sketched with the dashed line.

To further illustrate the focusing effect we took high-resolution images with zoom in the lens area. It is clearly visible that nanostructured lens (L-section on Fig. 5.11a) cancels the diffraction of the light occurring in the unpatterned slab (S-section on Fig.

5.11a) and that the focusing spot lies approximately in 10 μm from the beginning of the grating structure. The phase distribution (Fig. 5.11b) further demonstrates the focusing ability through the evolution of phase fronts in the device. The phase fronts in the waveguide section are straight (1) and perpendicular to the direction of propagation; then as an effect of the diffraction in the non-patterned slab part the convex phase fronts (2) show the widening of the beam; as the light enters the lens region the convex phase fronts gradually flatten out to become straight again (3) and then the focusing starts to narrow the beam size which results in the concave fronts (4); at the focal point the phase is flat once again (5) and then past the focus we have the convex phase fronts (6) and widening of the beam.

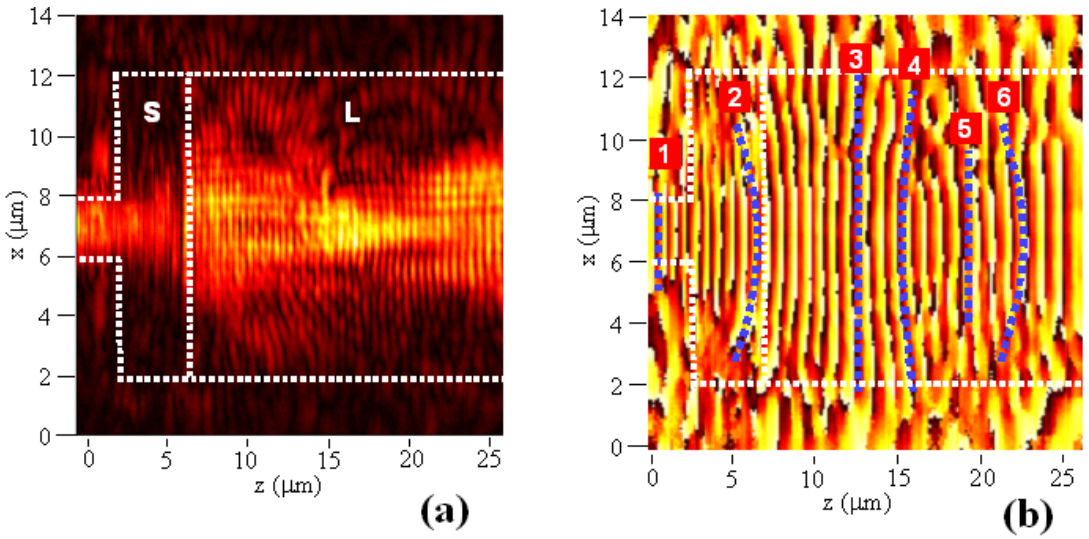

Fig. 5.11. High-resolution image near-field (a) amplitude and (b) phase distributions showing focusing effect inside the lens.

The cross sections (z-position is held constant) of the phase at the approximate locations of the number labels on Fig. 5.11b can be plotted to illustrate the phase front evolution

(Fig. 5.12). Unwrapping was used to demonstrate the parabolic dependence of the phase in the structure – a 2nd degree polynomial fits the experimental points quite well.

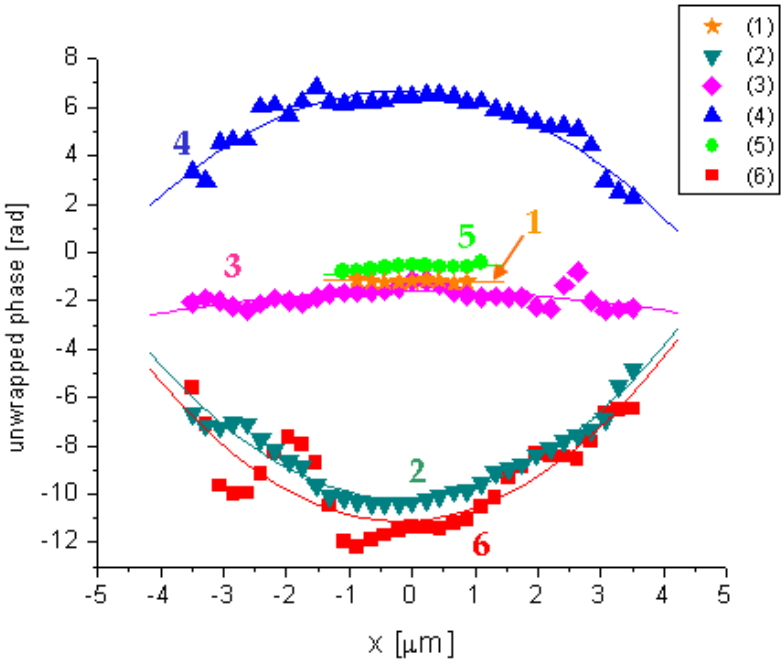

Fig. 5.12. Cross sections of the phase distribution at the z-positions characteristic to different locations on the device.

The consistency in the shorter than expected focal distance for different samples made us look closer at the SEM images of the fabricated devices (Fig. 5.13). It turned out that the smallest air gap in the actual device is 50 nm as oppose to the 100 nm in our design, which can be ascribed to proximity effects of fabrication which possibly occur on the e-beam patterning stage due to charging of the sample. This effect can be accounted for in the further rounds of sample fabrication by recalibrating the machine or by adjusting the design of the structure.

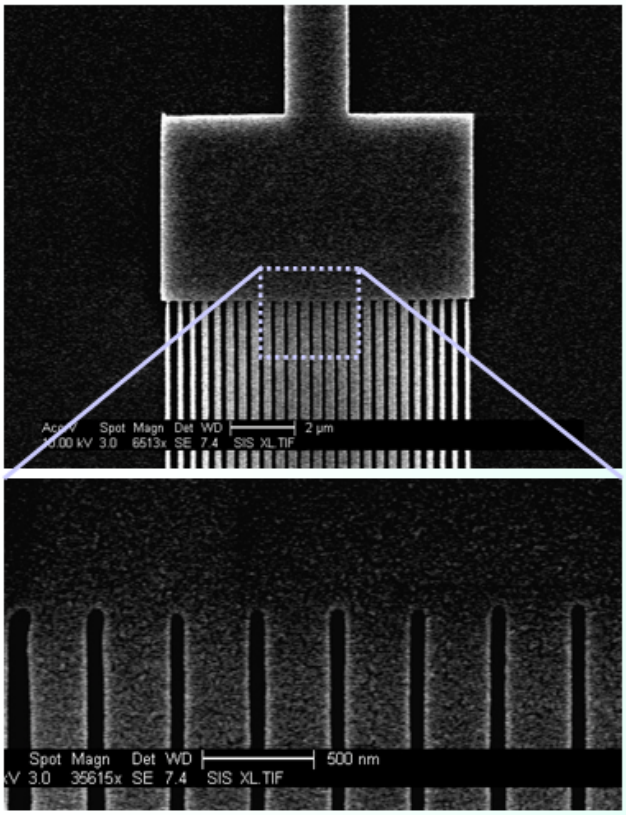

Fig. 5.13. SEM micrograph showing central part of the subwavelength grating stracture. Boxed area shows approximate location of the zoomed image.

We wanted to double check the new findings by performing numerical modeling with the actual geometry of the device obtained in the SEM characterization. After substitution of the new values in the model the obtained result (Fig. 5.14) confirms the "over-focusing" effect observed in the HNSOM measurements.

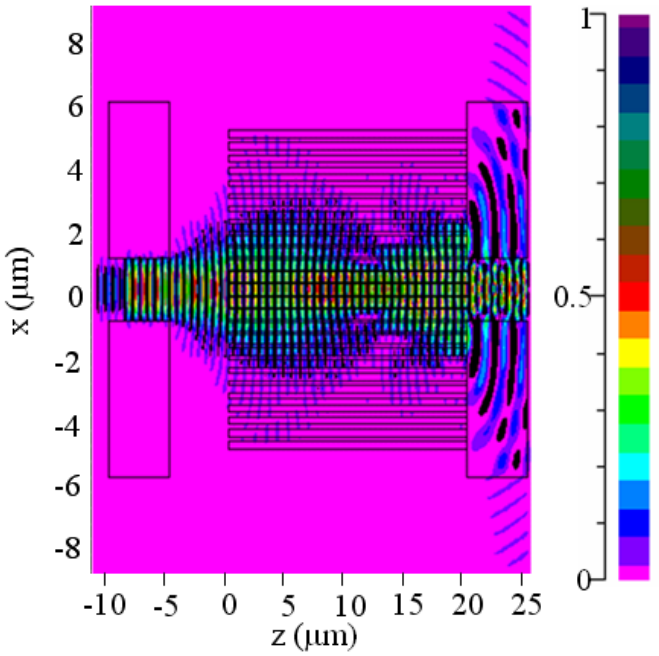

Fig. 5.14. Numerical modeling result showing the light propagation in the planar lens with geometry parameters taken from the SEM micrographs measurements.

6. Near-field microscopy with spectrally broad sources

6.1. Time-dependent properties of the photonic nanodevices

Information cannot be transmitted by the time-independent CW sources; there should be always some discontinuities in the optical fields. In optical communications amplitude modulation of the high-frequency carrier is typically used: the information can be coded in pulses and there are different data encoding techniques [63, 64] – return-to-zero, non-return-to-zero, etc. To transmit more information per unit of time the pulses become shorter and shorter and the system properties governing their propagation can be very different from those for the quasi-stationary signals.

For fiber-optic telecommunications the carrier wavelength is usually around $\lambda = (1550 \pm 20)$ nm, near-infrared region where the propagation losses in optical fibers are minimal. Bandwidth of 10 Gigabit per second is routinely used in optical networks; components for 40G and 160G are being developed. Modulation speeds on the order of 1 ps and faster are needed for such high data bandwidths. Further increase in transfer efficiency can be achieved using so-called Wavelength Division Multiplexing (WDM), the technique allowing several carrier frequencies modulated with different data streams to be present in a single optical fiber. In this approach a multiplexer on the transmitter

side is used to join several signals together, and on the receiver side a demultiplexer is used to split separate data streams to the different detectors.

Application of photonic nanodevices to electrical-to-optical conversion, multiplexing/demultiplexing, switching and optical signal processing is very promising nowadays. Thus it is crucial to learn about short pulse propagation on the nanoscale level and to characterize properties of nanodevices with respect to pulse propagation. Another reason for ultrashort pulses to be studied is the high peak power and therefore large nonlinearities associated with their propagation. This can be considered as a negative effect in optical data transmission as it can distort the pulse shapes and corrupt the data. For simplicity purpose and considering low typical average power in optical processing systems we will limit our investigation of the pulse propagation in nanodevices to only the linear phenomena. On the other hand a study of nanoscale nonlinear effects can be interesting for some other applications and can be also performed using near-field microscopy approach.

Short pulses can be described as optical frequency oscillations with a sharp temporal dependence of amplitude envelope:

$$E(t) = \sqrt{I(t)} \cdot e^{i\omega_0 t} e^{i\psi(t)} \qquad (6.1),$$

where ω_0 is the optical frequency, $I(t)$ is the intensity envelope function, and $\psi(t)$ is the temporal phase. For such pulses the characteristic time is usually 100 ps and less, while pulse durations from 200 fs to 10 fs can be provided by ultrafast lasers. In the frequency domain this pulse can be described as:

$$E(\omega) = \sqrt{S(\omega)} \cdot e^{i\phi(\omega)} \qquad (6.2),$$

where $S(\omega)$ is the spectrum function and $\varphi(t)$ is the spectral phase. According to Fourier analysis these two representations are related with Fourier transform:

$$E(\omega) = \mathrm{F}\left\{E(t)\right\} \qquad (6.3).$$

From this it follows that the shorter the temporal duration of the pulse the wider is the spectral bandwidth (for a transform-limited pulse). For a Gaussian pulse with constant spectral phase we have:

$$\Delta\omega \approx \frac{0.44}{2\pi}\frac{1}{\Delta t} \qquad (6.4),$$

where $\Delta\omega$ is the width of the spectrum and Δt is the pulse width.

The envelope $E(t)$ of a pulse propagates in space with the speed different from the speed of the phase propagation of the spectral components of the pulse. The definition of group velocity is

$$v_g \equiv \frac{\partial\omega}{\partial k} \qquad (6.5).$$

Similarly group refractive index $n_g = c/v_g$ can be defined. After some transformation we can obtain:

$$n_g = \frac{c}{v_g} = c\frac{\partial k}{\partial\omega} = \frac{\partial}{\partial\omega}(\omega\cdot n(\omega)) = n(\omega) + \omega\frac{\partial n}{\partial\omega} \qquad (6.6),$$

where $n(\omega) = n_{\mathrm{eff}}$ effective, or phase, index. In terms of the wavelength it can also be rewritten as:

$$n_g = n_{eff} - \lambda\cdot\frac{\partial n_{eff}}{\partial\lambda} \qquad (6.7).$$

In general due to material dispersion the refractive index depends on the wavelength of propagating light, this makes the derivative in (6.7) nonzero and then the group index is different from the effective phase index. Usually most materials in the wavelength range where they are transparent have a negative sign of the derivative, i.e. the refractive index n decreases with increasing wavelength λ, thus this situation is called normal dispersion. For some wavelengths or special geometries the reverse situation is possible, leading to a so called anomalous dispersion.

Another important parameter of nanophotonic components with respect to polychromatic light propagation is group velocity dispersion (GVD), which is defined as

$$\beta \equiv \frac{\partial}{\partial \omega}\frac{1}{v_g} = \frac{\partial^2 k}{\partial \omega^2} \qquad (6.8).$$

It determines how an optical pulse broadens in the system. Pulse broadening is considered a negative effect in optical communications and signal processing as it deteriorates the SNR for high-speed communications.

6.2. Methods to measure group velocity and dispersion

There are various methods to study pulses in nanostructures and the properties governing their propagation. Far-field methods are simpler in implementation, but usually are limited to “black box”-type analysis, i.e. it is hard to distinguish the contributions of the different components in a circuit. In the case when the out-of-plane radiation is significant it is possible to directly track the propagation of the optical pulse [65], but those cases are rather rare for modern low-loss nanophotonic devices. Near-field methods provide local sub-diffraction-limit measurements of the light propagating in the

nanophotonic circuit and can in principle map the important pulse propagation parameters for each component.

In the classical configuration of far-field group velocity measurements pulses are coupled to nanophotonic devices and then the output is studied [66]. Due to the limited temporal resolution of direct detection correlation techniques are usually used for pulse delay measurements. Schemes similar to heterodyne detection with variable reference arm length can be implemented. Cross-correlation or autocorrelation shape analysis can also be used to estimate the effects of GVD and pulse broadening [67]. It is rather hard to obtain information on what is happening to the pulse as it propagates inside the nanophotonic structure. Proper calibration is critical in this approach; also to provide some analysis the cut-back method is often used, which provides measurements of similar parameters for structures with different propagation lengths.

Another method to obtain the parameters governing pulse propagation is through analyzing continuous light transmission for different wavelengths inside the nanophotonic structures. For example group refractive index of a waveguide could be measured by fabricating an on-chip Mach-Zehnder interferometer with the desired geometry. The arm length difference in this structure will cause interference at the recombining directional coupler and fringes on the transmission spectrum [68]. The distance between maxima and minima is dependent on the group index of the waveguide [69]:

$$n_g = \frac{\lambda_{\min} \cdot \lambda_{\max}}{2\Delta L \left| \lambda_{\min} - \lambda_{\max} \right|} \qquad (6.9),$$

where λ_{min} and λ_{max} are the positions of the adjacent minimum and maximum and ΔL is the length difference of the interferometer arms.

A similar effect can be obtained in a Fabry-Perot-type interferometer. The cleaved ends of a single waveguide create a pair of partially reflecting mirrors due to the Fresnel reflections from the boundaries of high and low refractive index media. Thus the configuration shown for example in Fig. 3.2 acts as a Fabry-Perot interferometer with considerable fringe visibility. The group index in such a waveguide can be obtained by measuring spectral transmission characteristics:

$$n_g(\lambda_0) = \frac{{\lambda_0}^2}{2L \cdot \Delta\lambda} \qquad (6.10),$$

where L is the length of the waveguide between input and output facets (if L is comparable with the wavelength then phase shifts from the reflections should be also included in the picture), and $\Delta\lambda$ is the Free Spectral Range (FSR) – the distance between two adjacent maxima or minima in transmission closest to the λ_0. Note the similarity of formulas (6.9) and (6.10) – the underlying effects are similar and in the case of Fabry-Perot configuration the effective length difference of the two waves is equal to the doubled length of the resonator.

We fabricated a chip with a set of L-shaped SOI waveguides with rectangular cross sections of 250 nm x 500 nm, 250 nm x 700 nm, 250 nm x 900 nm, 250 nm x 1100 nm, and 250 nm x 1300 nm (Fig. 6.1a). The input and output facets of the waveguides were cleaved at an angle close to 90° thus creating Fresnel reflection mirrors and Fabry-Perot interferometers.

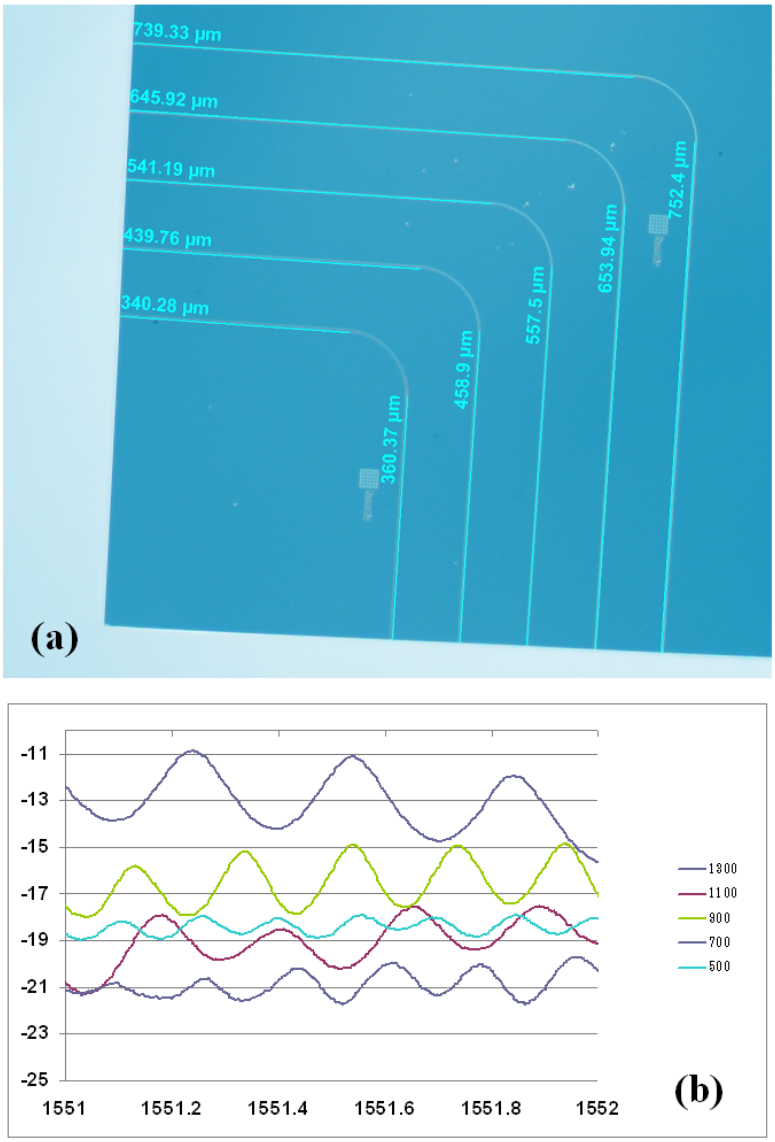

Fig. 6.1. (a) The set of the SOI waveguides with different widths (500 nm to 1300 nm) and cleaved input and output facets; (b) transmission spectra of the Farbry-Perot interferometers created by Fresnel reflections in such waveguides.

The transmission of the interferometers shows spectral fringes with approximately 3dB modulation. From formula (6.10) the period of the fringes approximately corresponds to group index of $n_g = 3.9\text{-}4.5$. The measurement errors were not calculated and the accuracy of these values can be quite low due to low modulation depth. The group index

values significantly exceed the effective index or index of phase fronts propagation in the waveguides. They are even higher than index of refraction of bulk Silicon – this emphasizes the contribution of the waveguide dispersion and shows that the derivative $dn_{eff}/d\lambda$ has a negative sign.

The disadvantage of the far-field methods was already pointed out before and consists of inability to study the local parameters. Thus near-field methods were developed to study the pulse's propagation. Recently it was shown that the HNSOM setup can be used for tracking of ultrafast laser pulses in the nanophotonic structures [70-73]. The Mach-Zehnder configuration should in this case have matching lengths of interferometer arms. Only when the length of the reference arm is equal to the length of the signal arm (including the portion of nanophotonic device under study) the maximum signal can be observed. To study the pulse at different locations in the nanophotonic circuit a variable delay line should be added. While the final amplitude or intensity distribution obtained with NSOM might look like a snapshot of a single pulse propagating in the device, it is obviously not the case since the scanning process takes a lot of time. Even during the detection at each scan point the probe picks up contributions of a number of pulses. No special synchronization is needed to keep the pulse in place while scanning the tip, since the amplitude oscillating at the reference frequency is fixed by the position of the delay line and the probe (to achieve overlap of the pulses travelling in different arms). In that sense the "spatial" cross-correlation (which is not a cross-correlation, strictly speaking [70]) of the ultrashort pulse propagating in the HNSOM setup is measured. By measuring the pulse peak positions at the different delay times the group velocity in the waveguide can be calculated. The "temporal" cross-correlation can

be also obtained in such a setup by fixing the tip position in contact with the device and scanning the delay line. The latter method is useful for pulse distortion analysis or measurements of pulse broadening (occurring due to GVD) by taking the temporal cross-correlations at two different positions of the photonic circuit [74]. Of course the dispersion also acts on the pulse propagating in the reference arm; it was shown [75] that the difference in the dispersion in two arms of interferometer can cause cross-correlation pulse broadening and lower the peak value, which deteriorates temporal resolution and reduces SNR.

It is also possible to find the group velocity of pulse propagation by measuring the spectrum evolution inside a multimode waveguide [76]. This method can work for direct (non-heterodyne) NSOM detection, but is limited to multimode waveguides – a rather rare case for nanophotonic signal processing devices. Similarly, in the far-field case of PhC devices the group velocity can be inferred from the photoluminescence spectra in some special geometries [77].

6.3. HNSOM measurements with spectrally broad sources

Continuous sources with finite spectral content also have a limited temporal coherence length and thus their cross-correlation in the HNSOM setup depends on the arm length difference. In fact, the coherence time is inversely proportional to the spectral bandwidth:

$$\tau_c = k\frac{\lambda_0^{\,2}}{c\cdot\Delta\lambda} \qquad (6.11),$$

where λ_0 is central wavelength $\Delta\lambda$ is width of the spectrum curve and k is the spectrum form-factor coefficient ($k = 0.32$ for Lorentzian spectral dependence and $k = 0.66$ for Gaussian spectrum) [78]. Thus as a low-coherence source which would provide similar response in the HNSOM setup one could use a broad-spectrum continuous optical source. This realization can provide a cost-effective solution for group velocity measurements; also CW sources usually have smaller form-factor and better stability than ultrashort pulse sources. In addition, since the SNR of HNSOM detection is dependent on the average power (detectors typically are not as fast as a laser's repetition rate), but nonlinear effects are dependent on the instantaneous power, similar signal levels can be obtained in the case of continuous broad-spectrum sources with lower distortions, occurring due to nonlinear effects.

As a quick proof of concept we used an erbium doped fiber amplifier with no seed signal producing a broad-spectrum amplified spontaneous emission signal. The source was characterized using an optical spectrum analyzer and has a double peak spectral shape (Fig. 6.2a). The width of the stronger peak is 4 nm FWHM.

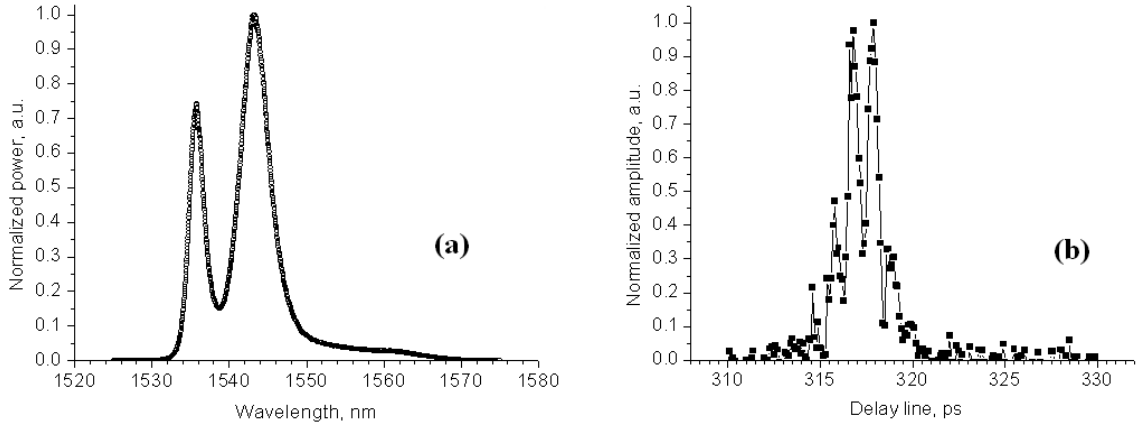

Fig. 6.2. (a) Experimentally measured spectrum of the unseeded fiber amplifier; (b) temporal cross-correlation of the source in the HNSOM interferometer.

This source was coupled to the HNSOM setup with a channel silicon waveguide. The tip position was fixed in contact with the waveguide and the delay line value was varied to obtain temporal cross-correlation of the source (Fig. 6.2b). The temporal cross-correlation also has a double peak shape with two approximately equal peaks with FWHM of 0.7 ps. This value approximately corresponds to the coherence time of the broad-spectrum source calculated using formula (6.11) assuming a Lorentzian spectral shape, which gives $\tau_c = 0.64$ ps. Then the delay line position was fixed around the peak and the probe was scanned to obtain the HNSOM image. The obtained amplitude distribution (Fig. 6.3) shows the finite "pulse-like" shape with double peak structure. The peaks are rather wide and the second peak does not fit in to the scanning window limited to 70 μm. This and some fine oscillations significantly complicate exact peak position determination, thus ideally sources with broader spectral content and with regular (single Gaussian) shape should be used.

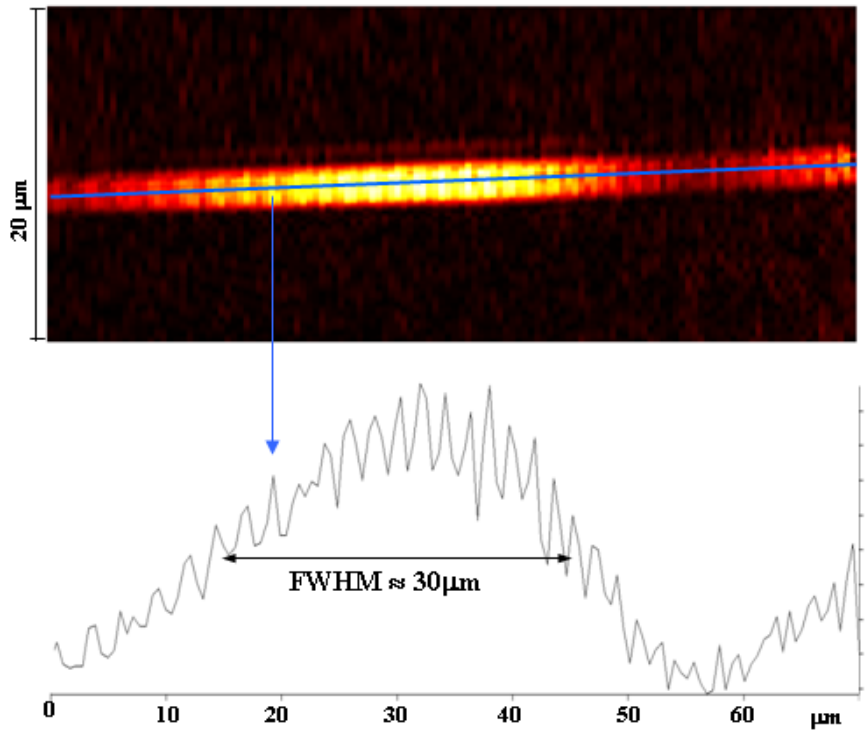

Fig. 6.3. Spatial cross-correlation of the broad-spectrum unseeded fiber amplifier source in the HNSOM interferometer with channel silicon waveguide.

By changing the delay line position it is possible to shift the peak of the cross-correlation inside the waveguide. This is similar to the ultrashort pulse tracking in the previously reported experiments [70].

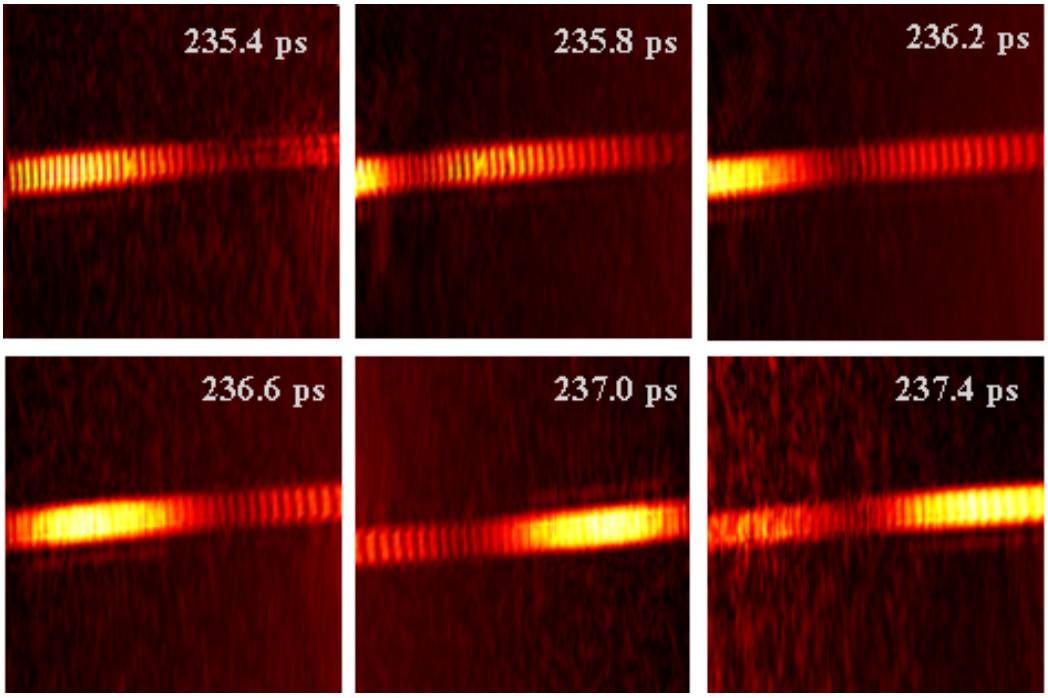

Fig. 6.4. HSNOM amplitude (70 μ x 20 μ) distributions of the unseeded optical amplifier source in the silicon channel waveguide.

The group velocity in the structure can in principle be found by measuring the peak position vs. the delay line value, but the broad shape makes it hard to determine the exact peak position and leads to large errors.

Another advantage of using low-coherence sources is that they can significantly reduce the contribution of the parasitic light which comes from scattering, occurring for example at the point of coupling the light from fiber to a nanophotonic device. The measurements of the same section of the waveguide as on Fig. 6.3 obtained using highly coherent tunable CW laser is shown on Fig. 6.5. In this case a large amount of scattered light distorts the image; also some interference fringes can affect the mode profile characterization. The scattered light is travelling in the free space and thus its optical path

length is very different from that of for the waveguide mode and with low coherence sources it does not produce an interference term with the light in the reference arm.

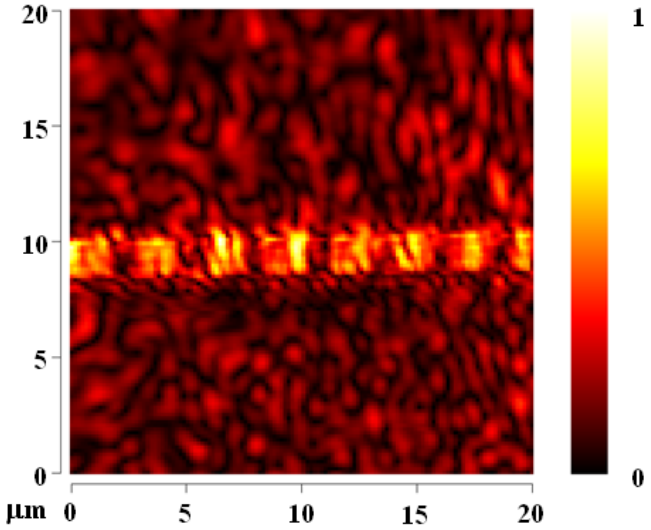

Fig. 6.5. Amplitude distribution for the silicon channel waveguide obtained using HNSOM with CW tunable laser in the presence of large scattering.

Superluminescent light emitting diodes (SLD) can provide powerful and spectrally broad output with regular spectral shapes (close to Gaussian). Such sources combine laser-diode-like output power with broad LED-like optical spectrum and they are often used in optical coherence tomography and similar applications. We use an Opto-Link OLSLD-15-HP4 superluminescent diode (SLD) (Fig. 6.6a) operating in the near-infrared region at a center wavelength of $\lambda_c = 1539$ nm, full width at half-maximum (FWHM) of the spectrum, $\Delta\lambda = 44.5$ nm, and output optical power of $P_{out} = 30$ mW. The measured power spectrum of the SLD source is shown in Fig. 6.6b.

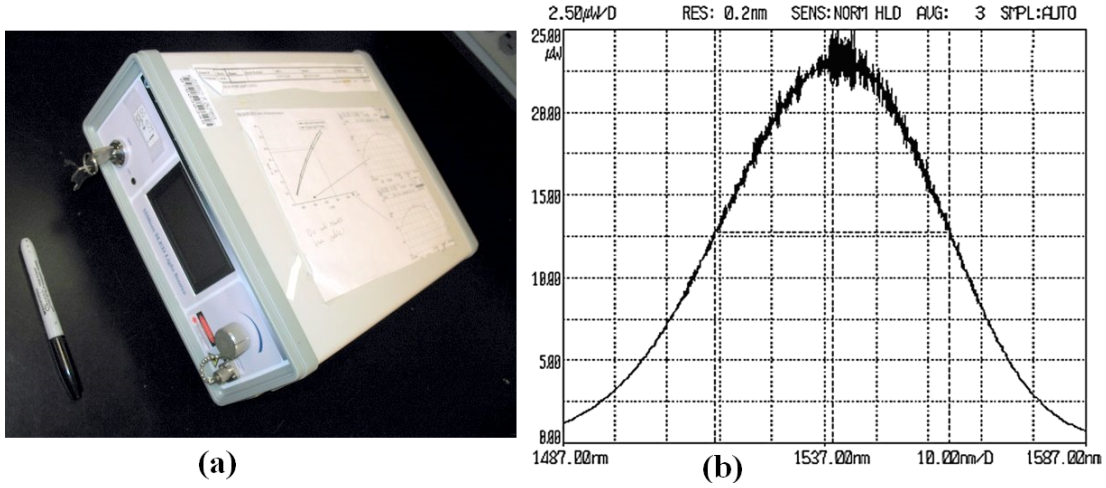

Fig. 6.6. (a) OLSLD-15-HP4 unit; (b) Measured spectral output of the device.

Superluminescent sources are cheaper, more compact and easier to operate compared to ultrafast laser sources, so it is very advantageous to use them for time-dependent HNSOM characterization.

The temporal coherence of our SLD can be estimated using formula (6.11) and if we assume Gaussian spectral shape we obtain:

$$\tau_c = k\frac{\lambda_0^{\,2}}{c\cdot\Delta\lambda} = 0.66\frac{(1540nm)^2}{3\cdot 10^5\, nm/\,ps\cdot 45nm} \cong 0.12\,ps = 120\,fs\,,$$

in other words the coherence length of our SLD source is approximately equal to that of the 120 fs transform-limited ultrashort pulse. In reality though the spectrum of our source somewhat deviates from Gaussian, and to take this into account one can perform Fourier transform to obtain the autocorrelation of the pulse thereby converting spectral information to the time domain. To perform this transformation the spectral data of the source was obtained using an optical spectrum analyzer, then the wavelength dependence was converted to the frequency variable and the data was interpolated to provide even

spacing. The Fast Fourier Transform (FFT) operation was performed on the newly obtained data and the result was plotted against a new time variable ranging from 0 to $\Delta t \cdot (N_{\text{samples}} - 1)$ with step $\Delta t = 1/(\max(\text{Freq}) - \min(\text{Freq}))$. All the operations described above were performed using MatLab software and the resulting autocorrelation is shown in Fig. 6.7. The curve is very close to Gaussian dependence and the fit is also shown on the picture. The FWHM of the autocorrelation is $\Delta\tau_{spectr} = 160$ fs, which is relatively close to the previous rough estimation of 120 fs.

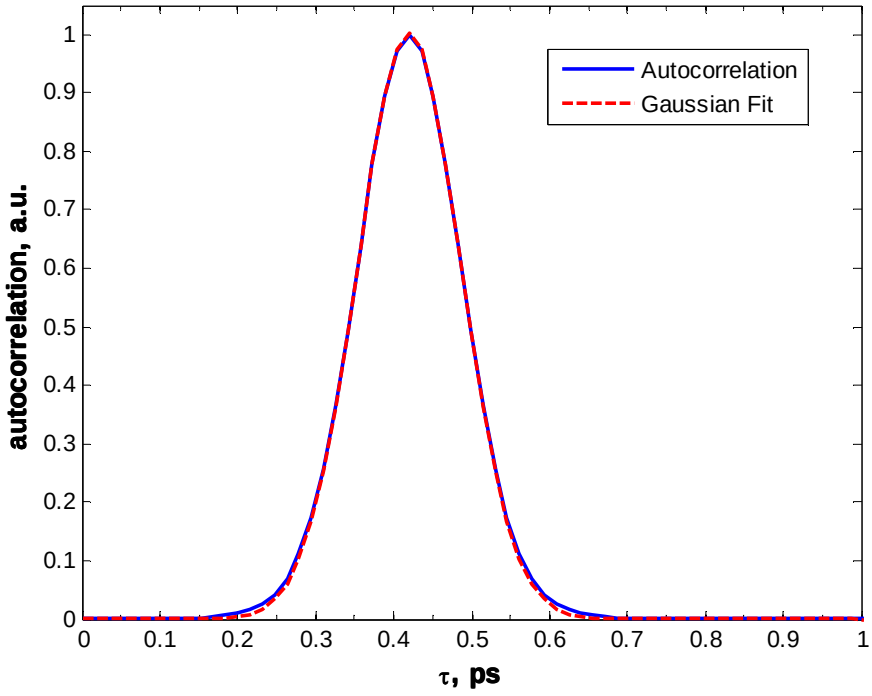

Fig. 6.7. Autocorrelation of the source spectrum.

In the HNSOM setup the polychromatic spectrum can be distorted due to dispersion in different components: optical fibers, splitters, AOMs, etc. It was shown that if the two arms of the Mach-Zehnder interferometer of the HNSOM have very

different dispersion characteristics then the cross-correlation becomes wider and SNR becomes lower. For optimal detection efficiency the dispersive media in the two interferometer branches should be balanced [75]. To analyze the dispersion difference in the setup the temporal cross-correlation can be measured by placing the probe in contact with starting sections of the nanophotonic device and then scanning the delay line. The maximal interference signal can be observed when the lengths of the interferometer branches are equal, the width of the curve represents the spectral characteristics of the source and dispersion contribution. In the classical HNSOM setup with the two AOMs in the reference branch (Fig. 2.2) the dispersion difference of the arms leads to the significant widening of the cross-correlation (Fig. 6.8). The FWHM of 0.6 ps is observed in this case, and thus almost no improvement compared to the unseeded EDFA is gained for the SLD source.

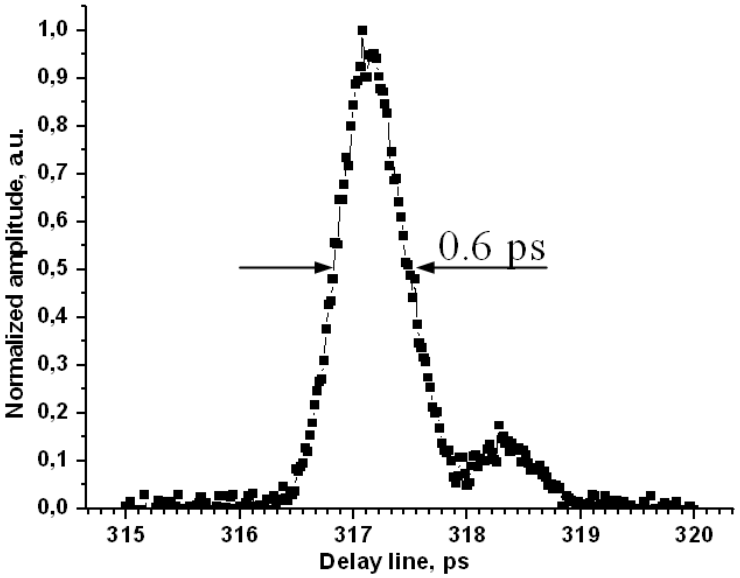

Fig. 6.8. Temporal cross-correlation of the SLD source in the HNSOM interferometer with two AOMs in the reference arm.

To reduce the difference in dispersion we propose symmetric arrangement of the AOMs in the arms of the interferometer (Fig. 6.9). In this case the modulators should provide the frequency shift in the same direction, i.e. utilize the same-sign diffraction order, for the interference term to be at ~10 kHz range.

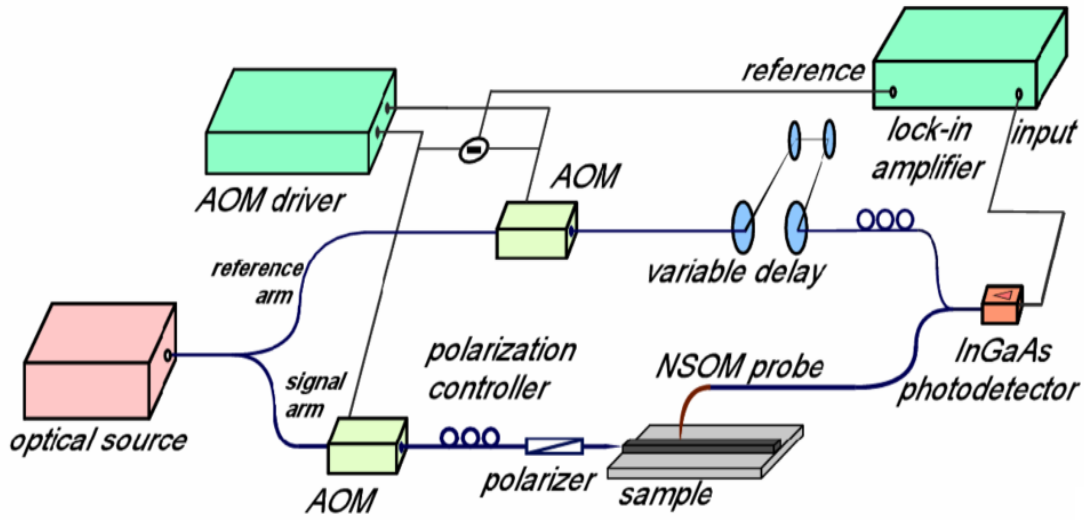

Fig. 6.9. Scheme of the HNSOM setup with the symmetric arrangement of AOMs to reduce the difference of the dispersion in two interferometer arms.

In our case the modulator in the reference arm is upshifting the frequency by 40.07 Mhz and the AOM in signal arm is upshifting the frequency by 40 MHz, so the interference term is the same 70 kHz as in the previous scheme. The temporal cross-correlation taken for the SLD source in the setup (Fig. 6.10) shows much less broadening and is comparable with the theoretical limit. The FWHM of temporal cross-correlation estimated from this measurement is $\Delta\tau = 180$ fs; the ~10% broadening factor in comparison to the spectrum autocorrelation is tolerable for these measurements and is partially attributable to the dispersion of a portion of the optical waveguide.

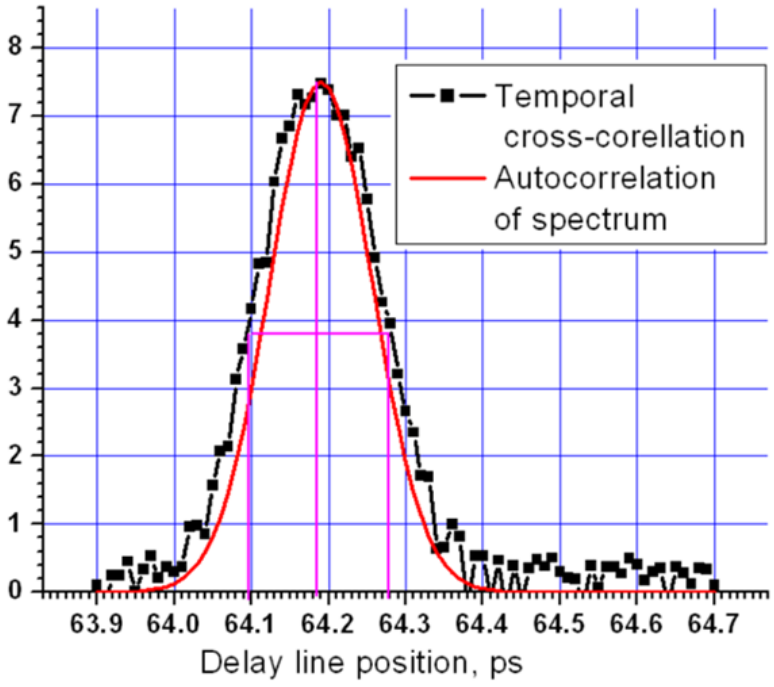

Fig. 6.10. Temporal cross-correlation of the SLD source in the HNSOM interferometer with symmetric arrangement of AOMs. Autocorrelation of the source is given as a reference and the ideal cross-correlation in the absence of the dispersion difference.

Similarly the spatial cross-correlation can be obtained by fixing the delay line position and scanning the near-field probe. This will result in a finite "pulse-like" measured amplitude distribution in the investigated nanodevice. A typical result for the SOI waveguide with dimensions 700 nm by 250 nm is shown on the Fig. 6.11. The cross-section along the waveguide gives the width of the amplitude peak as approximately $\Delta L = 20$ μm. Using this value and the previously obtained temporal cross-correlation width of $\Delta\tau = 180$ fs roughly under the assumption of no spectral distortions the effective index of the waveguide can be calculated:

$$n_{eff} = c \cdot \frac{\Delta\tau}{\Delta L} = 300 \frac{\mu m}{ps} \cdot \frac{0.18 ps}{20 \mu m} = 2.7 .$$

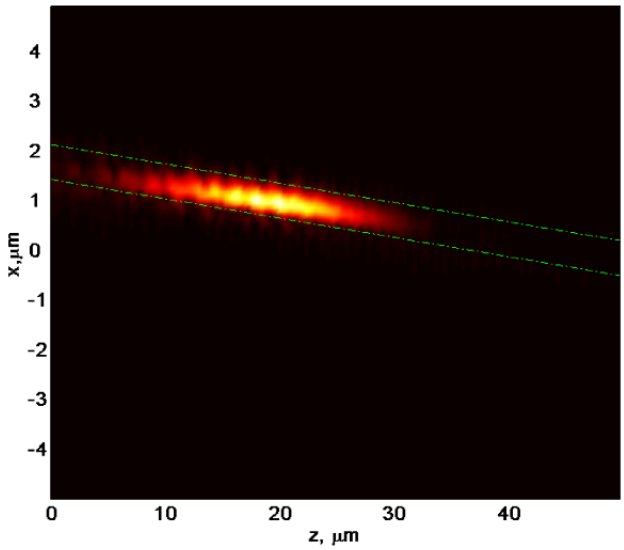

Fig. 6.11. Spatial cross-correlation of the SLD measured by HNSOM with symmetrically arranged AOMs in the SOI channel waveguide.

The Beam Propagation Method (BPM) mode solver from RSoft can be used to calculate the effective refractive indices for the mode at a specific wavelength. Such numerical methods do not account for fabrication tolerances, waveguide wall roughness, etc., but in most cases the values obtained in computer simulations give a good approximation. The effective refractive indices of TM polarization mode for the SOI channel waveguide with a cross section of 700 nm x 250 nm for the wavelengths around $\lambda_c = 1539$ nm with a spectral step of 1 nm were calculated. Specifically $n_{eff} = 2.13$ was found for $\lambda = \lambda_c$. Knowing the effective indices at a particular wavelength and in the vicinity spectrum allows calculation of group refractive index from the Eq. 6.7. Implementing a simple two-point estimation of the derivative we get numerical estimation of $n_{gr} = 4.39 \pm 0.03$ within FWHM band of λ_c.

HNSOM optical phase data also allows us to obtain the effective refractive index value experimentally. The near-field phase distribution measured with SLD source in the system described above is shown on Fig. 6.12a, one can see a pretty stable picture of phase fronts normal to the direction of light propagation. The cross section of the distribution along the center of the waveguide (Fig. 6.12b) shows fringes with a somewhat longer period at the left compared to the period at the right side due to dispersion. The average effective refractive index $n_{eff} = 2.3 \pm 0.1$ is found from the phase fringe period across the picture. To improve the accurateness of the phase measurements images with better resolution should be taken and the interferometric stability of the HNSOM setup should be enhanced.

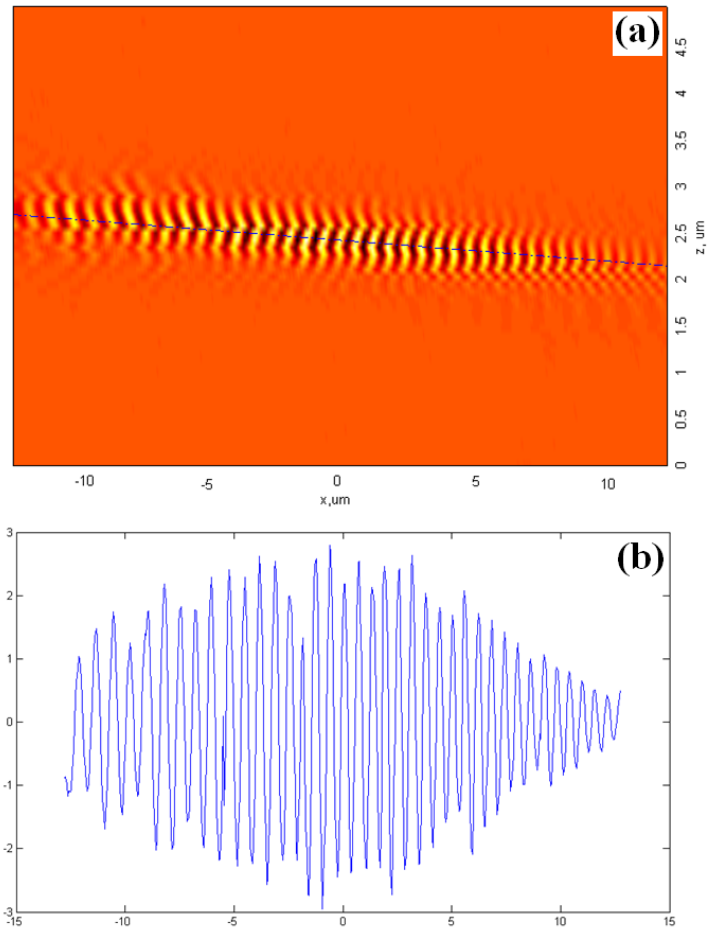

Fig. 6.12. (a) Optical phase distribution obtained for the SOI waveguide obtained the HNSOM setup with SLD source; (b) Cross-section of the image showing phase fronts.

For experimental group index determination the position of the peak should be measured at different delay line values and then the distance in the waveguide and in the free space can be related. Amplitude distributions measured for a 700 nm x 250 nm SOI channel waveguide with HNSOM at different positions of delay line are shown on Fig. 6.13. The images show very low amplitude levels outside the waveguide. The cross-correlation pulse has a well defined shape with some trailing low amplitude post pulses occurring probably due to some scattering or reflections in the HNSOM setup. The amplitude inside the waveguide is integrated in the direction across the waveguide and

then plotted vs. the position along the waveguide (Fig. 6.14a). The shape of the cross-correlation pulse is approximately Gaussian with a FWHM of 15 μm and constant through the measured distance.

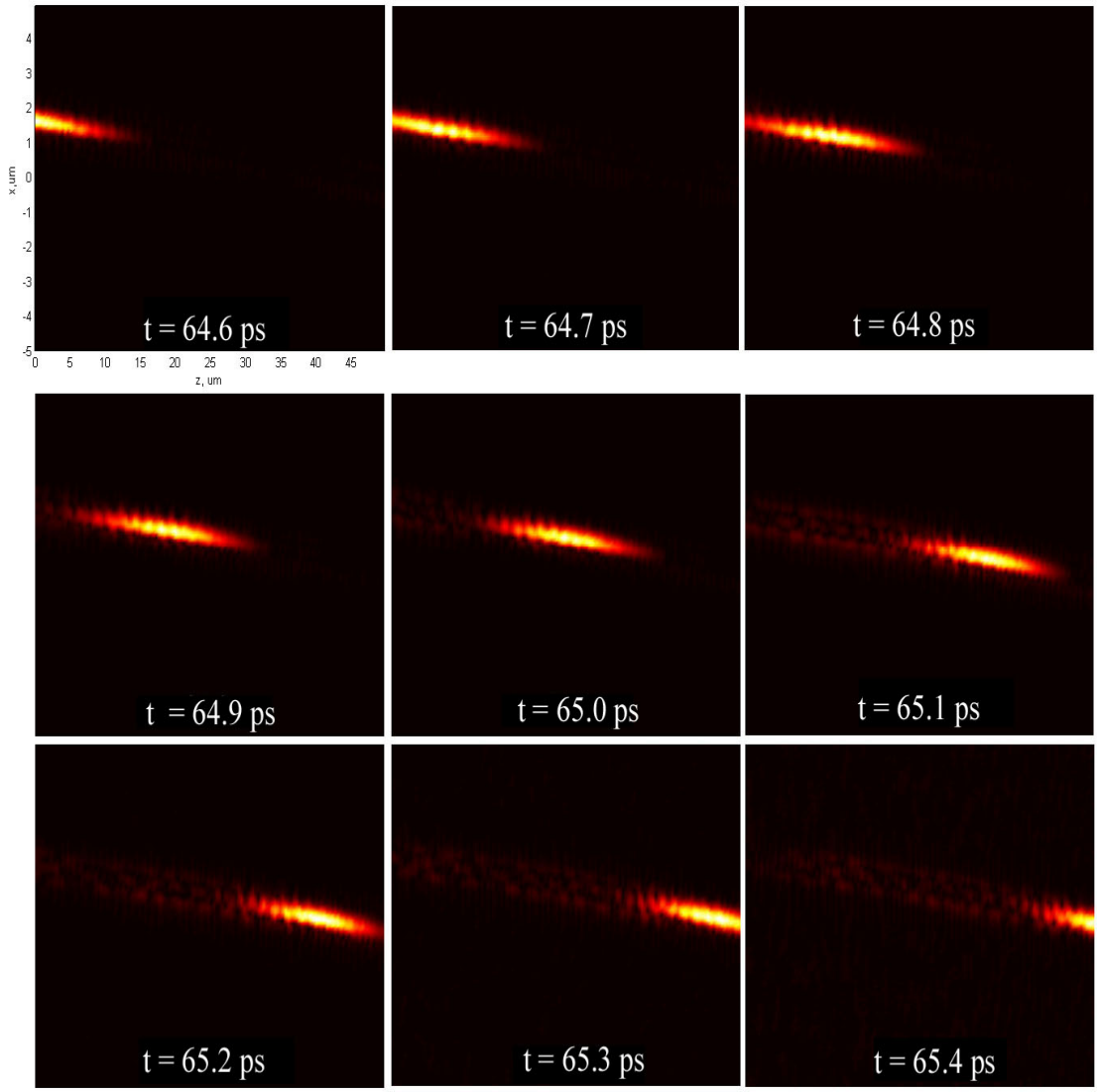

Fig. 6.13. HSNOM amplitude (50 μ x 10 μ) distributions of the SLD source in the silicon channel waveguide for different delay times.

The cross-correlation maxima positions is plotted vs. delay line position and fitted with a linear equation (Fig. 6.14b). The proportional coefficient of the fitting equation has the dimension of [μm/ps] and gives the velocity of propagation of the peak maximum. The group index of the waveguide is determined as $n_{gr} = c / v_{gr}$, where c is the speed of light in vacuum, and v_{gr} is the obtained group velocity. From the linear fitting we get $v_{gr} = 68.78 \pm 2.95$ μm/ps and thus $n_{gr} = 4.36 \pm 0.19$.

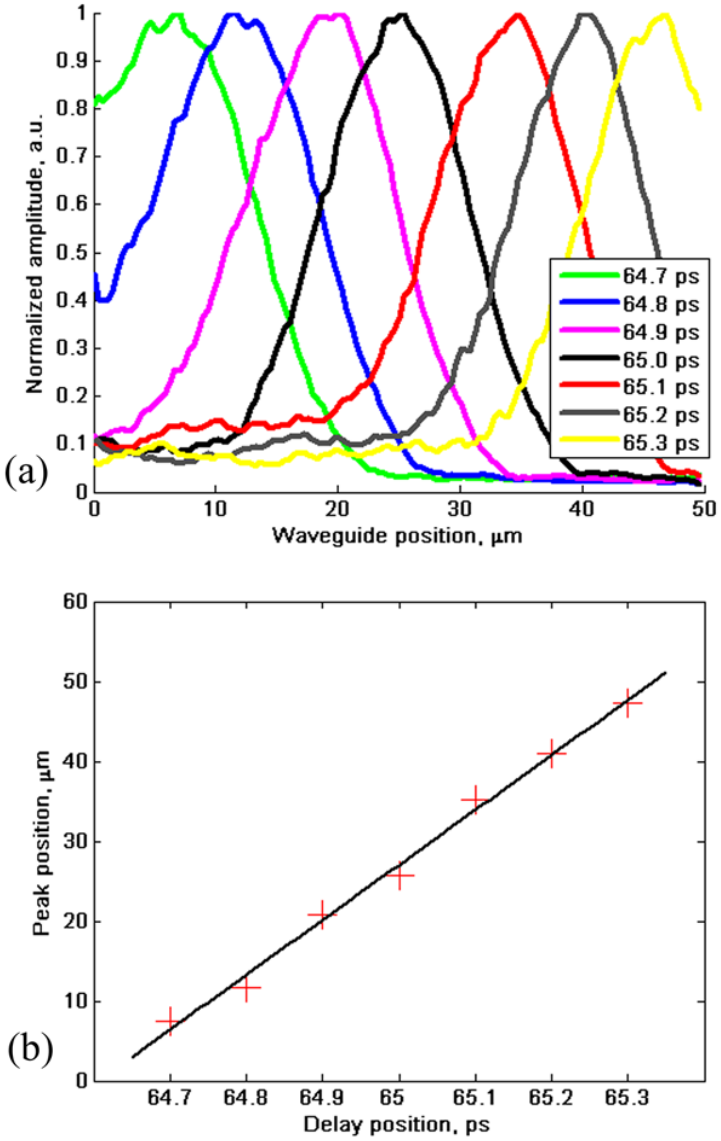

Fig. 6.14. (a) Optical amplitude over the waveguide length for different positions of the delay line; (b) Positions of the amplitude maxima and their linear fitting.

Similar experiments can be performed for waveguides with different geometrical parameters as well as other photonic nanodevices. We measured group velocities for a set of SOI channel waveguides (Fig. 6.1a) and calculated group refractive indices for them (Fig. 6.15). In general, the values for the group index in SOI waveguides are strongly

dependent on the waveguide geometry and wavelength, and as evident from the results reported in [68, 79-81], the group indices for waveguides with similar geometries vary between 4 and 5. The errors of our near-field index characterization can be decreased by taking higher resolution images and by using a higher precision variable delay line. Our current image pixel size is approximately 470 nm, whereas the probe aperture, and thus the approximate spatial resolution limit, is 200 nm; in addition the documented accuracy of the delay line used in our setup is ±0.02 ps.

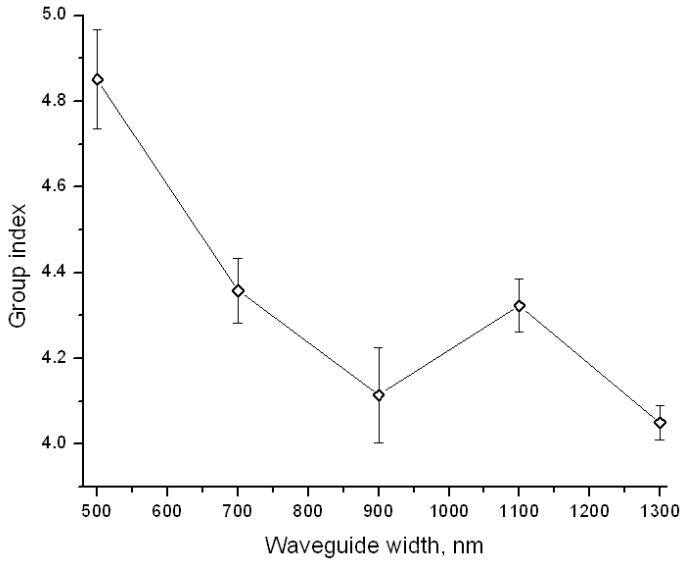

Fig. 6.15. Experimentally obtained values of group indices for the SOI channel waveguides with the height of 250 nm and widths of 500 nm, 700 nm, 900 nm, 1100 nm, and 1300 nm.

7. Summary and future research directions

7.1. Summary of the thesis

This dissertation shows the advantages of the Heterodyne NSOM approach in photonic nanodevice characterization. First, the principles of near-field microscopy and heterodyne detection were discussed. Then it was shown that the near-field probe can affect the device under investigation. For example a microring resonator changes the *Q*-factor ($\Delta Q/Q_0 = 57$ %) and resonant wavelength ($\Delta\lambda = 1$ nm) in the process of probe scanning. Thus for high-*Q* structures the NSOM approach (especially with the metal-coated or high refractive index probes) cannot provide accurate measurements of device parameters.

A number of photonic nanodevices utilizing the PhC concept of index of refraction periodically changing with a scale comparable to a wavelength of light were demonstrated and studied using the HNSOM technique. Specifically single-line defect waveguide mode structure was studied using the Fourier modal analysis approach. It was shown that two different modes can be excited in such structure and that the excitation conditions depend on the wavelength of coupled light. The losses between the components of the structure – tapered channel waveguide and PhC waveguide – were estimated based on the experimental data. Furthermore, the performance of more

complex PhC devices such as a photonic lattice with self-collimating property and a polarization beam splitter based on the boundary effects between two PhC lattices were demonstrated using near-field measurements.

Another approach to photonic nanodevice design in which free space optical components are transferred to a chip by utilizing deeply subwavelength index variation, the so called metamaterial approach, was also discussed. The designed and fabricated devices utilizing this principle were characterized using HNSOM. It was shown that the subwavelength structured graded index lens possess the ability to focus the light, but the characterization has also revealed fabrication errors deteriorating the specific device functionality.

It was also proposed to use spectrally broad CW optical sources which possess low temporal coherence length to characterize the dispersive properties of photonic nanodevices. The specific configuration of the heterodyne setup which has AOMs in two different arms was shown to have enhanced performance in this case. The SLD source was shown to have a narrow cross correlation with a Gaussian shape in the HNSOM setup. The group velocity of cross correlation propagation and the group refractive indices were measured for a set of SOI channel waveguides.

7.2. Future research directions

The field of nanophotonics is rapidly growing and has a lot of promise in the all-optical signal processing and data transmission as well as in biological and chemical related applications such as sensing and material analysis. Experimental characterization

of nanophotonic components and circuits is an important step in fabrication and concept validation, and subwavelength resolution and access to evanescent fields delivered by NSOM will be indispensable for such characterization.

As it was shown in this thesis the probe affects performance of the device in the process of investigation, so some special probe designs should be used for highly resonant structures. Less effect can be expected from the sharp apertureless probes and metallic nanoparticle probes and therefore a similar study should be performed with these types of near-field probing techniques.

A lot of the nanophotonic devices have a solid overcladding which reduces losses and provides the symmetric environment around the photonic components. This significantly complicates probing of the near field. The overcladding can be removed at points of interest, but this may affect the functionality of the device. The solution can be found in filling the removed overcladding areas with index matching fluid which will allow the access of the near-field probe to the surface of the waveguiding components but will create only minimal perturbation to the device performance. The liquid environment complicates AFM feedback of the NSOM system and usually only allows the sample to be scanned under a fixed position probe. To achieve similar coupling condition throughout the characterization process the optical fiber delivering light to the device should be attached rigidly to the nanophotonic chip. This is a rather challenging procedure but it is significant to master this step for experiments with fluidic imitation of the solid overcladding for near-field characterization.

NSOM with low-coherence sources is a very promising technique for characterization of the dispersive properties of photonic nanodevices especially ones

designed for optical data processing or nonlinear optical applications. More detailed study of the group refractive indices should be performed and the technique for characterizing other parameters (group velocity dispersion, etc) should be developed. An additional advantage of the low-coherence approach is that it allows filtering of scattered light which can be beneficial for characterization of the devices combining conventional waveguides and metallic components with surface plasmon light propagation.

While our HNSOM setup allows simultaneous measurement of the device topography, optical amplitude and phase, it is still can be enhanced with polarization resolving capability. A polarization diversity detector can be used for this purpose, which is essentially comprised of the polarization beam splitter and a pair of photodetectors. Random birefringent properties of single mode optical fibers can be one of the obstacles in the realization of the polarization resolving detection so the solution can be in recreating the HNSOM setup in polarization maintaining fibers or in a free-space. The polarization properties of near-field probes should be also thoroughly studied.

References:

1. E. Abbe, “Beiträge zur Theorie des Mikroskops und der Mikroskopischen Wahrnehmung,” Archiv für Mikroskopische Anatomie, **IX**, 413-68 (1873).

2. Lord Rayleigh, “On the theory of optical images with special reference to the optical microscope,” Phil. Mag., **5**(42), 167-195, (1896).

3. E. H. Synge, "Method for extending microscopic resolution into the ultra-microscopic region," Philosophical magazine, **6**, 356, (1928).

4. J. A. O’Keefe, "Resolving Power of Visible Light," J. Opt. Soc. Am. **46**, 359 (1956).

5. E. A. Ash and G. Nicholls “Super-resolution Aperture Scanning Microscope,” Nature **237**, 510-512 (1972).

6. D. W. Pohl, W. Denk, and M. Lanz, “Optical stethoscopy: image recording with resolution λ/20,” Applied physics letters **44**, 651 (1984).

7. A. Lewis, M. Isaacson, A. Harootunian, et al., “Development of a 500Å spatial resolution light microscope I. light is efficiently transmitted through λ/16 diameter apertures,” Ultramicroscopy **13**, 227 (1984).

8. E. Betzig, J. K. Trautman, T. D. Harris, et al., "Breaking the diffraction barrier: optical microscopy of a nanometric scale," Science **251**, 1468-1470 (1991).

9. H. Heinzelmann and D. W. Pohl "Scanning near-field optical microscopy," Appl. Phys. A **59**, 89-101 (1994).

10. Bert Hecht et al., "Scanning near-field optical microscopy with aperture probes: Fundamentals and applications," J. Of Chem. Phys. **112,** (2000).

11. Julia W.P. Hsu, "Near-field scanning optical microscopy studies of electronic and photonic materials and devices," Materials Science and Engineering **33**, 1-50 (2001).

12. L. Novotny and S. J. Stranick, “Near-field optical microscopy and spectroscopy with pointed probes,” Ann. Rev. Phys. Chem., **57**, 303-331 (2006).

13. P. N. Prasad, “Nanophotonics”, Wiley Interscience (2004).

14. L. Novotny and B. Hecht, “Principles of Nano-Optics,” Cambridge University Press, Cambridge, (2006).

15. G. A. Valaskovic, M. Holton, and G. H. Morrison, “Parameter control, characterization, and optimization in the fabrication of optical fiber near-field probes,” Appl. Opt. **34**, 1215–1228 (1995).

16. D. R. Turner, "United States patent 4,469,554," in AT&T Bell laboratories. Murray Hill, NJ, USA (1983).

17. M. Abraham, W. Ehrfeld, M. Lacher, et al., "Micromachined aperture probe tip for multifunctional scanning probe microscopy," Ultramicroscopy **71**, 93-98 (1998).

18. Liang Wang and Xianfan Xu, "High transmission nanoscale bowtie-shaped aperture probe for near-field optical imaging," Appl. Phys. Lett. **90**, 261105 (2007).

19. Tim H. Taminiau et al, "λ/4 Resonance of an Optical Monopole Antenna Probed by Single Molecule Fluorescence," Nano Letters **7**, 28-33 (2007).

20. F. Zenhausern, M. P. O'Boyle, and H. K. Wickramasinghe, "Apertureless near-field optical microscope," Appl. Phys. Lett. 65, 1623 (1994).

21. H. A. Bethe, "Theory of diffraction by small holes," Phys. Rev. **66**, 163-182 (1944).

22. Bertrand Dutoit, Dieter Zeisel, Volker Deckert, and Renato Zenobi "Laser-Induced Ablation through Nanometer-Sized Tip Apertures: Mechanistic Aspects," The Journal of Physical Chemistry B, 101 (35), 6955-6959 (1997).

23. http://www.nanonics.co.il/multiview-2000.html

24. http://www.nanonics.co.il/optical-fiber-nsom-probes.html

25. http://www.corning.com/opticalfiber/products/SMF-28_ULL_fiber.aspx

26. A. Nesci, and Y. Fainman, "Complex amplitude of an ultrashort pulse with femtosecond resolution in a waveguide using a coherent NSOM at 1550 nm," in Wave Optics and Photonic Devices for Optical Information Processing II, P. Ambs and F. R. Beyette, Jr., eds., Proc. SPIE **5181**, 62-69 (2003).

27. A. T. Forrester, R. A. Gudmundsen, and P. O. Johnson "Photoelectric Mixing of Incoherent Light," Phys. Rev. **99**, 1691 - 1700 (1955).

28. T. Nussmeier, F. Goodwin, and J. Zavin, "A 10.6-um terrestrial communication link," IEEE Journal of Quantum Electronics **10**, pp. 230-235, (1974).

29. R. Dändliker, “Heterodyne holographic interferometry”, Progress in optics **17**, p. 1-84, Amsterdam, North-Holland Publishing Co., (1980).

30. P. Tortora, M. Abashin, I. Marki, W. Nakagawa, L. Vaccaro, M. Salt, H. P. Herzig, U. Levy, and Y. Fainman, "Observation of amplitude and phase in ridge and photonic crystal waveguides operating at 1.55um by use of heterodyne scanning near-field optical microscopy," Opt. Lett. **30**, 2885-2887 (2005).

31. A. Roberts, “Probe-sample interaction in near-field microscopy: analysis of the interaction between a metal diffraction grating and a plane conductor,” Optics Communications, **98**, pp. 225-230 (1993).

32. J. A. Cline and M. Isaacson, "Probe-sample interactions in reflection near-field scanning optical microscopy," Appl. Opt. **34**, pp. 4869-4876 (1995).

33. M. Hammer and R. Stoffer, "PSTM/NSOM Modeling by 2-D Quadridirectional Eigenmode Expansion," J. Lightwave Technol. **23**, p. 1956 (2005).

34. E. Yablonovitch, "Inhibited Spontaneous Emission in Solid-State Physics and Electronics," Phys. Rev. Lett. **58**, 2059-2062 (1987).

35. S. John, "Strong Localization of Photons in certain Disordered Dielectric Superlattices," Phys. Rev. Lett. **58**, 2486-2489 (1987).

36. John D. Joannopoulos, Steven G. Johnson, Joshua N. Winn, and Robert D. Meade “Photonic Crystals: Molding the Flow of Light,” 2nd ed., Princeton University Press (2008).

37. J. W. S. Rayleigh, "On the remarkable phenomenon of crystalline reflexion described by Prof. Stokes." Phil. Mag. **26**, 256-265 (1888).

38. V. P. Bykov, "Spontaneous emission in a periodic structure." Sov. Phys. JETP **35**, 269-273 (1972).

39. R.D. Maede et al.,"Accurate Theoretical Analysis of Photonic Band-Gap Materials", Phys. Rev. B **48**, 8434-8437 (1993).

40. M. Abashin, P. Tortora, I. Märki, U. Levy, W. Nakagawa, L. Vaccaro, H. Herzig, and Y. Fainman, "Near-field characterization of propagating optical modes in photonic crystal waveguides," Opt. Express **14**, 1643-1657 (2006).

41. S. G. Johnson and J. D. Joannopoulos, “Block-iterative frequency-domain methods for Maxwell's equations in a planewave basis,” Optics Express **8**, 173–190 (2001).

42. Kosaka H., Kawashima T., Tomita A., Notomi M., Tamamura T., Sato T. and Kawakami S., "Superprism phenomena in photonic crystals," Phys. Rev. B **58**, R10096–99 (1998).

43. Chigrin D. N., Enoch S., Torres S. C. M. and Tayeb G. "Self-guiding in two-

dimensional photonic crystals" Opt. Express **11** 1203–11 (2003).

44. Dennis W. Prather, Shouyuan Shi, Janusz Murakowski, Garrett J Schneider, Ahmed Sharkawy, Caihua Chen, BingLin Miao and Richard Martin, "Self-collimation in photonic crystal structures: a new paradigm for applications and device development," J. Phys. D: Appl. Phys. **40**, 2635–2651 (2007).

45. M. Loncar, J. Vuckovic and A. Scherer, “Methods for controlling positions of guided modes of photonic-crystal waveguides”, JOSA B, **18** (9), pp. 1362-1368 (2001).

46. Dennis W. Prather, Caihua Chen, Shouyuan Shi, Binglin Miao, David M. Pustai, Sriram Venkataraman, Ahmed S. Sharkawy, Garrett J. Schneider, and Janusz A. Murakowski, "Ultralow-loss photonic crystal waveguides based on the self-collimation effect," Proc. SPIE **5360**, 175 (2004).

47. Dennis W Prather, Shouyuan Shi, Janusz Murakowski, Garrett J. Schneider, Ahmed Sharkawy, Caihua Chen, BingLin Miao and Richard Martin, "Self-collimation in photonic crystal structures: a new paradigm for applications and device development," Journal of Physics D **40**, 2635 (2007).

48. D. W. Prather, A. S. Sharkawy, C. Chen, B. Miao, T. R. Hodson, and S. Shi, "Self-collimation photonic-crystal-based modulator and switching elements in silicon," Proc. SPIE **6640**, 664002 (2007).

49. Jonghwa Shin and Shanhui Fan, "Conditions for self-collimation in three-dimensional photonic crystals," OPt. Lett. **30**, 2397 (2007).

50. Seunghyun Kim, Gregory P. Nordin, Jingbo Cai, and Jianhua Jiang, "Ultracompact high-efficiency polarizing beam splitter with a hybrid photonic crystal and conventional waveguide structure," Opt. Lett. **28**, 2384-2386 (2003).

51. E. Schonbrun, Q. Wu, W. Park, T. Yamashita and C. J. Summers, "Polarization beam splitter based on a photonic crystal heterostructure," Opt. Lett. **31**, 3104 (2006).

52. Rei-Shin Chen and Hong-Bin Wei, "Polarization beam splitter for two-dimensional photonic crystal self-collimation devices," Proc. SPIE **6695**, 669511 (2007)

53. V. Zabelin, L. A. Dunbar, N. Le Thomas, R. Houdré, M. V. Kotlyar, L. O’Faolain, and T. F. Krauss "Self-collimating photonic crystal polarization beam splitter," Opt. Lett. **32**, 530 (2007).

54. F. Xu, R. Tyan, P. C. Sun, C. Cheng, A. Scherer, and Y. Fainman, ‘‘Fabrication, modeling, and characterization of form-birefringent nanostructures,’’ Opt. Lett. **20**, 2457–2459 (1995).

55. R. Tyan, A. Salvekar, Cheng, A. Scherer, F. Xu, P. C. Sun, and Y. Fainman, ‘‘Design, fabrication, and characterization of form-birefringent multilayer polarizing beam splitter,’’ J. Opt. Soc. Am. A **14**, 1627–1636 (1997).

56. W. Nakagawa, R. Tyan, and Y. Fainman, ‘‘Analysis of enhanced second-harmonic generation in periodic nanostructures using modified rigorous coupled-wave analysis in the undepleted-pump approximation,’’ J. Opt. Soc. Am. A **19**, 1919–1928 (2002)

57. U. Levy, C. H. Tsai, L. Pang, and Y. Fainman, ‘‘Engineering space-variant inhomogeneous media for polarization control,’’ Opt. Lett. **29**, 1718–1720 (2004).

58. U. Levy, M. Nezhad, H.-C. Kim, C.-H. Tsai, L. Pang, and Y. Fainman, "Implementation of a graded-index medium by use of subwavelength structures with graded fill factor," J. Opt. Soc. Am. A **22**, 724-733 (2005).

59. J. N. Mait, A. Scherer, O. Dial, D. W. Prather, and X. Gao, ‘‘Diffractive lens fabricated with binary features less than 60 nm,’’ Opt. Lett. **25**, 381–383 (2000).

60. S. M. Rytov, "Electromagnetic properties of a finely stratified medium," Sov. Phys. JETP **2**, 466-475 (1956).

61. I. Richter, P.-C. Sun, F. Xu, and Y. Fainman, "Design considerations of form birefringent microstructures," Appl. Opt. **34**, 2421-2429 (1995).

62. P. Lalanne and D. L. Lalanne, ‘‘Depth dependence of the effective properties of subwavelength gratings,’’ J. Opt. Soc. Am. A **14**, 450–458 (1997).

63. Bruce Peterson, "Data Coding and Error Checking Techniques," Accolade Engineering Solutions, http://www.accoladeeng.com/codes.pdf.

64. Harry J. R. Dutton, "Understanding Optical Communications," International Technical Support Organization, http://www.redbooks.ibm.com/pubs/pdfs/redbooks/sg245230.pdf (1998).

65. R. Rokitski, K. A. Tetz, and Y. Fainman, "Propagation of Femtosecond Surface Plasmon Polariton Pulses on the Surface of a Nanostructured Metallic Film: Space-Time Complex Amplitude Characterization," PRL 95, 177401 (2005).

66. Yu. A. Vlasov, S. Petit, G. Klein, B. Hönerlage, and Ch. Hirlimann, "Femtosecond measurements of the time of flight of photons in a three-dimensional photonic crystal," Phys. Rev. E **60**, 1030 - 1035 (1999).

67. J.-C. Diels, W. Rudolph, “Ultrashort Laser Pulse Phenomena: Fundamentals, Techniques, and Applications on a Femtosecond Time Scale,” Academic Press, San Diego (1996).

68. E. Dulkeith, F. Xia, L. Schares, W. M. J. Green, and Y. A. Vlasov, “Group index and group velocity dispersion in silicon-on-insulator photonic wires,” Opt. Express **14**, 3853–3863 (2006).

69. Y. A. Vlasov, M. O'Boyle, H. F. Hamann & S. J. McNab, "Active control of slow light on a chip with photonic crystal waveguides," Nature **438**, 65-69 (2005).

70. M. L. M. Balistreri, H. Gersen, J. P. Korterik, L. Kuipers, and N. F. van Hulst, "Tracking Femtosecond Laser Pulses in Space and Time," Science **294**(5544), 1080 - 1082 (2001).

71. A. Nesci, R. Dändliker, and H. P. Herzig, "Quantitative amplitude and phase measurement by use of a heterodyne scanning near-field optical microscope," Opt. Lett. **26**, 208-210 (2001).

72. H. Gersen, T. J. Karle, R. J. P. Engelen, W. Bogaerts, J. P. Korterik, N. F. van Hulst, T. F. Krauss, and L. Kuipers, "Real-Space Observation of Ultraslow Light in Photonic Crystal Waveguides," Phys. Rev. Lett. **94**, 073903 (2005).

73. Sandtke, M.; Engelen, R. J. P.; Schoenmaker, H.; Attema, I.; Dekker, H.; Cerjak, I.; Korterik, J. P.; Segerink, F. B.; Kuipers, L. "Novel instrument for surface plasmon polariton tracking in space and time," Review of Scientific Instruments **79**(1), 013704-013704-10 (2008).

74. H. J. W. M. Hoekstra, D. J. W. Klunder, and A. Driessen, "Theory for the measurements of dispersion characteristics in waveguiding structures with a scanning near-field optical microscope," J. Opt. Soc. Am. A **21**, 280-287 (2004).

75. Gersen H., Korterik J.P., van Hulst N.F., Kuipers L., "Tracking ultrashort pulses through dispersive media: Experiment and theory," Phys. Rev. E **68**, 026604 (2003).

76. J. D. Mills, T. Chaipiboonwong, W. S. Brocklesby, M. D. B. Charlton, C. Netti, M. E. Zoorob, and J. J. Baumberg,"Group velocity measurement using spectral interference in near-field scanning optical microscopy," Appl. Phys. Lett. **89**, 051101 (2006).

77. X. Letartre, C. Seassal, C. Grillet, P. Rojo-Romeo, P. Viktorovitch, M. Le Vassor d'Yerville, D. Cassagne, and C. Jouanin, "Group velocity and propagation losses measurement in a single-line photonic-crystal waveguide on InP membranes," Appl. Phys. Lett. **79**, 2312 (2001).

78. V. Shidlovski, “Superluminescent Diodes. Short overview of device operation principles and performance parameters,” SuperlumDiodes Ltd. http://www.superlumdiodes.com/pdf/sld_overview.pdf (2004)

79. A. Sakai, G. Hara, and T. Baba, “Propagation Characteristics of Ultrahigh-Δ

Optical Waveguide on Silicon-on-Insulator Substrate," Jpn. J. Appl. Phys. 40, L383–L385 (2001).

80. C. Turner, C. Manolatou, B. S. Schmidt, M. Lipson, M. A. Foster, J. E. Sharping, and A. L. Gaeta, "Tailored anomalous group-velocity dispersion in silicon channel waveguides," Opt. Express, 14, 4357–4362 (2006).

81. J. Jágerská, N. Le Thomas, R. Houdré, J. Bolten, C. Moormann, T. Wahlbrink, J. Čtyroký, M. Waldow, and M. Först, "Dispersion properties of silicon nanophotonic waveguides investigated with Fourier optics," Opt. Lett., 32, 2723–2725 (2007).